People's Democratic Republic of Algeria Ministry of Higher Education and Scientific Research Ferhat ABBAS University - Setif 1 Faculty of Sciences Department of Physics



Presented to obtain the degree of **DOCTORATE**

Domain: Matter science

Option: Radiation and matter

By: MELLAK Ghada

Theme

Monte Carlo Simulation on Gamma Spectrometry and Application to Radioactivity Measurement in Honey Samples

Defended on 07/07/2025 In the presence of the jury:

Mr.	Maouche Djamel	Professor	UFAS Setif-1	President
Mrs.	Boukhenfouf Wassila	MCA	UFAS Setif-1	Supervisor
Mrs.	Dehimi Fatma Zohra	Principal researcher	Nuclear Research Center of Algiers	Co-Supervisor
Mr.	Bentridi Salah Eddine	MCA	Khemis Miliana University	Examinator
Mrs.	Amrani Naima	Professor	UFAS Setif-1	Examinator
Mr.	Ounoughi Nabil	Professor	JIJEL University	Examinator
Mr.	Messai Adnane	Expert researcher	Nuclear Research Center of Birine	Guest
Mr.	Boucenna Ahmed	Professor	UFAS Setif-1	Guest

I would like to dedicate this thesis to

my beloved parents,
who taught me that small steps,
taken with purpose and love,
can cross impossible distances.
Your unwavering faith in me
turned every challenge into a journey,
and every dream into this achievement

Acknowledgement

First of all, I would like to express my deepest gratitude to God Almighty, whose blessings, guidance, and strength have sustained me throughout this journey. Without His will, none of this would have been possible.

I extend my sincere thanks to my supervisor, **Dr. Boukhenfouf Wassila**, Associate Professor at the Faculty of Physics, Ferhat Abbas University – Sétif, for her exceptional guidance, valuable advice, and continuous encouragement throughout the course of this research. Her expertise and support have been essential to the successful completion of my thesis.

I also wish to express my deep appreciation to my co-supervisor, **Dr. Dehimi Fatma Zohra**, Principal Researcher at the Nuclear Research Center of Algiers, for her insightful feedback, constructive suggestions, and generous support throughout this work. This work was carried out at the Nuclear Research Center of Birine (CRNB). I would like to warmly thank **Dr. Messai Adnane**, Expert Researcher and Director of the Nuclear Instrumentation and Technology Division, for his generous support, guidance, and fatherly presence throughout my research. His encouragement and wisdom have been a true source of inspiration. I am also grateful to **Mr. Hebboul Nour Eddine** for his assistance, collaboration, and for providing a welcoming and motivating research environment.

I am grateful to **Ferhat Abbas University** – **Sétif 1** for providing me with the opportunity and resources to pursue this research. I am especially thankful to **the departement of Physics** for its academic and administrative support during my doctoral studies.

I would like to express my sincere gratitude to Professor **Djamel Maouch**, from the departement of Physics at UFAS, for doing me the honor of chairing the jury of this thesis. I warmly thank him for his availability and for kindly accepting this role.

My sincere thanks also go to the esteemed jury members:

Dr. Bentridi Salah Eddine, Associate Professor of Physics, Khemis-Miliana University

Prof. Ounoughi Nabil, Professor of Physics, Jijel University

Prof. Amrani Naima, Professor of Physics, UFAS

Thank you for taking the time to evaluate my work and for your valuable remarks and recommendations, which greatly enriched the quality of this research.

. I would also like to extend my heartfelt thanks to **Prof. Fabio Mantovani** for kindly accepting my internship at the Laboratory of Nuclear Technologies Applied to the Environment, University of Ferrara, Italy. I am sincerely grateful for his warm welcome, support, and for giving me the opportunity to benefit from such a valuable experience. My deep appreciation also goes to the entire team at the laboratory for their assistance, collaboration, and kindness throughout my stay.

I also sincerely thank **Prof. Haikel Jelassi** for generously accepting me into his laboratory at the Centre National de Sciences et Technologies Nucléaires (CNSTN), Sidi Thabet, Ariana. I am truly grateful for the opportunity to be part of his research group and for the support and guidance provided during my internship. My appreciation also extends to all the members of the laboratory for their collaboration, availability, and for creating a welcoming and productive research environment.

To my colleagues and friends, thank you for your encouragement, help, and for making this academic journey a memorable one.

Finally, I owe special thanks to my family. To my beloved parents, for their endless love, prayers, and sacrifices. Your unwavering belief in me has been my greatest motivation. To my siblings and friends who are like siblings, thank you for your constant support, patience, and understanding during the most challenging times.

This achievement is as much yours as it is mine.

Abstract

By integrating computational modeling (MCNP5, ANGLE, MEFFTRAN) and experimental techniques (gamma spectrometry, AAS, CHARM II), this thesis develops and applies advanced methodologies for analyzing radioactivity and contaminants in honey, a dense and complex matrix with significant nutritional value. The study specifically addresses critical challenges in gamma spectrometry, including photon attenuation, self-absorption, and true coincidence summing (TCS) effects. The optimized Monte Carlo simulations demonstrated excellent agreement with the experimental data (deviations <5% for low-energy gamma rays). The validated model was then applied to quantify naturally occurring radionuclides (226 Ra, 232 Th, and 40 K) in honey samples from various geographical origins. Additional analyses using AAS and CHARM II were employed to evaluate trace levels of heavy metals (K, Zn, Cu, Al, As) and antibiotic residues (tetracyclines and chloramphenicol), revealing contamination trends linked to industrial zones and environmental or apicultural practices. This interdisciplinary approach offers a robust and transferable framework for contaminant analysis in dense matrices, with important implications for food safety regulations, environmental monitoring, and public health protection.

Keywords: Monte Carlo simulations, MCNP5 Code, HPGe Detector Efficiency, Computational Tools(MEFFTRAN, ANGLE), Environmental contamination, Honey.

Résumé

En combinant la modélisation numérique (MCNP5, ANGLE, MEFFTRAN) avec des techniques expérimentales (spectrométrie gamma, (SAA), CHARM II), cette thèse développe et applique des méthodologies avancées pour l'analyse de la radioactivité et des contaminants dans le miel — une matrice dense et complexe, dotée d'une grande valeur nutritionnelle. L'étude traite des principaux défis liés à la spectrométrie gamma, notamment l'atténuation des photons, l'auto-absorption et les effets de coïncidence réelle (TCS). Les simulations Monte Carlo optimisées ont montré une excellente concordance avec les données expérimentales (écarts <5% pour les rayonnements gamma de basse énergie). Le modèle validé a ensuite été appliqué pour quantifier les radionucléides naturels (²²⁶Ra, ²³²Th et ⁴⁰K) dans des échantillons de miel d'origines géographiques variées. Des analyses complémentaires par SAA et CHARM II ont permis de détecter des traces de métaux lourds (K, Zn, Cu, Al, As) et de résidus d'antibiotiques (tétracyclines et chloramphénicol), révélant des tendances de contamination associées aux zones industrielles et aux pratiques apicoles ou environnementales. Cette approche interdisciplinaire fournit un cadre robuste pour l'analyse des contaminants dans les matrices denses, avec des implications importantes pour la sécurité alimentaire, la surveillance environnementale et la santé publique.

Mots Clée: Simulation Monte Carlo, Code MCNP5, Efficacité du détecteur HPGe, Outils de calcul (MEFFTRAN, ANGLE), Contamination Environnementale, Miel.

بالجمع بين النمذجة العددية (شرصه، اشز، شزسسةضا) والتقنيات التجريبية (التحليل الطيفي الأشعة غاما، الامتصاص الذري الانتقائي (ضاا)، وتقنية رساضش يي)، تطوّر هذه الأطروحة وتطبق منهجيات متقدمة لتحليل النشاط الإشعاعي والملوثات في العسل وهو مادة كثيفة ومعقدة ذات قيمة غذائية عالية. تتناول الدراسة التحديات الرئيسية المرتبطة بالتحليل الطيفي الأشعة غاما، بما في ذلك التوهين الفوتوني، واالمتصاص الذاتي، وتأثيرات التوافق الحقيقي (قرض). وقد أظهرت المحاكاة المحسنة باستخدام مونتي كارلو توافقاً ممتازً مع البيانات التجريبية (فروق أقل من ٥٪ الأشعة غاما منخفضة الطاقة).

تم بعد ذلك تطبيق النموذج المحسن لقياس تركيزات النويدات المشعة الطبيعية (26 ض، 23 في عينات من العسل ذات أصول جغرافية متنوعة. كما سمحت التحليلات الإضافية باستخدام ضاا ورساضش يي بالكشف عن آثار معادن ثقيلة (ش، ظن، ر، ال، اس) وبقايا مضادات حيوية (التتراسيكلينات والكلورامفينيكول)، مما أظهر أنماط تلوث مرتبطة بالمناطق الصناعية والممارسات البيئية أو النحلية. توفر هذه المقاربة متعددة التخصصات إطاراً متيناً لتحليل الملوثات في المواد الكثيفة، مع آثار هامة على سلامة الأغذية، ورصد البيئة، والصحة العامة.

الكلمات المفتاحية: محاكاة مونت كارلو، كود شرصه، كفاءة كاشف سص، أدوات حسابية (شرنسسة ضا، اشرز)، مطيافية غاما، التلوث البيئي، العسل،

Contents

Li	st of	Figure	es		i
Li	st of	Tables	S		iii
G	enera	al Intro	oduction	1	1
1	The	eoretic	al Backg	ground	4
	1.1	Introd	uction .		4
	1.2	Conta	minants,	their Sources, and detection	5
		1.2.1	Radioac	etivity in the Environment	5
			1.2.1.1	Natural Sources of Radioactivity	5
			1.2.1.2	Artificial Sources of Radioactivity	6
		1.2.2	Detection	on of Radioactivity: Principles and Interactions	6
			1.2.2.1	Interactions of Gamma Rays	7
			1.2.2.2	Radiation Detectors	7
			1.2.2.3	Semiconductor Detectors	8
			1.2.2.4	Spectrometer Performance Characterization	11
			1.2.2.5	Detection setup	12
		1.2.3	Transiti	on from Experimental Detection to Simulation	13
			1.2.3.1	Monte Carlo Simulation	13
			1.2.3.2	MCNP 5 Code	14
			1.2.3.3	MCNP5 code structure	14
			1.2.3.4	Tools Supporting Efficiency Calculation: ANGLE and MEFF	_ק
				TRAN software	18
		1.2.4	Heavy N	Metals	19
		1.2.5	Heavy n	netals detection and measurement	20
			1.2.5.1	Atomic Absorption Spectroscopy (AAS)	21
			1.2.5.2	Principle of Atomic Absorption Spectroscopy (AAS) $$	21
			1.2.5.3	Instrumentation and Components of AAS	21

			1.2.5.4 Working Process of AAS	22
		1.2.6	Antimicrobial Residues	23
		1.2.7	Antimic robial residues detection and measurement	23
			1.2.7.1 What is the CHARM Technique?	24
			1.2.7.2 Principle of CHARM	24
	1.3	Contar	mination Pathways and Mechanisms	25
	1.4	Bioacc	cumulation and Biomagnification	26
2	Moi	nte Ca	rlo Simulation and Detector Efficiency Modeling	27
	2.1	Introd	uction	27
	2.2	Gamm	na Spectrometry Experimental Setup	28
		2.2.1	Detector features	28
	2.3	Calibra	ation of the Measurement Chain	29
		2.3.1	Energy Calibration	29
		2.3.2	Efficiency calibration for Point Source	30
	2.4	Simula	ations using the Monte Carlo MCNP5 Code	32
		2.4.1	Modeling the detector geometry	32
		2.4.2	Initial Model Based on Manufacturer Specifications	34
		2.4.3	Germanium Crystal Dead Layer Adjustment	35
		2.4.4	Influence of Cross-Section Libraries on Efficiency Calculations $$	38
		2.4.5	Marinelli Beaker Geometry	38
		2.4.6	Modeling of Detector Efficiency for a Marinelli Source	39
		2.4.7	True Coincidence Summing Effects	42
		2.4.8	Methodology for True Coincidence Summing Correction	44
		2.4.9	Application of the Validated Model to Honey Samples	46
		2.4.10	Determination of Self-Absorption Correction Factors using the De-	
			veloped Model	47
		2.4.11	Impact of Cross-Section Library Selection on Simulated Efficiency $$.	48
	2.5	ANGL	E Calculations	49
	2.6	Simula	ation Results and Discussion	50
		2.6.1	Validation of the optimized detector model	50
		2.6.2	Experimental vs. MCNP5 Simulated Efficiency	51
			2.6.2.1 Experimental Vs Simulation calculations	51
3	Exp		ntal Methodology	54
	3.1	Introd	uction	54
	3.2	Sample	e Collection and preparation	54

		3.2.1	Sampling Strategy	54
	3.3	Exper	imental setup	57
		3.3.1	Radioactivity measurements	57
		3.3.2	Gamma Spectrometry Analysis	57
	3.4	Heavy	Metal Analysis	61
		3.4.1	Instrumentation	61
		3.4.2	Sample Preparation	62
		3.4.3	Calibration	62
	3.5	Antibi	iotics residues	63
		3.5.1	Charm II test	63
		3.5.2	Tetracycline Test for Honey	64
		3.5.3	Sample Preparation	65
		3.5.4	Determination of the Control Point (CP)	65
		3.5.5	Interpretation of Results	65
4	Res	ults A	nd Discussions	67
	4.1	Introd	luction	67
	4.2	Exper	imental Analysis of Radioactive Contamination	67
		4.2.1	Activity Concentrations	67
		4.2.2	Spatial Distribution	69
		4.2.3	Radiological Risk Assessment	70
		4.2.4	Multivariate Statistical Analysis	73
	4.3	Exper	imental Analysis of Heavy Metals Contamination	77
		4.3.1	Heavy Metals concentrations	77
		4.3.2	Spatial Distribution	78
		4.3.3	Health Risk Assessments	81
		4.3.4	Multivariate statistical analysis	86
	4.4	Exper	imental Analysis of Antibiotics Residues Contamination	90
		4.4.1	Antibiotics residues concentrations	90
G	lener	al Con	nclusion	92
Bi	ibliog	graphy		95
٨	Т;+1	o of th	ne Appendix	${f A}$
_1	T 101	C OI III	ю другийх	A

List of Figures

1.1	Ionizing radiation interactions	7
1.2	Notion of bandgap (Eg) in an insulator, semiconductor, and conductor	9
1.3	Realization of a P-N junction	10
1.4	polarized P-N junction	10
1.5	Radiation Detector Types and Energy Suitability	11
1.6	Schematic of the electronics used for signal analysis	13
1.7	MCNP code structure	14
1.8	Anthropogenic sources of heavy metal pollution	19
1.9	Atomic Absorption Spectroscopy (AAS) Mechanism Overview	22
1.10	Schema of Honey Contamination: From Source to Exposure	26
2.1	Experimental device of gamma spectrometry used	28
2.2	A radio X for the detector used \dots	29
2.3	Energy calibration curve	30
2.4	Experimental spectrum of ¹⁵² Eu point source	31
2.5	efficiency calibration curve	32
2.6	the dimensions of the detector as supplied by the manufacturer	33
2.7	Comparison of Experimental Full-Energy Peak Efficiency (FEPE) with the	
	simulated by the Manufacturer's dimensions	34
2.8	the detector modeled by the MCNP 5 code	37
2.9	FEP efficiency of detector at different energies for the final model	37
2.10	Marinelli beaker source geometry	39
2.11	the simulated HPGe detector by MCNP5 code with the Marinelli beaker	
	placed in the lead shielding	41
2.12	Comparison of the Experimental and Simulated Spectrum of the $^{152}\mathrm{Eu}$	
	Source in Marinelli Beaker Geometry Using MCNP5	41
2.13	Effect of solid angle on the coincidence effects of sum peaks	43
2.14	decay scheme of Eu-152	44

2.15	Simulated efficiency curves for different honey densities				
2.16	Variation of the self - absorption correction factor on the sample density				
	(g/cm3)	48			
2.17	Efficiency calibration curves for the two libraries ${\rm ENDF/B.VI}$ and JENDL-5	49			
2.18	$^{152}\mathrm{Eu}$ Spectrum: Experimental vs. MCNP Simulation (Optimized Model) .	51			
2.19	Comparison between experimental and MCNP-5 efficiencies	52			
2.20	$\label{thm:experimental} Efficiency \ calibration \ curves \ for \ both \ experimental \ and \ simulation \ calculation.$	53			
3.1	Honey samples collection	55			
3.2	Map of sampling locations	56			
3.3	Spectrum of gamma radiation emitted by honey sample H008	60			
3.4	Spectrum of gamma radiations emitted by honey sample H001	60			
3.5	digestion process	62			
3.6	Calibration Curve for Quantification of Heavy Metals Using Atomic Ab-				
	sorption Spectroscopy (AAS)	63			
3.7	Charm II 7600 system equipment	64			
3.8	CHARM II test principle	64			
3.9	Example of interpretation of Charm II test results	66			
4.1	Distribution of Activity concentration in honey samples: Spatial distribu-				
	tions of 232 Th, 226 Ra and 40 K	69			
4.2	Pearson's correlation matrix for studied honey sapmles	74			
4.3	Principal component plot	76			
4.4	Clustering dendrogram of the honey samples' radiological parameters and				
	radionuclides	77			
4.5	K distribution	78			
4.6	Zn distrbution	79			
4.7	Cu distrbution	79			
4.8	Al distribution	80			
4.9	As distribution	80			
4.10	Hazard index	86			
4.11	Pearson's correlation matrix for studied heavy metals of honey sapmles	87			
4.12	PCA analysis loading 2-D plot (PC 1 vs PC 2) for heavy metals in honey .	88			
4.13	hierarchical dendrogram	89			

List of Tables

1.1	Properties of Common Naturally Occurring Radioactive Radionuclides	5
1.2	MCNP surface Cards	16
1.3	Summary of MCNP Tally Types, Their Applications, and Examples	17
1.4	Classification of Heavy Metals	20
1.5	Commonly Used Antibiotics in Beekeeping	23
2.1	Gamma Energies, Emission Probabilities, and Corresponding Channel Num-	
	bers	30
2.2	The HPGe parameters provided by the manufacturer and values from the	
	optimized model	36
2.3	True Coincidence Summing (TCS) Correction Factors for Different Gamma	
	Energies	45
3.1	Botanical origins of honey samples from North-eastern regions of Algeria .	56
3.2	Operating parameters for elemental analysis using AAS	61
3.3	Calibration parameters for heavy metal analysis using AAS: concentration	
	ranges and correlation coefficients (R^2)	63
4.1	Comparison of the radioactivity levels in honey samples with those from	
	other regions worldwide	68
4.2	The caculated values of daily intake and radiological health risks parame-	
	ters of 226 Ra, 232 Th and 40 K	72
4.3	Comparison of the radioactivity levels in honey samples with those from	
	other regions worldwide	73
4.4	Principal component analysis of the radionuclides and radiological health	
	risk parameters in honey samples	7 4
4.5	Principal component analysis of the radionuclides and radiological health	
	risk parameters in honey samples	76
4.6	Concentrations (mg/L) of heavy metals in honey	78

$LIST\ OF\ TABLES$

4.7	Reference oral dose (RfD) for metals	82		
4.8	Daily Intake of Metals from honey consumption by a dults and children $$	83		
4.9	Target hazard quotient and harzard index of metals from honey consump-			
	tion by a dults and children	84		
4.10	Principal component analysis of trace metals in honey samples	88		
4.11	Tetracyclines Residue Detection Results and Sample Analysis	90		
4.12	Chloramphenicol Residue Detection Results and Sample Analysis	91		

General Introduction

Due to the rapid urbanization and population growth, food safety has become a critical global concern. With the increasing demand for enhanced food production and widespread distribution, ensuring food safety and maintaining stringent quality control measures have become imperative. In recent years, many studies have focused on environmental pollution and food contamination in various products including fruits, vegetables, milk, meat, and other products [1–3]. Among these, the measurement of radioactivity in environmental and food samples has emerged as a vital area of reaserch due to its implications for public health, environmental safety, and regulatory compliance.

Honey, a natural sweetener consumed world wide, holds a unique position in human history and culture for centuries. Renowned for its nutritional and medicinal properties, including antibacterial and anti-inflammatory qualities [4], honey is produced by honeybees from flower nectar. As a widely consumed food product, its composition and quality are of significant interest to both consumers and researchers [5]. However, honey is also a potential carrier of environmental contaminants, including radionuclides, heavy metals, and antibiotic residues. These contaminants can originate from various sources, such as soil, water, air, and beekeeping practices, making honey a valuable indicator of environmental pollution. Consequently, the accurate quantification of these contaminants in honey is essential for ensuring food safety and assessing environmental impact.

In the field of environmental radioactivity analysis, the High-Purity Germanium (HPGe) detector is a preferred tool due to its high resolution and ability to perform non-destructive, high-performance analyses [6]. This detector allows for the simultaneous measurement of all gamma-emitting radionuclides within an energy range of 20 to 2000 keV in a single analysis. However, the unique physical and chemical properties of honey, such as its high density and complex matrix, pose significant challenges for gamma spectrometry. Honey typically has a density ranging from 1.25 to 1.45 g/cm^3 , which is much higher than water (1.0 g/cm^3) and many other liquids like vegetable oils (0.92 g/cm^3) but less dense than

metals or dense organic compounds. This high density, combined with its heterogeneous composition (e.g., sugars, water, organic acids, and trace minerals), results in a complex matrix that can cause photon attenuation and self-absorption effects [7]. These effects distort the gamma-ray spectra, leading to inaccuracies in activity concentration measurements.

To address these challenges, advanced computational and experimental approaches are required. Monte Carlo simulations, such as those performed using the MCNP (Monte Carlo N-Particle) code, have emerged as powerful tools for modeling detector responses and determining the full-energy peak efficiency (FEPE) in complex geometries. These simulations account for critical factors such as sample density, geometry, and self-absorption, enabling researchers to correct for matrix effects and improve the accuracy of radioactivity measurements [8]. By simulating the interaction of gamma rays with the honey matrix and the detector, Monte Carlo methods provide a reliable way to optimize measurement conditions and validate experimental results. This approach is particularly important for honey, as its variable composition and high density make it difficult to apply standard calibration methods used for denser or more homogeneous samples.

In this study, semi-empirical codes were also employed to enhance the accuracy of efficiency calculations and corrections. The ANGLE software was used to determine the full-energy peak efficiency (FEPE) by modeling the effective solid angle and accounting for geometric and matrix effects [9]. Additionally, the MEFFTRAN software was utilized to correct for true coincidence summing effects, which are critical for accurate gamma spectrometry measurements, especially when working with a Marinelli beaker geometry. Environmental samples of very low radioactivity are often measured in specially designed containers to ensure maximum detection efficiency, called Marinelli beaker geometry. The Marinelli beaker, with its unique shape and large sample volume, required precise efficiency calibration and correction for summing effects to ensure reliable detector performance. These tools, combined with Monte Carlo simulations, provided a comprehensive framework for addressing the challenges posed by low-density and heterogeneous samples, ensuring reliable and reproducible results [10].

In addition to radionuclides, honey can also contain trace amounts of heavy metals and antibiotic residues, which pose additional risks to human health. Heavy metals, such as lead, cadmium, and arsenic, can accumulate in honey through environmental contamination, while antibiotics, such as tetracyclines, may be introduced through beekeeping practices aimed at controlling bacterial diseases. The simultaneous detection and quan-

tification of these contaminants require a multidisciplinary approach, combining gamma spectrometry with techniques like Atomic Absorption Spectroscopy (AAS) for heavy metals and receptor-binding assays (e.g., CHARM II) for antibiotics.

This thesis focuses on the development and application of advanced methodologies for the comprehensive analysis of radioactivity and contaminants in honey. The research is structured around three main objectives: (1) optimizing Monte Carlo simulations using the MCNP code to determine full-energy peak efficiency for gamma spectrometry in honey samples, (2) quantifying radionuclide activity concentrations in honey and assessing their potential health risks, and (3) evaluating the levels of heavy metals and antibiotic residues in honey using AAS and CHARM II techniques, respectively. By integrating computational modeling, experimental measurements, and analytical chemistry, this study aims to provide a holistic understanding of the contamination profile of honey and its implications for food safety and environmental monitoring. The findings of this research are expected to contribute to the development of standardized methods for radioactivity and contaminant analysis in high-density matrices like honey. Furthermore, the results will provide valuable insights into the sources and levels of environmental contaminants, supporting regulatory efforts to ensure the safety and quality of honey and other food products.

This manuscript is organized into four chapters. The first chapter provides a theoretical background, discussing sources of contamination, contamination pathways, and detection methods. It also covers the fundamental principles necessary for understanding radiation interaction mechanisms and offers a general description of simulations using the MCNP5 code. The second chapter focuses on the simulation methodology, detailing the approaches used to optimize the HPGe detector. This includes a comparison between experimental measurements and MCNPX modeling calculations, as well as corrections for coincidence summing effects. The third chapter describes the experimental methodology for analyzing honey samples, encompassing gamma spectrometry, atomic absorption spectroscopy (AAS), and the CHARM II technique. The fourth chapter presents the results and discussion, offering a comprehensive interpretation of the findings. Finally, the general conclusion summarizes the key outcomes, highlights the implications of the research, and outlines future perspectives.

Chapter 1

Theoretical Background

1.1 Introduction

The accurate assessment of contaminants in food products requires a multidisciplinary approach that combines knowledge of environmental sources, detection technologies, and computational modeling. This chapter provides a theoretical foundation for understanding the nature, sources, and pathways of contaminants—particularly heavy metals, antimicrobial residues, and radioactive substances—within biological and environmental matrices such as honey.

Honey is a remarkable natural product, valued not only for its nutritional benefits, such as its rich antioxidant content, and medicinal properties, including its use as a natural antimicrobial agent [11]. But also, for its role as a powerful bioindicator of environmental pollution. This unique ability stems from how honey is produced—bees forage over vast areas, collecting nectar and pollen that may carry traces of pollutants from their surroundings. As a result, honey serves as a natural record of environmental conditions, reflecting the presence of contaminants in its production area [12].

This chapter introduces the principles behind the detection techniques used in this work, including Atomic Absorption Spectroscopy (AAS), the CHARM II technique, and gamma-ray spectrometry using HPGe detectors. Moreover, it explores the physical interactions of radiation with matter, the structure and functioning of detectors, and the challenges posed by high-density matrices. The chapter concludes by introducing computational tools such as MCNP5, ANGLE, and MEFFTRAN, which are essential for modeling detector responses, correcting measurement artifacts, and ensuring accurate quantification of radioactivity in complex samples.

1.2 Contaminants, their Sources, and detection

1.2.1 Radioactivity in the Environment

Radioactivity refers to the spontaneous decay of unstable atomic nuclei, releasing energy in the form of radiation. The presence of radioactive materials in the environment can arise from both natural and human-made sources, contributing to the background radiation to which all living organisms are exposed. Understanding the distribution, sources, and pathways of radioactivity in the environment is crucial for assessing its impact on ecosystems, food safety, and public health [13].

1.2.1.1 Natural Sources of Radioactivity

The sources of natural radioactivity contribute to the Earth's background radiation and play a significant role in environmental radioactivity levels [14].

• A.Primordial Radionuclides Primordial radionuclides are elements with long half-lives that have persisted since the Earth's creation. The most significant among them include:

Isotope	Half Life	Radiation Type	Sources
Thorium-232 (232Th)	14 billion years	Alpha, Gamma	Found in granite, sands, and ores
Radium-226 (226Ra)	1,600 years	Alpha, Gamma	Product of ²³⁸ U. Found in rocks, soil, and ores
Potassium-40 (40K)	1.25 billion years	Beta, Gamma	Found in soil, rocks, and plants

Table 1.1: Properties of Common Naturally Occurring Radioactive Radionuclides

These radionuclides contribute to background radiation and can enter the ecosystem through soil, water, and air.

• Radon: Characteristics, Exposure, and Sources

Radon (²²²Ra, ²²⁰Ra, ²¹⁹Ra) is a naturally occurring radioactive gas produced by the decay of uranium and thorium found in rocks, soil, and certain building materials. Because of its colorless, odorless, and tasteless, radon is not detectable without specialized instruments, making it a silent health hazard in many environments. The most common isotope, ²²²Ra, has a half-life of 3.8 days. It can accumulate:

- in lung tissue, as it decays, it releases radioactive particles that posing significant health risks over time (cancer) [15].
- indoors, particularly in basements, crawl spaces, and other poorly ventilated areas, due to its ability to seep through cracks in foundations and walls.
- into groundwater by dissolving and contaminate water supplies, potentially entering the food chain through irrigation and cooking processes [16].
- B. Cosmogenic Radionuclides Cosmic radiation originates from the sun and other celestial bodies. When cosmic rays penetrate the Earth's atmosphere, they interact with atmospheric molecules, producing secondary radiation that reaches the surface [17]. Some notable radionuclides formed through these interactions include:
 - Carbon-14 (C-14): Produced in the upper atmosphere when cosmic rays collide with nitrogen atoms (N-14), resulting in a radioactive form of carbon. It is widely used in radiocarbon dating to determine the age of organic materials [18].
 - Tritium (H-3): A radioactive isotope of hydrogen created by cosmic ray interactions with atmospheric gases. Tritium is often incorporated into water molecules and has various applications, including scientific research and environmental monitoring.

1.2.1.2 Artificial Sources of Radioactivity

Anthropogenic activities significantly contribute to the presence of artificial radionuclides in the environment. The most notable sources include:

- Nuclear Accidents: Events such as the Chernobyl disaster in 1986 and the Fukushima Daiichi accident in 2011 released substantial amounts of radioactive materials, including ¹³⁷Cs and ¹³³I, into the environment. [19].
- Nuclear Testing: Atmospheric nuclear weapons tests conducted during the mid-20th century introduced radionuclides like ⁹⁰Sr and ¹³⁷Cs into the environment [20].
- Industrial and Medical Waste: Improper disposal of radioactive materials from medical imaging and industrial applications can lead to localized contamination of soil and water [21].

1.2.2 Detection of Radioactivity: Principles and Interactions

The detection of radioactivity is based on the interactions between radiation and matter, which generate measurable signals. Understanding these interactions is critical for selecting the appropriate detection method and interpreting the results [14]. The primary types of interactions include:

1.2.2.1 Interactions of Gamma Rays

Gamma rays, being highly penetrating electromagnetic radiation, interact with matter through three main mechanisms:

- Photoelectric Effect: Occurs when a gamma photon is completely absorbed by an atom, ejecting an inner-shell electron. This interaction is dominant at low energies and contributes to high-resolution measurements in detectors like High-Purity Germanium (HPGe).
- Compton Scattering: A gamma photon transfers part of its energy to an electron, causing it to scatter. This is the predominant interaction for medium-energy gamma rays.
- Pair Production: At higher energies (greater than 1.022 MeV), the gamma photon is converted into an electron-positron pair [22].

The distribution of the 3 elementary effects according to the atomic number of the material and the energy of the incident photon are given in figure below 1.1:

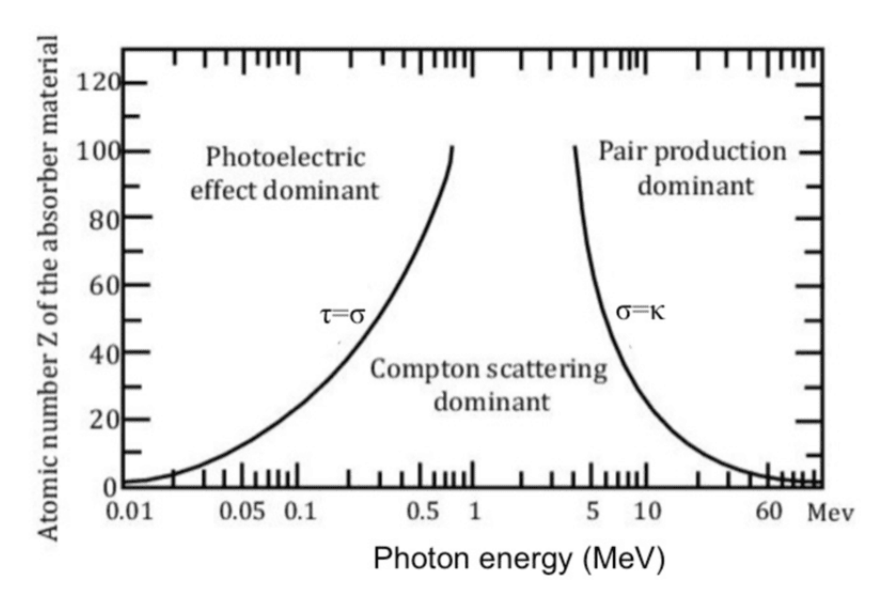


Figure 1.1: Ionizing radiation interactions

1.2.2.2 Radiation Detectors

Radiation detection is based on phenomena of interaction with matter; detectors make it possible to know the nature, number, and energy of particles emitted by radioactive sources. Two groups of detectors can be mainly distinguished according to their operating principles: ionization of matter (Geiger-Muller counter, semiconductors); excitation of electronic orbitals (scintillation detectors).

1.2.2.3 Semiconductor Detectors

A semiconductor is a material that can function as both an insulator and a conductor. A semiconductor detector consists of a single crystal, either elemental or compound, with a band gap typically ranging from 1 to 5 eV. The Group IV elements in Mendeliev table, particularly silicon and germanium, are the most widely used pure semiconductors in radiation detection. These detectors are valued for their excellent energy resolution compared to other types, due to the low energy required to generate charge carriers [23].

Operating principle of semiconductor detectors

When photons interact with the detector material, they undergo several possible interaction mechanisms depending on their energy. These interactions transfer part or all of the photon's energy to the cristal material, generating electron-hole pairs. The number of pairs created (n) depends on the deposited energy of the incident photon E_{abs} and the average energy required to create one pair, as expressed by the relationship [24]: The number of charge carriers generated is given by:

$$n = \frac{E_{\rm abs}}{\varepsilon}$$

For germanium, the average energy required to create an electron-hole pair is $\varepsilon = 2.96$ eV at 77 K.

However, ε represents an average value, with some dispersion due to the stochastic nature of valence electrons moving into the conduction band. The number of electron-hole pairs produced is proportional to the energy deposited by the photon, and its statistical fluctuation follows Poisson statistics as a first approximation, scaling with the square root of n [25].

Poisson statistics assume that each event occurs independently. In reality, the presence of an existing electron-hole pair affects the probability of generating additional pairs. To account for this effect, an experimentally determined correction factor—known as the **Fano factor** (F)—is introduced. The standard deviation associated with the production of charge carriers, σ_p , is therefore given by [26]:

$$\sigma_p = \sqrt{F \cdot E_{\text{abs}} \cdot \varepsilon}$$

Figure 1.2 illustrates the electronic band structure in a semiconductor. The valence band is completely filled with electrons, whereas the conduction band is empty. The energy gap between the two bands is less than 1 eV for germanium (0.67 eV).

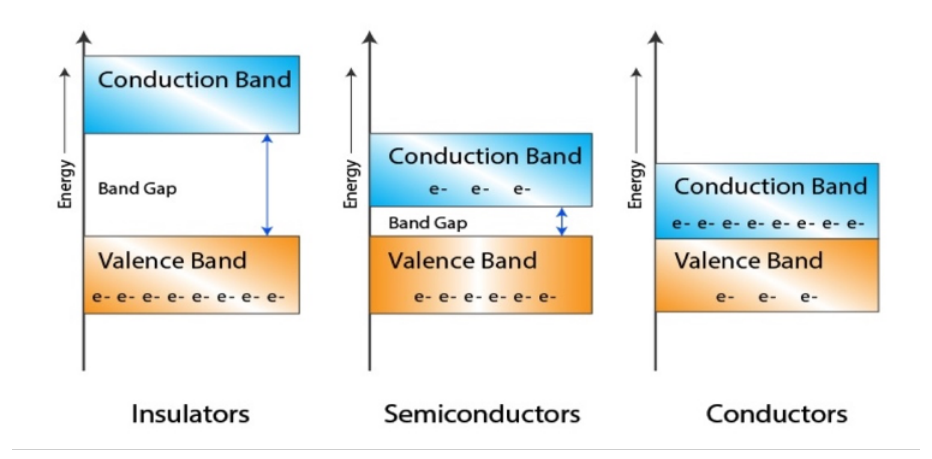


Figure 1.2: Notion of bandgap (Eg) in an insulator, semiconductor, and conductor

However, thermal excitation can provide sufficient energy for an electron in the valence band to move to the conduction band. As a result, a population of electrons exists in the conduction band, contributing to the material's conductivity. At room temperature, this intrinsic conductivity interferes with measurements, necessitating the cooling of germanium (Ge) with liquid nitrogen (77 K) or electric cooler to reduce thermal excitations. Doping is the process of introducing impurities into a semiconductor to create energy levels within the band gap.

- **N-doping** results in an excess of electrons due to donor impurities, such as phosphorus, which contribute free electrons to the conduction band.
- **P-doping** leads to an excess of holes due to acceptor impurities, such as lithium, which capture electrons and create vacant energy states in the valence band.

To create a junction, the N-type and P-type semiconductors must be joined together (see Figure 1.3). Once joined, excess electrons from the N region migrate to the P region (electron-hole recombination), resulting in a region devoid of charge carriers (neither electrons nor holes) at the junction interface. This region is known as the depletion region [27].

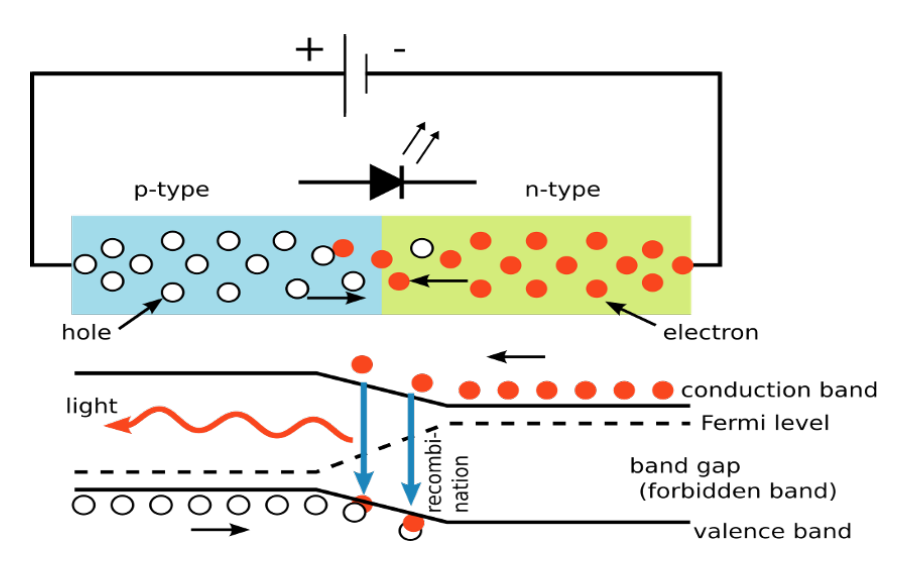


Figure 1.3: Realization of a P-N junction

The width of the depletion region is initially small because the electric field created by the migration of charges counterbalances further migration. To enhance the performance of the junction, it is necessary to widen the depletion region as much as possible [28].

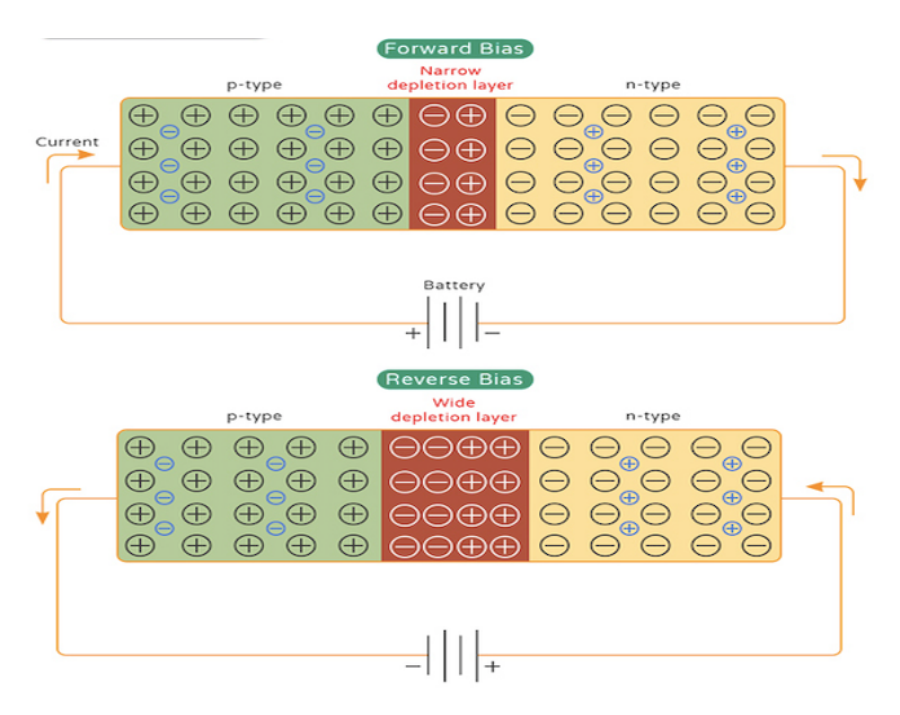


Figure 1.4: polarized P-N junction

To increase the width of the depletion region A reverse polarization is applied, which is an electric field with a strong potential difference is used in the opposite direction, when a gamma photon hits the depleted region, it interacts through processes (the photoelectric effect, Compton effect or pair creation) (see Figure 1.4). This generates electron-hole

pairs, and under the electric field, the charge carriers move towards the electrodes, creating current.

High-Purity Germanium (HPGe) detector

HPGe detector is a radiation detection device that uses an ultra-pure germanium crystal to measure gamma rays and X-rays with exceptional energy resolution. Unlike regular germanium, the crystal in an HPGe detector contains extremely low levels of impurities (less than 1 part in 10¹² atoms)), allowing it to function as an excellent semiconductor radiation sensor [24]. Today, there are many different types of Germanium detector. Each type meets one or more of the user's needs. For example, some will offer optimum efficiency or resolution, while others will only be truly effective in a specific energy range, and so on. However, these different types of detectors can be classified into three broad categories:planar detectors, coaxial detectors, and well detectors. These categories of detectors are distinguished above all by their geometry, which gives them distinct characteristics [29].

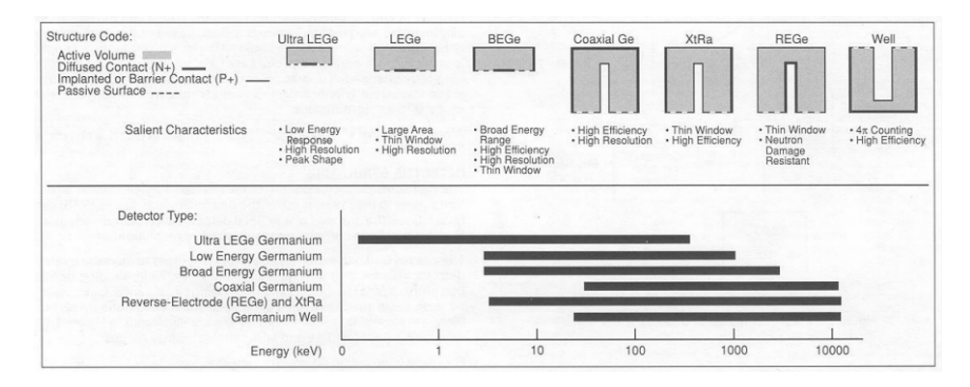


Figure 1.5: Radiation Detector Types and Energy Suitability

1.2.2.4 Spectrometer Performance Characterization

The performance of a gamma spectrometer is primarily determined by two key characteristics of the detector:

- Energy Resolution is a critical parameter that defines the detector's ability to distinguish between two gamma rays of close energy. A higher energy resolution allows for clearer separation of spectral peaks, making it easier to identify and quantify radionuclides in the sample [24]. Energy resolution is typically expressed as the Full Width at Half Maximum (FWHM) of a peak, where a smaller FWHM value corresponds to better resolution. For High-Purity Germanium (HPGe) detectors, typical energy resolutions are in the range of 0.1% to 2% at 1 MeV, depending on the detector's design and operating conditions [30].
- Efficiency The efficiency of a detector is the ratio of the number of gamma photons

detected to the total number of photons emitted by the sample. It is a function of several factors, including the geometry of the detector, the material's atomic number, and the energy of the gamma radiation. Higher efficiency results in a greater number of detected events, which translates to more reliable and accurate measurements of radioactivity. For HPGe detectors, efficiency is typically expressed as a percentage and varies with photon energy, geometry, and the distance between the sample and detector [25].

1.2.2.5 Detection setup

- Cryostat: This is used to cool the HPGe detector to cryogenic temperatures (around 77K) using liquid nitrogen, which improves the detector's performance by reducing electronic noise [26].
- The preamplifier: The preamplifier's role is to serve as an interface between the HPGe detector crystal and the pulse-processing electronics. It takes the charge produced by the detector from gamma radiation and integrates and amplifies it to produce a step-function pulse, where the amplitude is proportional to the total charge [31].
- The amplifier: The amplifier's role is to take the pulse signal from the preamplifier and significantly magnify it. It also filters and shapes the incoming pulse to enhance the signal-to-noise ratio, improving the resolution and shortening the response time to prevent overlap between pulses. This is important because count rates for radionuclides in environmental samples are typically low, and the amplifier needs to perform optimally in this range (less than 100 counts per second) [29].
- The multi-channel analyzer (MCA): Its primary role is to convert the amplified pulse signals from the detector into a digital form that can be analyzed, sorting the pulses into distinct channels based on their amplitude (energy). This enables the MCA to generate an energy spectrum, which is used to identify and quantify radionuclides based on their characteristic gamma emission peaks [31].
- Gamma Spectrometer Software: is used to analyze the energy spectrum obtained from the HPGe detector. It helps to identify isotopes based on their energy peaks and calculate activity concentrations.

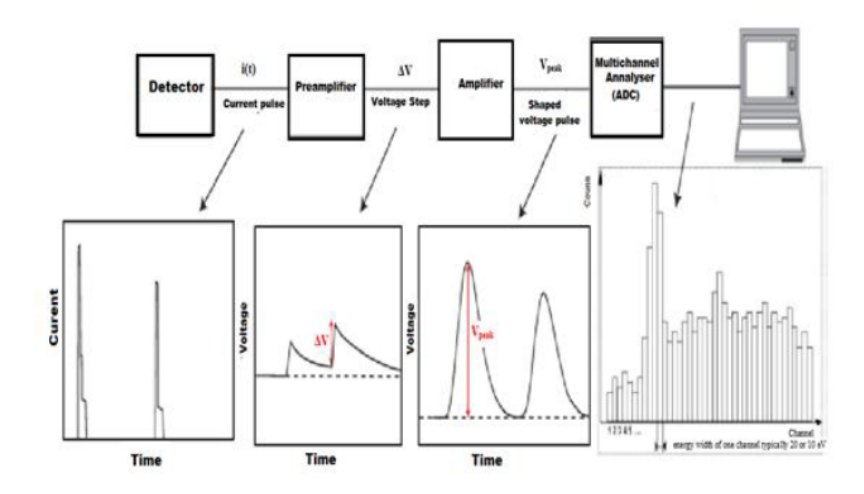


Figure 1.6: Schematic of the electronics used for signal analysis

1.2.3 Transition from Experimental Detection to Simulation

While experimental techniques such as HPGe gamma-ray spectrometry, AAS, and CHARM provide precise measurements of contaminants in honey, they have inherent limitations. The accuracy of radioactivity detection using HPGe detectors depends on factors such as detector geometry, sample composition, and photon interactions, which can introduce uncertainties in efficiency calculations. Similarly, AAS and CHARM techniques require extensive sample preparation and are constrained by detection limits and matrix effects. These challenges highlight the need for computational modeling to complement experimental findings and enhance measurement accuracy.

1.2.3.1 Monte Carlo Simulation

Monte Carlo simulation is a computational technique that uses random sampling and statistical probability to model complex physical and mathematical systems. It is particularly useful for solving problems involving uncertainty, stochastic behavior, or multiple interacting variables, making it a widely applied method in physics, engineering, finance, and medicine. The core idea of Monte Carlo simulation is to generate a large number of random events and analyze their outcomes to approximate solutions to problems that would be difficult to solve analytically [32]. Monte Carlo methods are especially powerful in radiation physics and nuclear science, where they are used to simulate the behavior of particles such as photons, neutrons, and electrons as they interact with different materials. In gamma-ray spectrometry, Monte Carlo simulations play a crucial role in optimizing detector efficiency, radiation shielding, and measurement accuracy.

1.2.3.2 MCNP 5 Code

One of the most widely used Monte Carlo-based codes for radiation transport is MCNP5 (Monte Carlo N-Particle version 5), developed by Los Alamos National Laboratory (LANL). MCNP5 is a general-purpose code designed to simulate the interactions of neutrons, photons, and electrons with matter, making it an essential tool for studying gamma-ray detectors, such as High-Purity Germanium (HPGe) systems [33]. In this study, MCNP5 is used to model the HPGe detector and calculate its Full Energy Peak Efficiency (FEPE), which is critical for accurately measuring radioactivity levels in honey samples. By integrating Monte Carlo simulations with experimental techniques, this research aims to enhance the precision of radioactivity assessments while reducing reliance on standard calibration sources.

1.2.3.3 MCNP5 code structure

An MCNP input file has three major sections: cell cards, surface cards, and data cards. The input file begins with a one-line title card, followed by the cell card section. Each card represents a single line of input, with a maximum of 80 characters [34].

Title Card
blank line terminator {optional}
Cell Cards [Block 1]
blank line delimiter
Surface Cards [Block 2]
blank line delimiter
Data Cards [Block 3]
blank line terminator {optional}

Figure 1.7: MCNP code structure

1. The title card

The title card is the first line in an MCNP input file and can be up to 80 characters in length. It typically provides information about the problem being modeled and is displayed in various locations throughout the MCNP output. The title also acts as a label, helping to differentiate between input files and identify the content of the output files.

2. Cell Cards

The first section after the title card is for the cell cards and has no blank line delimiter at

the front of it. Cells are used to define the shape and material content of physical space. The specific format for a cell card is [35]:

j m d geo params where: j: is the cell number is is an integer from 1 to 99999.

m: is the material number is an integer from 1 to 99999, used to specify the material present in a cell (0 if the cell is a void). The composition of each material is defined in the data card section.

d: is the cell material density

- no entry if the cell is a void.
- positive entry = atom density (atoms/b·cm).
- negative entry = mass density (g/cm^3) .

geom: List of all signed surface numbers and Boolean operators that specify a cell.

Params: Optional specification of cell parameters For example, the importance card (imp:p,e=1) specifies the relative cell importance for photons and electrons.

3. Surface Cards

```
The specific format for a surface card is [35]:

j a list
where:
j: is surface number starting in columns 1-5 (1-99999).
a: surface mnemonic (plane, sphere, cylinder...), as presented in table 1.2
List: numbers that describe the surface in cm (dimensions, radius, etc.,).
```

4. The Data Cards

The data cards section in an MCNP input file is where the key parameters and settings for the simulation are defined.

- Mode Card: The MODE card specifies the types of particles that will be tracked during the simulation. MCNP is capable of simulating multiple particle types, including neutrons (N), photons (P), and electrons (E), and the MODE card determines which of these particles are included in the simulation. For example, MODE P E indicates that both photons and electrons will be tracked [36].
- Material Cards (M):In MCNP, the M card plays a key role in defining the materials used in the simulation. Each material is given a unique label, such as M1 or M2, and is made up of one or more nuclides. These nuclides are identified using the ZAID (Z-AID) format, which merges the atomic number (Z) and the mass number (A) of the element. For instance, 1001 refers to hydrogen-1, and 6012 represents carbon-12. The material's composition is determined by listing each nuclide's ZAID along with its proportion, which can be expressed either by atom or by weight. For example, M1 1001 1.0 describes a ma-

Table 1.2: MCNP surface Cards

Surface Type	Definition	Equation Format	Example
		Plane Surfaces	
PX	Plane ⊥ to x-axis	x = a	1 PX 10 \$ Plane at $x = 10$
PY	Plane ⊥ to y-axis	y = b	2 PY 5 \$ Plane at $y = 5$
PZ	Plane ⊥ to z-axis	z = c	3 PZ -3 \$ Plane at $z = -3$
P	General plane	Ax + By + Cz = D	4 P 1 1 1 -10 $\$x+y+z=10$
		Spherical Surfaces	
SO	Sphere at origin	$x^2 + y^2 + z^2 = R^2$	5 SO 5 \$ Radius = 5
S	Sphere at (x_0, y_0, z_0)	$(x - x_0)^2 + (y - y_0)^2 + (z - z_0)^2 = R^2$	6 S 2 3 4 10
		Cylindrical Surfaces	
CX	Along x-axis	$(y - y_0)^2 + (z - z_0)^2 = R^2$	7 CX 3 2
CY	Along y-axis	$(x - x_0)^2 + (z - z_0)^2 = R^2$	$ \begin{array}{cccccccccccccccccccccccccccccccccccc$
CZ	Along z-axis	$(x - x_0)^2 + (y - y_0)^2 = R^2$	$ \begin{array}{cccccccccccccccccccccccccccccccccccc$
		Conical Surfaces	
KX	Cone along x-axis	$ (y - y_0)^2 + (z - z_0)^2 = (x - x_0)^2 \tan^2 \theta $	10 KX 0 0 0 30
KY	Cone along y-axis		11 KY 2 2 2 45
KZ	Cone along z-axis	$(x - x_0)^2 + (y - y_0)^2 = (z - z_0)^2 \tan^2 \theta$	12 KZ 1 1 1 60

terial consisting entirely of hydrogen-1, while M2 6000 0.5 8016 0.5 defines a material with equal parts carbon-12 and oxygen-16 by atom fraction. These definitions are crucial because they directly influence how particles interact with the simulated geometry, affecting outcomes such as particle scattering, absorption, and energy deposition. Accurate material definitions are therefore essential for ensuring the simulation reflects real-world behavior [37].

• Source Definition (SDEF): The SDEF card defines the particle source. It specifies the position, energy, direction, and type of particles being emitted. For example, SDEF POS=0 0 ERG=1.41 PAR=1 defines a photon source located at the origin with an energy of 1.41 MeV. Additional parameters, such as DIR for direction or EXT for spatial

distribution, can be included to further refine the source definition. The SDEF card is essential for ensuring that the simulation accurately represents the physical conditions of the problem, such as a point source, a beam, or a distributed source [35].

• Tallies: In MCNP, tallies are used to measure specific quantities of interest during a simulation, such as particle flux, energy deposition, or reaction rates. The table 1.3 provides an overview of the most commonly used tally types, their descriptions, and their applications [38].

Table 1.3: Summary of MCNP Tally Types, Their Applications, and Examples

Tally Type	Description	Example	Use Case
F1	Surface current tally (particles crossing a surface).	F1:N 1	Measures neutron current across surface 1.
F2	Surface flux tally (particle flux integrated over a surface).	F2:P 2	Measures photon flux on surface 2.
F4	Track-length estimate of particle flux in a cell.	F4:N 1	Calculates neutron flux in cell 1.
F5	Point detector tally (flux at a specific point in space).	F5:N 0 0 0	Measures neutron flux at the origin $(0,0,0)$.
F6	Energy deposition tally (energy deposited in a cell).	F6:N 1	Calculates energy deposited by neutrons in cell 1.
F7	Fission energy deposition tally (energy from fission reactions in a cell).	F7:N 1	Measures fission energy deposition in cell 1.
F8	Pulse-height tally (energy deposition in a cell, used for detector response).	F8:P 1	Simulates detector response to photons in cell 1.
F9	Radiative heating tally (energy deposited by photons in a cell).	F9:P 1	Measures heating caused by photons in cell 1.
FM	Multiplier card (used to modify tallies, e.g., for reaction rates or dose).	FM4 1 (1 102)	Multiplies F4 tally by the (n,γ) cross-section for reaction rates.
Е	Energy bins (used to divide tally results into energy groups).	E4 0 1 10	Divides F4 tally results into energy bins: 0-1 MeV and 1-10 MeV.
Т	Time bins (used to divide tally results into time intervals).	T4 0 1e-6 1e-3	Divides F4 tally results into time bins: 0-1 μ s and 1 μ s-1 ms.
C	Cosine bins (used for angular distribution of particles).	C4 -101	Divides F4 tally results by cosine of the angle: backward, perpendicular, forward.

• Physics and Control Parameters: The NPS card sets the number of particle histories to simulate, which directly affects the statistical accuracy of the results (e.g.,

NPS 100000 simulates 100,000 particle histories).

• The CUT card :is used to apply energy cuts, which discard particles below a specified energy threshold, thereby improving computational efficiency.

1.2.3.4 Tools Supporting Efficiency Calculation: ANGLE and MEFFTRAN software

In the field of gamma spectrometry, especially when dealing with non-point, extended, or complex samples such as those in Marinelli beakers or high-density matrices like honey, additional tools are required to ensure accurate calculation of detector efficiency. While Monte Carlo simulations provide detailed modeling, software such as ANGLE and MEFF-TRAN are valuable for semi-empirical efficiency prediction and correction of complex effects.

ANGLE (Advanced Nuclear Geometry and Laboratory Efficiency)

is a widely used computational tool designed to calculate the Full Energy Peak Efficiency (FEPE) of gamma-ray detectors. Unlike full Monte Carlo simulations, ANGLE uses the concept of the effective solid angle (ω) combined with empirical and semi-analytical models to determine the efficiency of detectors for a wide variety of sample geometries (cylindrical, disk, Marinelli, etc.) and densities [39]. It operates on the principle of efficiency transfer, meaning it starts with the experimentally calibrated efficiency of a reference source (typically a point source) and applies correction factors to compute the efficiency for a sample of different geometry or composition. This makes it especially useful when simulating complex geometries is computationally expensive or impractical. ANGLE requires [40]: Precise detector geometry, Sample dimensions and density, Elemental composition of the sample, Gamma-ray energies of interest. This tool proved to be particularly helpful in this thesis, as it allowed efficient modeling of the HPGe detector's response to honey samples, and was used to validate and compare with MCNP5 simulation results.

MEFFTRAN (Marinelli Efficiency Transfert)

In gamma-ray spectrometry, especially when analyzing complex geometries such as Marinelli beakers or dense matrices like honey, correction for true coincidence summing (TCS) and matrix effects is essential to ensure measurement accuracy. MEFFTRAN (Matrix Effects Transfer), an analytical software tool, was developed to address these challenges. Originally introduced and refined by Tim vidmar, Bogdan Sima, and collaborators, as part of IAEA-supported projects and international efforts to improve the reliability of gamma-spectrometry in environmental and food monitoring. [10,41] MEFFTRAN provides a fast and reliable method to correct for coincidence summing effects, self-attenuation, and ge-

ometrical efficiencies without the computational burden of full Monte Carlo simulations. It utilizes pre-calculated solid angles, decay schemes of radionuclides, and sample-specific parameters such as density and composition to produce correction factors tailored to each measurement setup. MEFFTRAN is particularly advantageous in routine analyses involving Marinelli beakers, where its efficiency transfer and summing correction capabilities help mitigate the bias introduced by complex sample-detector interactions [10]. In this work, MEFFTRAN was used in parallel with MCNP5 and ANGLE to correct for summing effects and to better understand the influence of matrix composition on measurement accuracy. Its integration helped ensure the reliability of activity calculations, especially in complex honey matrices where attenuation and coincidence summing are significant.

1.2.4 Heavy Metals

Heavy metals are metallic elements with a density greater than 5 g/cm, high relative atomic weight, and remarkable environmental persistence due to their stability and non-biodegradability. These metals are toxic even at low concentrations, posing significant risks to plants, animals, and humans. Anthropogenic activities are the primary drivers of soil contamination with heavy metals [42]. Plants absorb these metals through their roots from contaminated soil and can also accumulate them on external parts, such as leaves and fruits [43].



Figure 1.8: Anthropogenic sources of heavy metal pollution

Heavy metals can be classified into two primary categories based on their biological significance [44–46]:

Table 1.4: Classification of Heavy Metals

Category	Heavy Metals	Biological Role	Toxic Effects
Essential Heavy Metals	Iron (Fe)	Essential for oxygen transport and enzymatic activity.	
	Zinc (Zn)	Involved in enzyme activation and immune function.	excessive concentrations can lead to toxic effects such as headaches, respiratory issues,
	Copper (Cu)	Necessary for energy production and connective tissue formation.	metabolic disturbances, gastrointestinal symptoms,
	Manganese (Mn)	Supports bone formation and antioxidant defense.	Impaired enzyme function, and
	Cobalt (Co)	Integral to vitamin B12 synthesis.	organ damage
	Nickel (Ni)	Contributes to enzymatic functions in trace amounts.	
	Lead (Pb)		Neurological damage, kidney failure, cognitive impairments
Non- Essential Heavy Metals	Mercury (Hg)		Neurotoxicity, kidney damage, developmental disorders
	Cadmium (Cd)	No known beneficial role in biological systems	Renal toxicity, boneRenal toxicity, bonedemineralization, respiratory issues
	Arsenic (As)		Carcinogenic, skin lesions, cardiovascular damage
	Chromium (Cr)		Carcinogenic (especially Cr VI), liver and kidney damage

1.2.5 Heavy metals detection and measurement

Heavy metal contamination in food products, such as honey, is a significant concern due to the potential health risks it poses. The detection and quantification of heavy metals require precise and sensitive analytical techniques.

1.2.5.1 Atomic Absorption Spectroscopy (AAS)

Atomic Absorption Spectroscopy (AAS) is one of the most widely used and reliable techniques for detecting and quantifying heavy metals in various samples, including food products, environmental samples, and industrial effluents. This analytical method relies on the absorption of light by atoms in the gaseous state, making it ideal for measuring trace concentrations of metals [42].

1.2.5.2 Principle of Atomic Absorption Spectroscopy (AAS)

AAS is based on the principle that free atoms absorb light at specific wavelengths that are characteristic of each element. When a sample containing metal ions is introduced into a high-temperature flame or furnace, the metal ions are converted into free atoms. These atoms absorb light emitted by a light source (typically a hollow cathode lamp) at a characteristic wavelength for each metal. The amount of light absorbed is proportional to the concentration of the metal in the sample [47]. The absorbed light is measured by a photodetector, and the concentration of the metal is determined by comparing the absorbance with that of a calibration curve constructed using standards of known concentration [48].

1.2.5.3 Instrumentation and Components of AAS

• 1. Atomizer:

The atomizer is the component responsible for converting the sample into free atoms. There are two types of atomizers commonly used in AAS:

- 2. Light Source (Hollow Cathode Lamp): A hollow cathode lamp (HCL) is used as the light source. It contains a cathode made of the element to be analyzed (e.g., copper, zinc, lead) and emits light at a specific wavelength characteristic of that metal. Each metal has its own specific wavelength, which is crucial for selective detection [49].
- 3. Monochromator: is used to isolate the specific wavelength of light absorbed by the metal of interest. It ensures that only the wavelength corresponding to the metal being analyzed is transmitted to the detector, filtering out other wavelengths [50].
- 4. Detector: The detector measures the intensity of the transmitted light. When atoms of the metal absorb light, the amount of light passing through the sample decreases. The detector quantifies this reduction in light intensity, and the absorbance is then calculated [51].

• 5. Readout System: The absorbance data is processed by a computer or readout system. The absorbance is compared to a calibration curve obtained from standard solutions of known concentrations of the metal, allowing for the determination of the metal concentration in the sample [52].

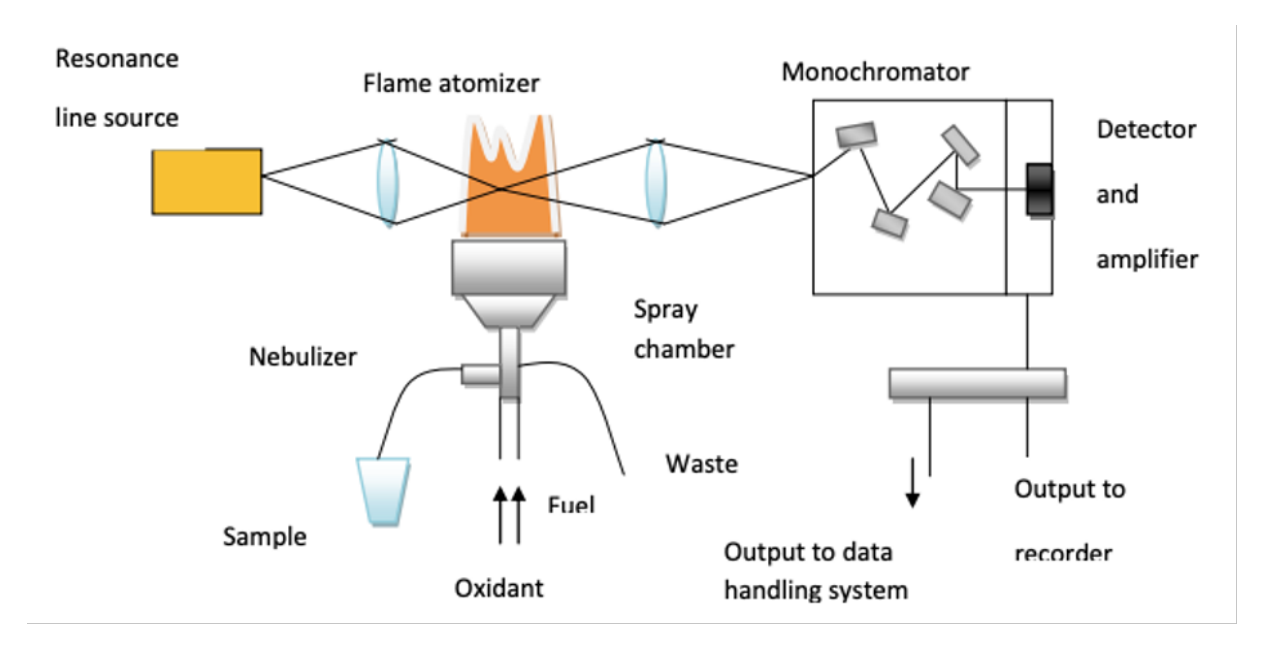


Figure 1.9: Atomic Absorption Spectroscopy (AAS) Mechanism Overview

1.2.5.4 Working Process of AAS

- 1. Sample Introduction The sample, typically dissolved in a suitable solvent, is introduced into the atomizer (flame or furnace). This is typically done using a nebulizer, which generates an aerosol from the sample solution [53]. 2. Atomization In the atomizer, the solvent evaporates, leaving behind the metal in the form of free atoms. These atoms then absorb the light emitted by the hollow cathode lamp [54].
 - Flame Atomizer: In this method, the sample is introduced into a flame, where it is heated to a high temperature (typically 2000to 3000to atomize the sample. The flame is typically composed of a mixture of acetylene and air or acetylene and nitrous oxide [48].
 - Graphite Furnace Atomizer: This atomizer uses a graphite tube that is heated to high temperatures (up to 3000) to atomize the sample. It is particularly useful for detecting metals in very low concentrations (trace levels) and is more sensitive than the flame atomizer [55].

3. Light Absorption and Measurement As the atoms absorb the light, the amount of light passing through the sample is reduced. The reduction in light intensity is measured by the detector, which is proportional to the concentration of the metal in the sample [56].

4. Calibration and Quantification A calibration curve is constructed using standards of known concentration of the metal. The absorbance data from the sample is plotted against the known standards to determine the concentration of the metal in the unknown sample [47].

1.2.6 Antimicrobial Residues

In addition to radioactivity and heavy metals, antimicrobial residues, including antibiotics represent another significant contaminant in honey, primarily introduced through beekeeping practices. Beekeepers often use antibiotics, such as tetracyclines, sulfonamides, and streptomycin, to prevent or treat bacterial infections in honeybee colonies, including diseases like American and European foulbrood [57,58]. While these measures protect hive health, the excessive or improper use of antibiotics can result in their residues being transferred to honey [59]. Antibiotics in honey pose potential health risks to consumers, including allergic reactions, toxicity, and the development of antibiotic-resistant bacteria [60]. Regulatory bodies have established maximum residue limits (MRLs) for antibiotics in honey to ensure safety. However, contamination can also occur from environmental exposure, such as antibiotic-laden runoff from agricultural activities [61].

Antibiotic Group	Examples	Target Pathogens/Disease	Mode of Action	Residue Risks in Honey	Regulatory Status
Tetracyclines	Oxytetracycline, Chlortetracy- cline	American/European Foulbrood	Inhibits bacterial protein synthesis	Allergic reactions, antimicrobial resistance	MRLs set in EU and globally regulated
Sulfonamides	Sulfathiazole, Sulfamethoxa- zole	General bacterial infections	Inhibits folic acid synthesis	Toxicity, environmental persistence	Banned for use in many regions
Streptomycin	Streptomycin	Bacterial infections	Inhibits bacterial protein synthesis	Resistance development, potential toxicity	Usage banned in most countries

Table 1.5: Commonly Used Antibiotics in Beekeeping

1.2.7 Antimicrobial residues detection and measurement

The detection of antibiotic residues in food products is crucial for ensuring consumer safety and preventing antimicrobial resistance. Various analytical techniques are used for this purpose, including Charm II, ELISA (Enzyme-Linked Immunosorbent Assay), HPLC

(High-Performance Liquid Chromatography), and LC-MS/MS (Liquid Chromatography-Tandem Mass Spectrometry). These methods help identify and quantify antibiotic traces in honey, milk, meat, and other food items. Rapid screening tests like Charm II provide quick and cost-effective results, while advanced chromatographic techniques offer high sensitivity and specificity.

1.2.7.1 What is the CHARM Technique?

The CHARM II radio receptor assay technique developed by Charm Sciences Inc, technique is a rapid screening test used for detecting antimicrobial residues such as beta-lactams, sulfonamides, tetracyclines, chloramphenicol, quinolones, macrolides and aminoglycosides, in food products such as milk, honey, meat, and animal feed. It ensures food safety by identifying residues at trace levels, even below regulatory limits, providing both qualitative (presence/absence) and quantitative (concentration) results. It is widely used in food safety testing due to its high sensitivity, ease of use, and reliability [62].

1.2.7.2 Principle of CHARM

The CHARM technique is based on a radiolabeled competitive binding assay, utilizing microbial cells with specific receptor sites that bind antimicrobial drugs. During the analytical process, a sample extract is combined with a binder and a radiolabeled antimicrobial tracer (³H or ¹⁴C). If antimicrobial residues are present in the sample, they compete with the radiolabeled tracer for binding to the receptor sites. The amount of tracer bound to the receptor sites is then measured and compared to a predetermined control point. Since the binding is competitive, a higher concentration of antimicrobial residues in the sample results in less tracer binding, while a lower concentration of antimicrobial residues leads to more tracer being detected [63]. *How it works [50,52]

- Sample Preparation: A small amount of the food sample (e.g., honey, milk, meat) is extracted using a solvent or buffer solution. The extract is then filtered or treated to remove impurities that could interfere with the test.
- Addition of Binding Components: The sample extract is mixed with a microbial receptor binder that has specific sites for antimicrobial drugs. A radiolabeled antimicrobial tracer (³H or ¹⁴C-labeled) is also added.
- Competition for Binding Sites: If the sample contains antimicrobial residues, they compete with the radiolabeled tracer for binding to the receptor sites. Higher antimicrobial concentrations in the sample result in less tracer binding, while lower antimicrobial levels allow more tracer to bind.

- Separation and Measurement: After incubation, unbound tracer is washed away, leaving only the tracer bound to receptor sites. The amount of bound radiolabeled antimicrobial is measured using liquid scintillation counting or another radiation detection method.
- Interpretation of Results: The measured radioactivity is compared to a control sample. High radioactivity = fewer antimicrobial residues. Low radioactivity = higher antimicrobial content.
- Decision on Sample Safety: The results are compared to established Maximum Residue Limits (MRLs) set by regulatory bodies (e.g., FDA, EU, Codex). If antimicrobial levels exceed the allowable limit, the food is considered unsafe.

1.3 Contamination Pathways and Mechanisms

Contaminants such as radioactivity, heavy metals, and antimicrobials can enter the environment and subsequently impact honey through various pathways and mechanisms. Understanding these pathways is crucial to addressing contamination and safeguarding both honey quality and public health.

A. Soil, Air and Water Contamination

. Heavy metals: released into the atmosphere and soil through industrial discharges, mining activities, pesticide use, and wastewater irrigation, persist and accumulate in the environment. Plants absorb these metals through their roots or from deposits on their surfaces. Contaminated water bodies and soil further transfer metals to be be where they accumulate in nectar and pollen consumed by bees [64,65].

Radioactivity:Radioactive isotopes from nuclear fallout, improper waste disposal, or natural sources can contaminate groundwater and soil ecosystems. These radioactive particles enter the environment through multiple pathways: they can be absorbed by plant roots and incorporated into tissues, or settle as aerosols directly on vegetation surfaces and water sources. Bees become exposed through both routes - by consuming contaminated water [66] and collecting contaminated pollen and nectar from treated plants.

Antibiotics: used in agricultural and veterinary practices can leach into the soil and water or air from agricultural sprays, potentially entering plants or affecting bees directly when they forage [67].

B. Direct Exposure through Beekeeping Practices

Inadequate or improper use of chemicals in apiculture contributes directly to honey contamination.

- Antibiotics: Beekeepers sometimes use antibiotics like tetracyclines and sulfonamides to prevent or treat bacterial infections in bee colonies. Residues of these antibiotics can persist in honey if not used responsibly [58].
- **Pesticides:** The use of pesticides in hive management to control pests like Varroa mites (parasite attacks bees) may lead to contamination if residues are not adequately controlled [68].

1.4 Bioaccumulation and Biomagnification

Contaminants entering ecosystems often accumulate in organisms and magnify as they move up the food chain [69]. Bees can accumulate heavy metals from repeated exposure to contaminated nectar, pollen, and water. These metals are stored in their bodies and transferred to honey and other hive products. Radioactive isotopes such as ¹³⁷Cs and ⁹⁰Sr, present in the environment, may bioaccumulate in bees and affect honey safety. Honey contamination can also occur during processing and storage if equipment or containers are made of materials containing heavy metals or are improperly sanitized [70].

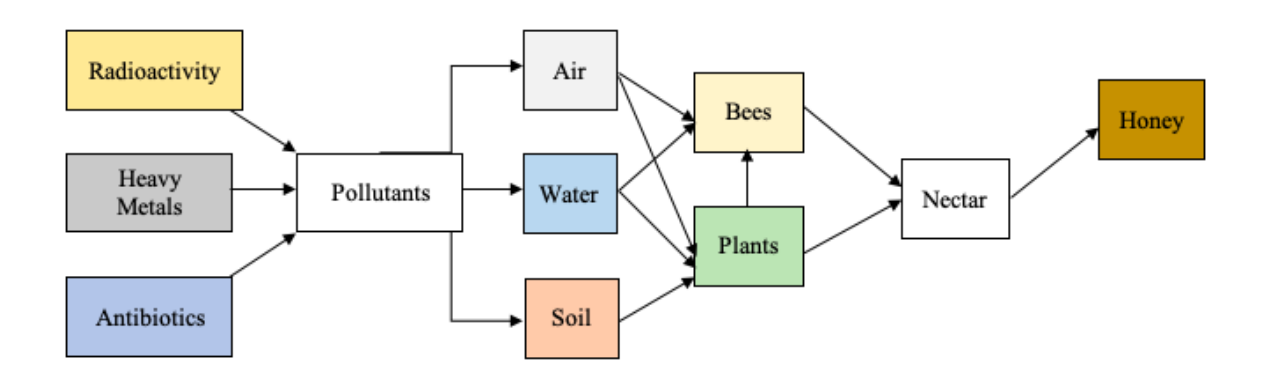


Figure 1.10: Schema of Honey Contamination: From Source to Exposure

Chapter 2

Monte Carlo Simulation and Detector Efficiency Modeling

2.1 Introduction

The integration of experimental measurements and simulations provides valuable insights into the capabilities and limitations of gamma-ray spectrometry, particularly within a defined energy range. Accurate quantification of radioactivity levels requires a comprehensive understanding of the detector's Full Energy Peak Efficiency (FEPE), which is influenced by measurement conditions such as source-detector geometry and various detector parameters, including detector type (semiconductor, scintillation, or solid state), as well as the density and size of the detector material [71]. Efficiency calibration is typically performed using standard radioactive sources that closely match the sample in geometric dimensions, density, and chemical composition. However, achieving these ideal conditions is often challenging, particularly for environmental samples [72]. Computational techniques help address these challenges by employing Monte Carlo-based simulation tools, which account for all physical processes—from photon emission to its interaction with the detector—thereby optimizing calibration procedures and reducing reliance on radioactive standards. Additionally, this approach minimizes calculation errors caused by approximations in experimental calibration while eliminating the need for constraints or assumptions regarding the source-detector geometric configuration [73]. In this chapter, the simulation methodology employed to determine the full energy peak efficiency (FEPE) which is a critical parameter for calculating the activity concentration of honey samples, as it directly influences the accuracy of gamma-ray spectrometry measurements [74]. Two software tools were utilized for this purpose: MCNP 5 code (Monte Carlo N-Particle) and ANGLE software. The rationale for using these codes, their theoretical foundations, and

their application in this study are discussed. Specifically, ANGLE was used to complement the MCNP 5 simulations by providing an independent calculation of the FEPE, enabling cross-validation of the results obtained from MCNP 5.

2.2 Gamma Spectrometry Experimental Setup

The gamma spectrometry chain used in this study is composed of a high purity Germanium (HPGe) detector, connected to an analog Nuclear instrument modules (NIM) system (preamplifier, high-voltage-power supply, amplifier, multichannel analyzer) from Ortec industries, the latter allows to amplify, adjust and process the pulses delivered by the detector. The spectra are visualized on a computer which are then processed by a Gamma Vision software. Figure 2.1 shows the experimental device used in this study.







Figure 2.1: Experimental device of gamma spectrometry used

2.2.1 Detector features

A low-background gamma-spectrometer with a coaxial p-type HPGe detector with a carbon fiber end-cap window (GEM-C5060-S ORTEC Industries) has been used in this study. they have a low average atomic number, which results in good transmission of low-energy photons. The HPGe detector has an efficiency of 35%relative to a standard 3 inch× 3 inch NaI(Tl) detector with an energy resolution of 1.7 keV for the ⁶⁰Co gamma-ray at 1.332 MeV, and the peak-to Compton ratio is 62:1. For achieving the low background needed in environmental applications, the detector was installed in a lead shielding (AT1320 ATOMTEX model) [75].

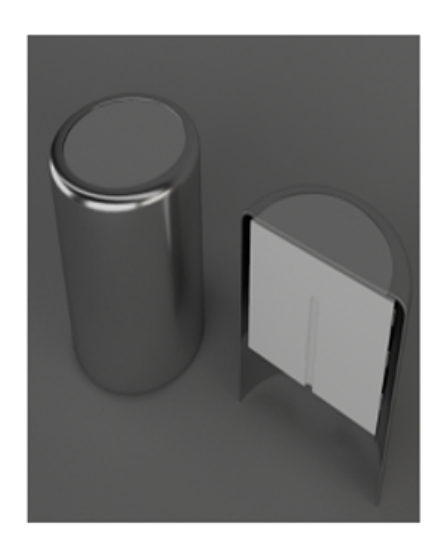




Figure 2.2: A radio X for the detector used

2.3 Calibration of the Measurement Chain

2.3.1 Energy Calibration

The first step before any measurements is the energy calibration of the gamma-ray spectrometry chain. Energy calibration involves establishing the relationship between the energy of gamma rays and the corresponding channel numbers in the spectrum.

For this purpose, the spectrometry chain was calibrated using a ¹⁵²Eu source. This radionuclide emits multiple gamma rays with varying probabilities, making it valuable for detector calibration. Some of the most intense gamma-ray emissions include 121.78 keV (28.53%), 244.70 keV (7.54%), 344.28 keV (26.59%), 778.90 keV (12.97%), 964.08 keV (14.55%), 1112.07 keV (13.64%), and 1408.01 keV (20.85%). Other notable emissions occur at 411.12 keV (2.24%), 444.00 keV (3.13%), 867.38 keV (4.23%), 1085.87 keV (10.13%), 1212.95 keV (1.43%), and 1299.14 keV (1.64%). These gamma rays cover a broad energy range, enabling precise detector calibration and validation under various measurement conditions.

Table 2.1: Gamma Energies	, Emission Probabilities, and	Corresponding Channel Numbers
---------------------------	-------------------------------	-------------------------------

Energy (keV)	Emission Probability (%)	Channel
121.78	28.53	243
344.28	26.59	689
778.90	12.97	1558
964.08	14.55	1929
1112.07	13.64	2225
1408.01	20.85	2816

The gamma spectrum was recorded over a 3600-second period, using 8192 channels with an energy width of 0.5 keV per channel, and analyzed with Gamma Vision software. The energy calibration line of the measurement chain is given in figure 2.3.

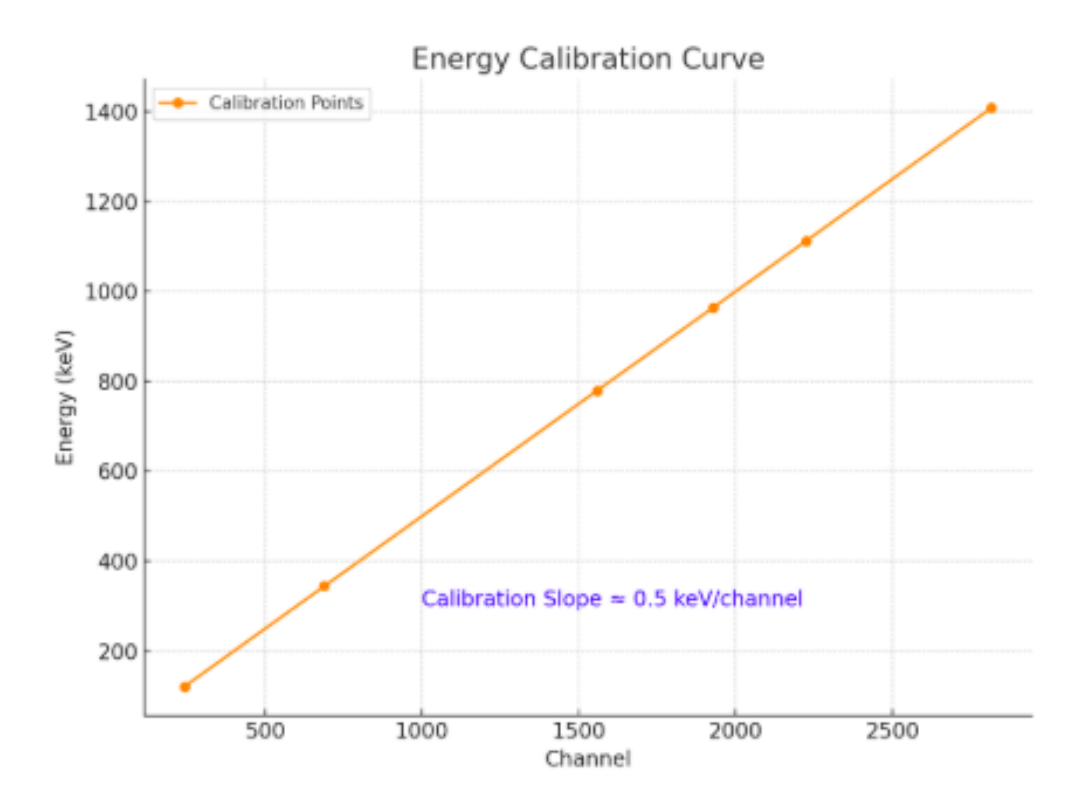


Figure 2.3: Energy calibration curve

2.3.2 Efficiency calibration for Point Source

The first measurement consisted in determining the detector's efficiency using a point source of ¹⁵²Eu at a distance of 14cm. The measurement time is chosen to be equal to 10000 seconds; the dead time recorded during the entire counting time was less than 2%. In this study, we were interested in an energy range from 121 keV to 1408 keV. The figure below 2.4 shows the experimental spectrum of ¹⁵²Eu point source

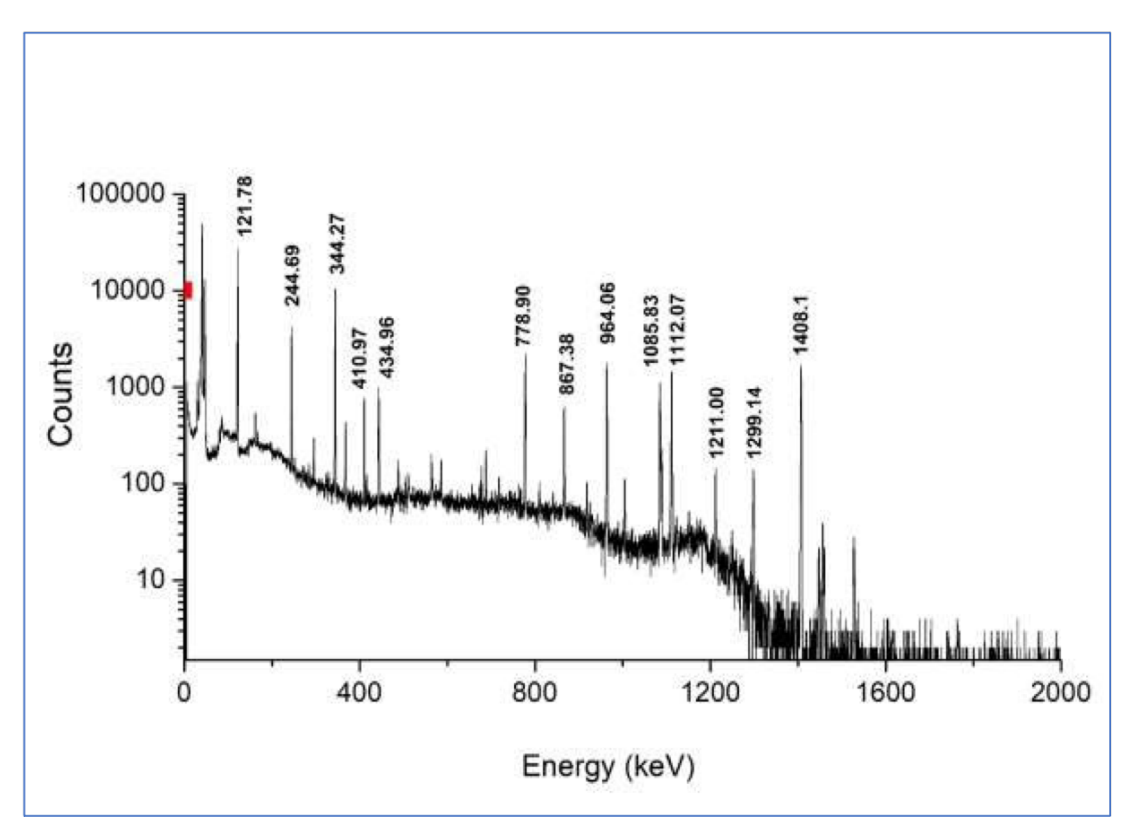


Figure 2.4: Experimental spectrum of ¹⁵²Eu point source

The intrinsic efficiency measured is given by the following expression:

$$\varepsilon_{\rm int} = \frac{N}{A \cdot I_{\gamma} \cdot T_c \cdot \left(\frac{\Omega}{4\pi}\right)} \tag{2.1}$$

where the solid angle Ω is given by:

$$\Omega = 2\pi \left(1 - \frac{d}{\sqrt{R^2 + d^2}} \right) \tag{2.2}$$

d: Source-detector distance; R: Collimator radius; N: Total absorption peak area; Tc: Counting time; A: Source activity; I_{γ} : is the photon emission probability the detector efficiency for a source-detector distance of 14 cm, chosen to reduce coincidence is shown in figure 2.5.

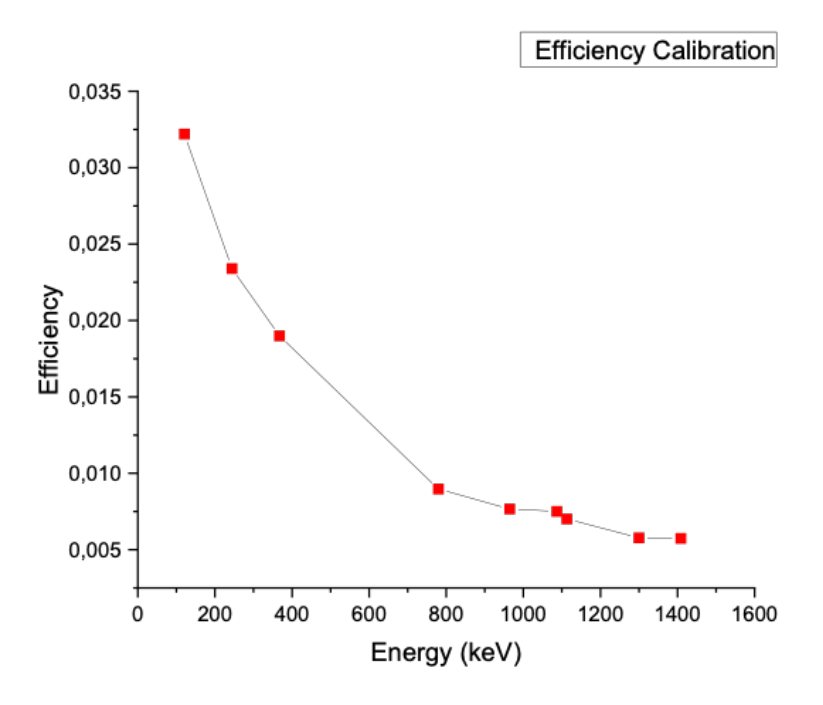


Figure 2.5: efficiency calibration curve

2.4 Simulations using the Monte Carlo MCNP5 Code

2.4.1 Modeling the detector geometry

Each code necessitates specific input files for accurate calculations. In the initial phase, it is crucial to input the geometrical parameters of the detector, including the dimensions of the germanium crystal and the thickness of the dead layer, as provided by the manufacturer (ORTEC). These parameters are detailed in figure 2.6.

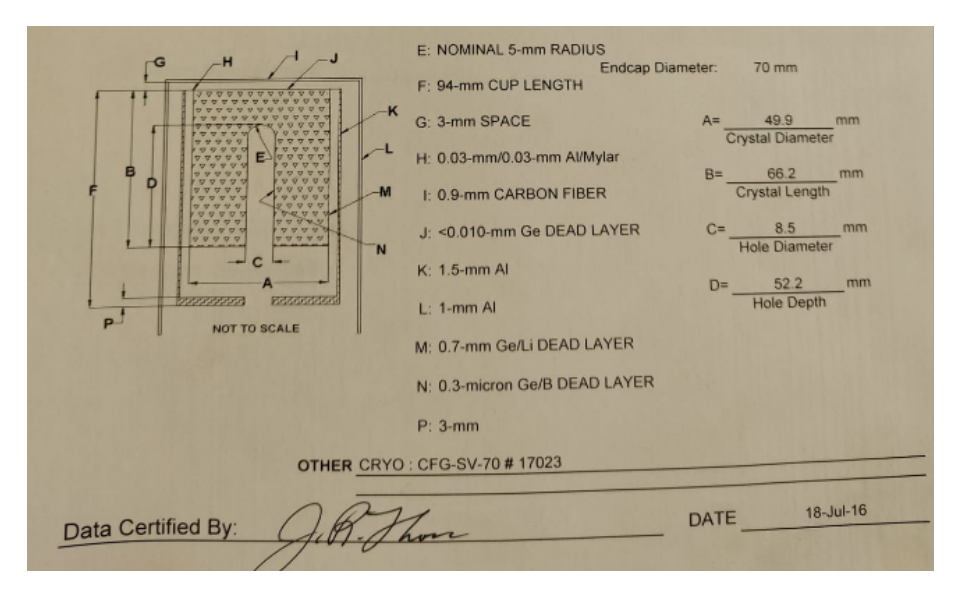


Figure 2.6: the dimensions of the detector as supplied by the manufacturer

The simulation of the source-detector geometry was performed using the MCNP5 code, operating in the PE mode (photon and electron mode). This mode is particularly recommended for the transport of low-energy photons [33]. To ensure comprehensive modeling of photon interactions with the germanium crystal, the cutoff energy for photons was set to 1 keV. This allowed for the inclusion of all relevant interaction mechanisms, such as photoelectric absorption, Compton scattering, and pair production for high-energy photons. A total of 10⁸ particles were simulated to achieve a statistical error of less than 1% in the results. The number of bins used was 8192. based on the energy calibration obtained from the experiment The F8 tally for photons and electrons was used to collect the deposited energy in the active crystal, generating the Pulse Height Distribution (PHD) per emitted gamma particle [76]. To simulate realistic detector performance, the energy resolution was modeled using the Gaussian Energy Broadening (GEB) card, which accounts for the statistical fluctuations in energy deposition and produces a more accurate spectrum. The GEB card parameters were obtained from the experimental spectrum by fitting the full width at half maximum (FWHM) using the following expression:

$$FWHM = a + b\sqrt{E + cE^2}$$
 (2.3)

Where E is the energy of the photon (MeV), a=0.00095124 MeV, b=0.001330 MeV2 and c=0. These constants are determined by mathematical regression from the experimental data [75]. The simulated efficiency for the photon energy E is determined as follows [77]:

$$\varepsilon_{\text{simulated}} = \frac{N_p(E)}{N(E)}$$
 (2.4)

Where $N_p(E)$ represents the number of photons that deposited their energy in the detector at the energy E, and N(E) is the total number of photons emitted from the source. Once the input file is built, the MCNP5 code offers the possibility to visualize the modeled geometry using a software called VISED PLOTTING, which allows to check the geometry before launching the execution of the file. All the geometric information present in the input file has been verified using this visualization program.

2.4.2 Initial Model Based on Manufacturer Specifications

In the first simulation experiment, we simulated a point sources of ¹³³Ba and ¹⁵²Eu using the detector dimensions provided by the manufacturer (as shown in figure 2.6. The results revealed that the simulated detector model, based only on the manufacturer's specifications, could not reproduce the experimental measurements with acceptable accuracy. The primary results of the simulation were compared with the experimental ones and considerable discrepancies exceeded 60% were observed (figure 2.7), especially in the low energy range. Since the dead layers thicknesses are not always precisely provided by the manufacturer and even can change during detector aging.

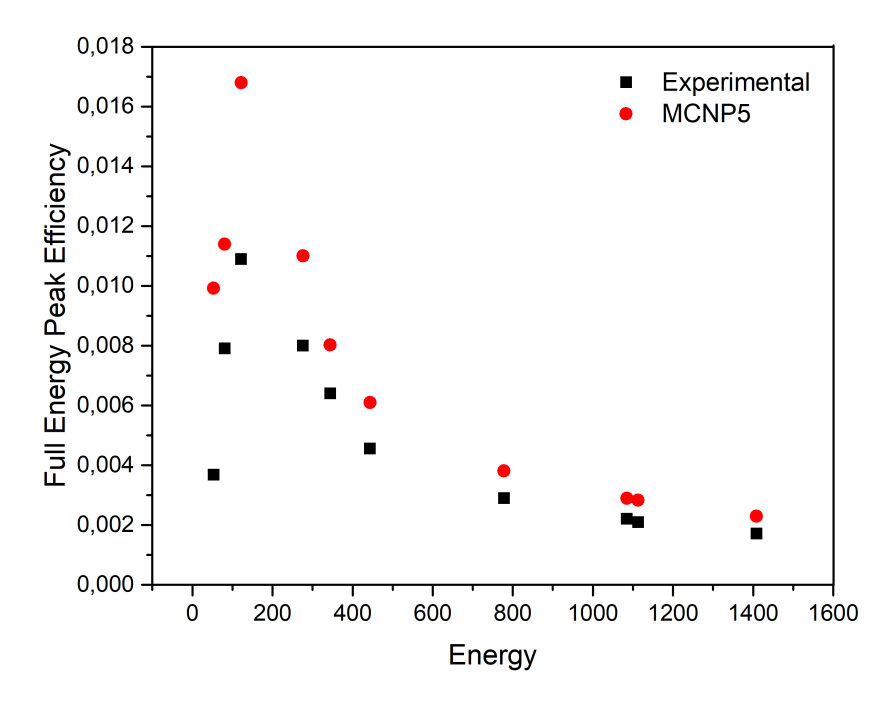


Figure 2.7: Comparison of Experimental Full-Energy Peak Efficiency (FEPE) with the simulated by the Manufacturer's dimensions

2.4.3 Germanium Crystal Dead Layer Adjustment

Since our detector is a p-type HPGe, its outer layer is composed of lithium. Over time, the thickness of the dead layer increases as a result of lithium diffusion, which affects the detector's response. Therefore, it became necessary to adjust and optimize the dead layer dimensions in the simulation to achieve better agreement with the experimental data. For this purpose, the measurements were conducted using two gamma energies: 59.5 keV from ²⁴¹Am and 661.6 keV from ¹³⁷Cs at for positions (one directly in front of the detector and three around the detector).

These energies were chosen to probe both the external and internal dead layers of the crystal. The gamma ray at 59.5 keV with its short mean free path in germanium, is sensitive to the external dead layer, while the gamma ray at 661.6 keV with a longer mean free path (26.5 mm), penetrates deeper into the crystal, allowing for the characterization of the internal dead layer.

The adjustment procedure used to estimate the thickness of the dead layer in the germanium crystal involves incrementally increasing the dead layer thickness, starting from the initial value (provided by the manufacturer) up to its optimized final value (see table 2.2).

. At each step, the measured intrinsic efficiency is compared with the Monte Carlo simulation results obtained at four selected locations. The calculation procedure stops when the average difference between the calculated and measured intrinsic efficiencies becomes less than 5%. The detector geometry modeled is illustrated in figure 2.8.

 $\textbf{Table 2.2:} \ \ \textbf{The HPGe parameters provided by the manufacturer and values from the optimized model}$

[75]

Parameters	Manufacturer Model	Optimized Model		
Aluminum Cryostat				
Endcap diameter	70 mm	70 mm		
Cup length	94 mm	94 mm		
Thickness	$1 \mathrm{\ mm}$	$1~\mathrm{mm}$		
Window to crystal distance	3 mm	3 mm		
Carbon fiber window	$0.9 \mathrm{\ mm}$	$0.9 \mathrm{\ mm}$		
Germanium Crystal				
Crystal diameter	49.9 mm	49.9 mm		
Crystal length	66.2 mm	$66.2 \mathrm{\ mm}$		
Ge/Li dead layer	$0.7 \mathrm{mm}$	$0.81 \mathrm{\ mm}$		
Ge/B dead layer	$0.0003~\mathrm{mm}$	$0.0003~\mathrm{mm}$		
Core Hole				
Hole diameter	$8.5 \mathrm{\ mm}$	$8.5~\mathrm{mm}$		
Hole depth	52.2 mm	$52.2 \mathrm{\ mm}$		
Aluminum Holder				
Holder thickness	1.5 mm	1.5 mm		
Aluminum/Mylar thickness	$0.03~\mathrm{mm}~/~0.03~\mathrm{mm}$	$0.03~\mathrm{mm}~/~0.03~\mathrm{mm}$		

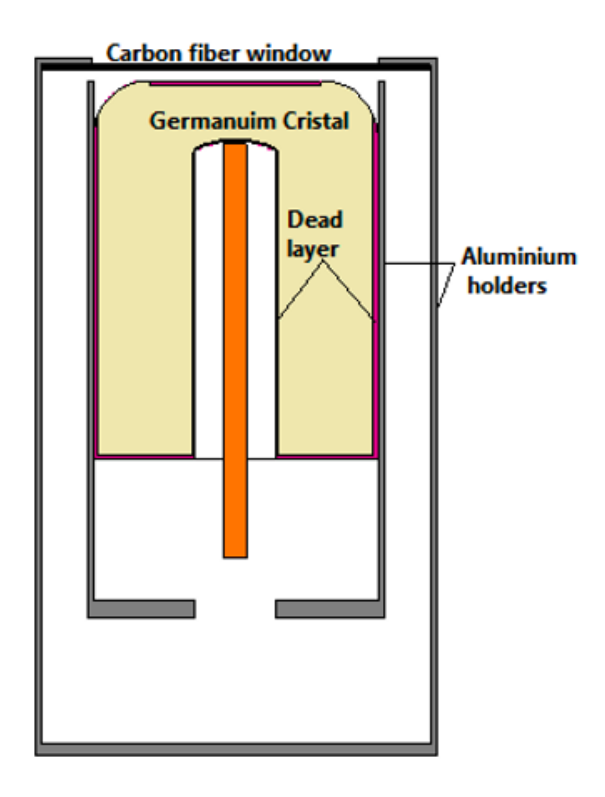


Figure 2.8: the detector modeled by the MCNP 5 code

After adjusting the thicknesses of the front and rear dead layers by a step by-step procedure, a good agreement was achieved between simulated and experimental efficiencies (relative discrepancies decreased to 3%).

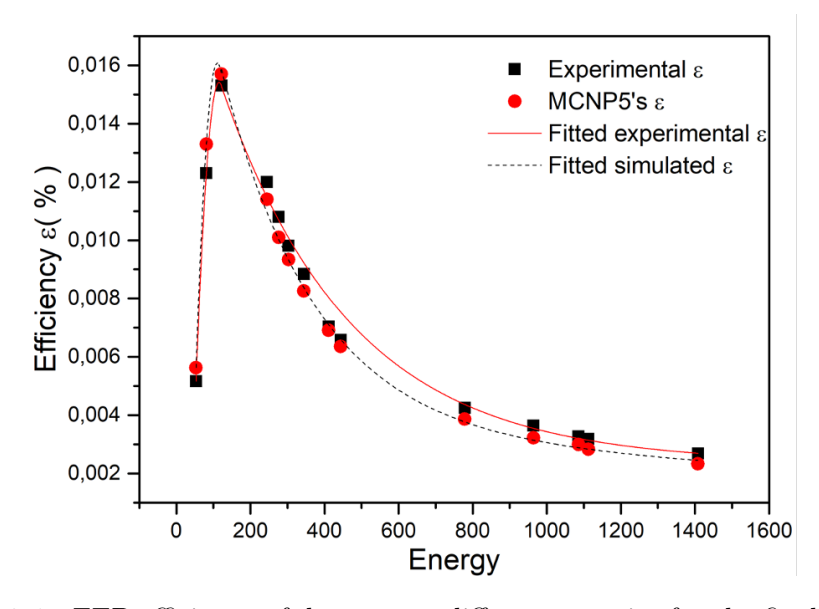


Figure 2.9: FEP efficiency of detector at different energies for the final model

2.4.4 Influence of Cross-Section Libraries on Efficiency Calculations

Despite extensive research in gamma spectrometry and detector modeling, there remains limited knowledge regarding how the interaction probability between photons and the detector material affects the overall effectiveness of the measurement system. One of the critical parameters governing this interaction is the photon cross-section, which plays a significant role in determining the detector's absolute efficiency. Variations in cross-section values directly influence the accuracy of simulated efficiency, as they alter the likelihood of photon interactions within the detector material [26].

To investigate this effect, two different cross-section libraries were employed in simulations using the MCNP5 code: ENDF/B-VI (Evaluated Nuclear Data File) and JENDL-5 (Japanese Evaluated Nuclear Data Library). These libraries were processed into ACE (A Compact ENDF) format files using NJOY16.65.j5 [78]. The ACE format is specifically optimized for Monte Carlo simulations, allowing efficient and accurate modeling of particle interactions based on evaluated nuclear data.

A comparative analysis of the two libraries was performed to evaluate the extent to which the choice of nuclear data file affects the calculated efficiency results. This comparison highlights that the cross-section data significantly impacts the detector response, particularly at lower photon energies, where interaction mechanisms such as photoelectric absorption and scattering become more complex. The findings underscore the importance of selecting an appropriate nuclear data library based on the energy range of interest to ensure accurate simulation results and reliable efficiency calibration [75].

2.4.5 Marinelli Beaker Geometry

Environmental samples of very low radioactivity are often measured in specially designed containers to ensure maximum detection efficiency, called Marinelli beaker geometry which have the following characteristics [79]:

- They are made of materials with low absorption of gamma rays.
- Having an internal hollow volume to the shape of the detector for maximum efficiency.
- Airtight and not reacting with the sample content, having a wide-neck opening to facilitate their closures.

These containers have been designed to make the sample-detector geometry as symmetrical as possible and to increase the solid angle between the sample and the detector. Marinelli beaker containers have lids with a unique locking design that excludes any spillage or leakage of the sample material. The schematic and dimensions of the Marinelli

beaker container used in this work are shown in the following figure.

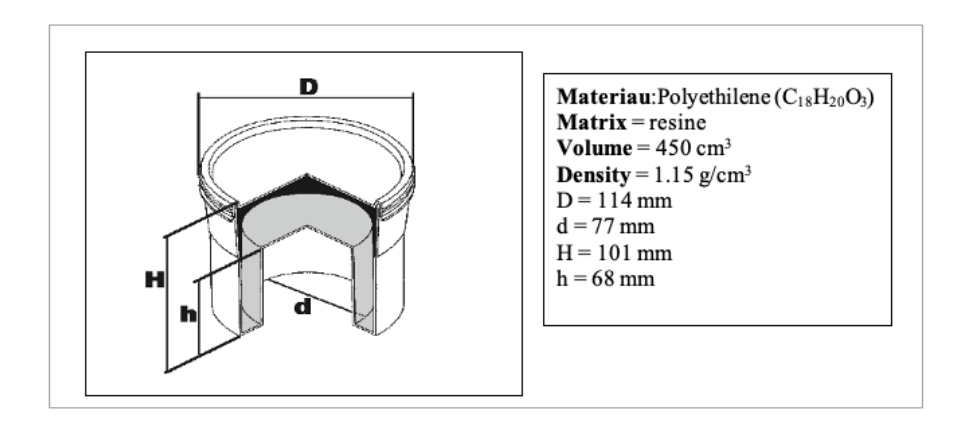


Figure 2.10: Marinelli beaker source geometry

2.4.6 Modeling of Detector Efficiency for a Marinelli Source

To simulate the efficiency of the detector for honey samples, it is necessary to use standard sources whose nature and shape are similar to those of the sample being analyzed, due to the complexity of the honey matrix and the variability of its density. These sources must have a composition close to the density and elemental composition of honey. In this study, two multi-gamma ray sources, $^{133}\mathrm{Ba}$ and $^{152}\mathrm{Eu},$ were used. These sources were packed in Marinelli beakers filled with epoxy resin (chemical formula C18H20O₃), which closely mimics the density and geometry of the honey samples. The resin's composition and physical properties ensure a faithful reproduction of the photon attenuation and scattering behavior within the matrix, thus improving the accuracy of the efficiency calibration. Gamma spectra were acquired using Gamma Vision software, with an acquisition time of 100,000 seconds, carefully adjusted according to the activity of the sources to maintain a statistical uncertainty of less than 1% on the peak area. Background spectra were collected over the same duration to ensure accurate background subtraction. The net area of each gamma peak was determined by subtracting the background contribution using Gamma Vision. The resulting detector response spectra were exported to OriginPro 2021 for further processing and comparison with simulated spectra on the same energy scale. In OriginPro, the Quick Peaks gadget was used for intuitive peak identification, while the Peak Analyzer tool enabled advanced peak fitting and deconvolution to resolve overlapping peaks. This facilitated a more precise evaluation of the measured data against the simulation. The complete analysis setup was saved as a reusable theme within Peak Analyzer for reproducibility and future batch processing. Spectra were recorded using 8192 channels, with an energy resolution of 0.5 keV per channel, enabling detection of photons in an energy range from 53 keV to 1408 keV. The experimental full-energy peak efficiency (FEPE) is given by [80]:

$$\varepsilon_{\rm exp} = \frac{N}{T_c \cdot A \cdot P_{\gamma} \cdot C_f} \tag{2.5}$$

where:

- N is the number of net counts under the peak,
- A is the source activity (in Bq), calculated as $A(t) = A_0 e^{-\frac{\ln 2}{t_{1/2}}t}$,
- T_c is the counting time (in seconds),
- P_{γ} is the photon emission probability,
- ullet C_f is the true coincidence summing correction factor.

The absolute uncertainty in the experimental efficiency is given by [81]:

$$\Delta \varepsilon = \varepsilon_{\text{exp}} \cdot \sqrt{\left(\frac{\Delta N}{N}\right)^2 + \left(\frac{\Delta A}{A}\right)^2 + \left(\frac{\Delta P_{\gamma}}{P_{\gamma}}\right)^2 + \left(\frac{\Delta C_f}{C_f}\right)^2 + \left(\frac{\Delta T_c}{T_c}\right)^2}$$
 (2.6)

To develop a realistic detector simulation, the input file was meticulously prepared to include all essential data describing the experimental setup. This involved specifying the high-precision geometry, dimensions, and material properties of the detector, sample container, and lead shielding. These details were comprehensively defined in the cell, surface, and material cards of the input file, which comprised 18 cells and 51 surfaces. Figure 2.11 presents the simulated HPGe detector by MCNP5 code with the Marinelli beaker placed in the lead shielding.

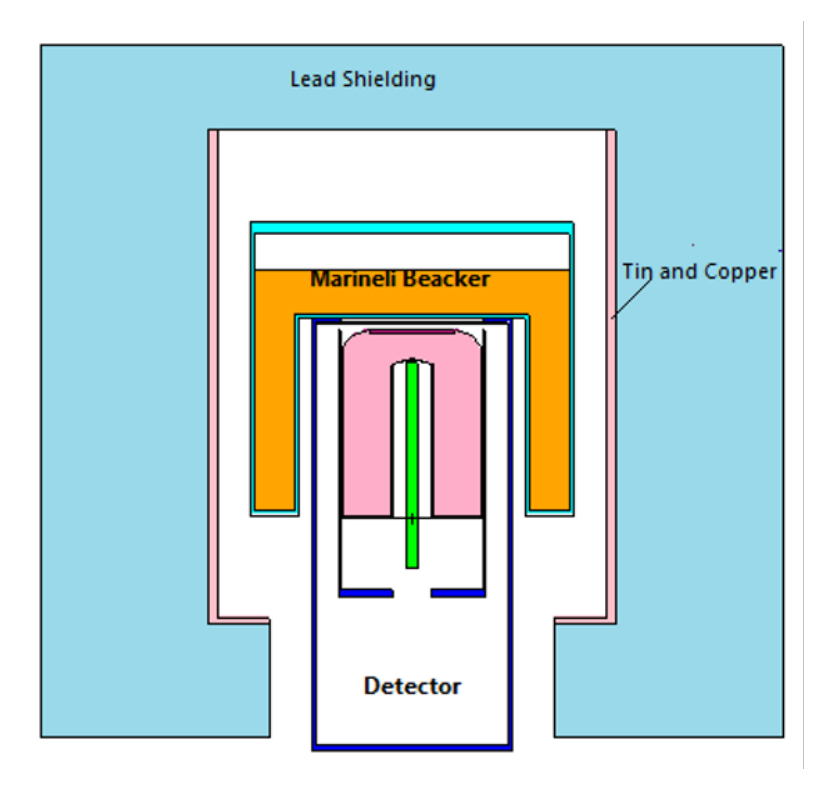


Figure 2.11: the simulated HPGe detector by MCNP5 code with the Marinelli beaker placed in the lead shielding

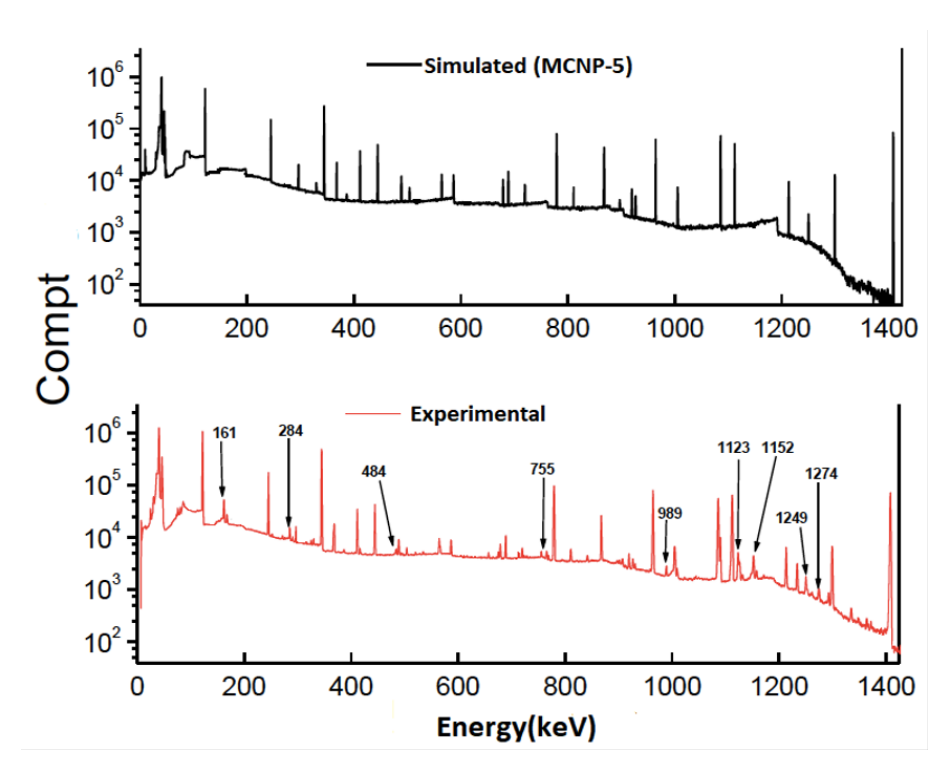


Figure 2.12: Comparison of the Experimental and Simulated Spectrum of the 152 Eu Source in Marinelli Beaker Geometry Using MCNP5

As shown in Figure 2.12, there is excellent agreement between the simulated spectrum (based on the optimized HPGe detector model) and the experimental measurement, both in terms of peak resolution and the shape of the Compton plateau. This agreement provides strong validation for the optimized HPGe detector geometry under environmental analysis conditions. However, a careful comparison between the experimental spectrum and the simulated spectrum (MCNP5) reveals the presence of several virtual peaks in the experimental spectrum that do not correspond to the emissions of the ¹⁵²Eu calibration source. These virtual peaks are primarily due to the influence of coincidence summing effects. Among the sum peaks observed in the experimental spectrum, various shapes and degrees of summing effects can be distinguished, including: 1. Virtual peaks corresponding to the respective coincidences between gamma-gamma radiation of ¹⁵²Eu:

- Virtual peak at 755 keV from the sum of (411 keV with 344 keV)
 - Virtual peak at 989 keV from the sum of (121 keV with 867 keV)
 - Virtual peak at 1123 keV from the sum of (344 keV with 779 keV)
- 2. The peaks sum with the combination of X-rays; 40 keV and 45 keV from the K-shell during the decay of ¹⁵²Eu to ¹⁵²Sm, with the gamma emissions of ¹⁵²Eu:
 - Virtual peak at 161 keV from the sum of (121 keV + 40keV)
 - Virtual peak at 284 keV from the sum of (244 keV +40keV)
 - Virtual peak at 484 keV from the sum of (443 keV + 40 keV)
- 3. We also have the emergence of coincidence peaks with a triple summation, Gamma-Gamma-X-ray:
 - Virtual peak at 1152 keV from the sum of (121.8 keV + 1085keV + 40 keV X-ray)
 - \bullet Virtual peak at 1274 keV from the sum of (121.8 keV + 964 keV + 40 keV X-ray)
 - Virtual peak at 1249 keV from the sum of (244.7 keV + 964 keV + 40 keV X-ray)

The presence of these virtual peaks leads to a noticeable increase or decrease in the number of counts in the real photoelectric peaks corresponding to the emissions of the source. This distortion affects the accuracy of the detection efficiency measurements as a function of energy, ultimately compromising the reliability of quantitative calculations for the analyzed samples. To address this issue, corrections for coincidence summing effects are essential to achieve high-precision measurements in the determination of radionuclide activity. These corrections ensure the accuracy and reliability of the gamma spectrometry results, particularly in complex measurement scenarios.

2.4.7 True Coincidence Summing Effects

The multi-energy gamma-ray emissions of ¹⁵²Eu and ¹³³Ba make them ideal for calibrating gamma-ray detectors over a broad energy range 53-1408 keV. However, their complex

decay schemes also introduce challenges, particularly due to coincidence summing effects as described in figure 2.12. Coincidence summing occurs when two or more gamma rays are emitted in a cascade (i.e. in quick succession) from the same nuclear decay. If these gamma rays are detected simultaneously within the resolving time of the detector, they are recorded as a single event with an energy equal to the sum of the individual gamma-ray energies. The coincidence phenomenon arises from the simultaneous detection or -x; these effects are independent of the frequency of the counting source and depend only on two parameters [82]:

• detection efficiency: this is linked to the probability that a photon emitted by the source interacts with the detector crystal. It depends on the solid angle of detection and the photon's energy.

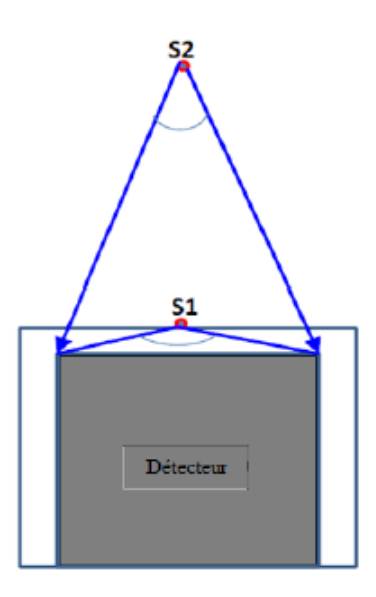


Figure 2.13: Effect of solid angle on the coincidence effects of sum peaks

• the desintegration shema: the complexity of the various de-excitation pathways plays a major role in the summation effect due to coincidences, which is all the more pronounced the higher the emission probability of the ray under consideration.

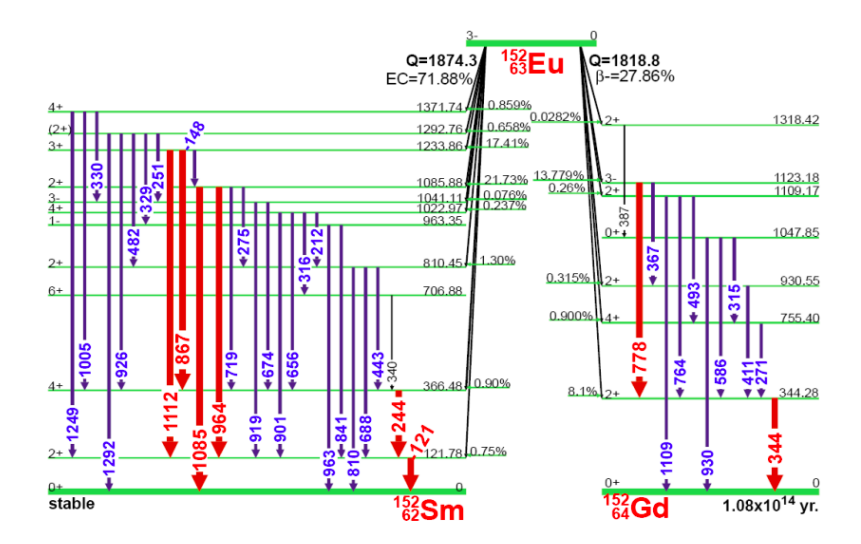


Figure 2.14: decay scheme of Eu-152

Corrections for coincident peak sums can be avoided by counting the sample away from the detector, so that the probability of two gamma rays reaching the detector at the same time becomes negligible [6]. This is quite impractical for low-activity samples such as environmental samples, where samples must be counted as close to the detector as possible. Another way of avoiding coincidence summing corrections is to use a standard containing the same radionuclide as that found in the sample to be analyzed. This may be practical for a routine laboratory where a few radionuclides are checked using a set of standards corresponding to those nuclides. But in cases where a variety of samples are to be analyzed, such as environmental samples, fission products, neutron activation samples, etc., it is virtually impossible to have standards which have the same radionuclides as the sample to be analyzed; in such cases it is preferable to apply sum peak coincidence corrections [83].

2.4.8 Methodology for True Coincidence Summing Correction

To account for these effects, corrections were applied using the MEFFTRAN (Marinelli Efficiency Transfer) software, which use efficiency transfer principles and detailed decay scheme data to account for summing effects. The software requires input data such as the detector efficiency curve, source geometry, and decay scheme information for the radionuclides of interest. In this study, the efficiency curve obtained from the experimental was used as input, and the source geometry was defined to match the experimental setup (a Marinelli beaker placed on the detector).

MEFFTRAN was then used to calculate correction factors for each gamma-ray energy of interest. The corrections were implemented by precisely defining the characteristics of both the detector and the source in Excel-based sheets, ensuring that the efficiency values were properly corrected for the true coincidence summing (TCS) effects. This approach allowed us to obtain more accurate efficiency values by minimizing the influence of coincidence summing on the experimental results. The FEPE corrected for coincidence summing effects can be expressed as [84]:

$$\varepsilon_{\text{true}}(E) = \varepsilon_{\text{meas}}(E) \times C_{\text{sum}}(E)$$
 (2.7)

where:

- $\varepsilon_{\text{meas}}(E)$ is the measured full-energy peak efficiency without summing correction,
- $C_{\text{sum}}(E)$ is the coincidence summing correction factor, which accounts for the probability of summation losses.

$$C_{\text{sum}}(E) = \frac{1}{1 - \sum_{i} B_{i} \cdot \varepsilon_{i}}$$
 (2.8)

where:

- B_i is the branching ratio of the i^{th} coincident gamma-ray,
- ε_i is the detection efficiency for the corresponding gamma energy.

The coincidence summing correction factor $C_{\text{sum}}(E)$ is derived from the summing probability, which depends on the branching ratios of the gamma transitions and the efficiency of the detector for each energy level [26]. Despite its effectiveness, the MEFFTRAN-based correction method has some limitations, such as uncertainties in the detector efficiency.

Table 2.3: True Coincidence Summing (TCS) Correction Factors for Different Gamma Energies

Energy (keV)	TCS Correction Factor
53	1.000
81	1.000
121	1.040
244	1.190
276	1.010
302	1.040
344	1.190
411	1.040
443	1.170
778	1.140
964	1.080
1085	0.970
1112	1.050
1408	1.060

2.4.9 Application of the Validated Model to Honey Samples

After validating the detector model and applying True Coincidence Summing (TCS) corrections, the finalized MCNP5 simulation was used to compute full energy peak efficiencies for honey samples placed in a Marinelli beaker geometry. To reflect the attenuation behavior of the samples, the elemental composition and density of various honey types were determined experimentally using the Wavelength Dispersive X-ray Fluorescence (WD-XRF) technique and implemented in the MCNP5 material cards. The honey matrix was modeled as a homogeneous mixture primarily composed of glucose $(80\%)C_6H_{12}O_6$ (17%) water 3%of trace components (K, Ca, Mg, etc.) corresponding to an approximate elemental composition of 42% carbon, 6,5% hydrogen, and 49,5% oxygen, and 2% minerals. With three representative densities considered: $1.25g/cm^3$, $1.35 \ g/cm^3$, and $1.45 \ g/cm^3$. For each density, simulations were conducted with uniformly distributed radionuclides, and the corresponding efficiencies were used to calculate the activity concentrations . Figure 2.15 illustrating the variation of detection efficiency with density, confirming the impact of matrix density on detector response.

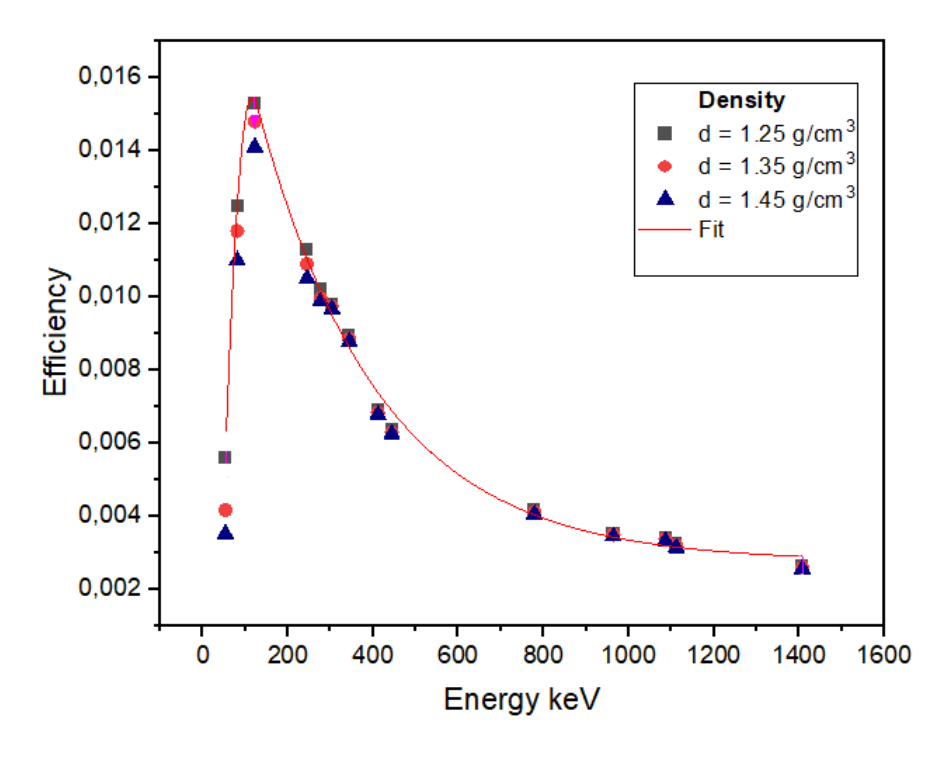


Figure 2.15: Simulated efficiency curves for different honey densities

2.4.10 Determination of Self-Absorption Correction Factors using the Developed Model

Among the corrections applied in gamma spectrometry for large-volume or dense samples, the correction of photon attenuation within the sample matrix—referred to as self-attenuation or self-absorption correction is particularly important Once the MCNP calibration efficiency is validated by the experimental measurement for honey samples, it is able to use the simulated efficiencies for determining the self-absorption correction factors CSA. To accurately account for the attenuation of gamma photons within the honey matrix, self-absorption correction factors were calculated using Monte Carlo simulations. The methodology involved simulating the detector efficiency for the honey sample with different densities and comparing it to a reference scenario in which the sample matrix was replaced by air which representing negligible attenuation. The CSA factor was defined as the ratio of the detector efficiency in a reference medium (typically air, representing negligible attenuation) to that in the actual sample [85]:

$$C_{\rm SA} = \frac{\varepsilon_{\rm air}}{\varepsilon_{\rm honey}} \tag{2.9}$$

where:

- ε_{air} is the full-energy peak efficiency (FEPE) of the detector when the matrix is replaced by air,
- $\varepsilon_{\text{honey}}$ is the FEPE with the actual honey composition and density.

Using air as the reference medium ensures that the correction factor reflects the true attenuation behavior of honey without introducing additional absorption effects, as would occur if a material such as water was used [86]. This approach enables precise quantification of activity concentrations by compensating for matrix-specific photon losses, particularly significant at low gamma-ray energies.

Simulation results presented in figure 2.16 showed that self-absorption effects were more significant at low gamma energies due to increased photon interaction with dense matrices, the FEPE for low-energy emissions such as 53 keV was reduced by up to 60%, with attenuation strongly dependent on both sample density and photon energy. At higher gamma energies(>300keV), the attenuation effects are less pronounced, as photons are more likely to escape the sample matrix and be detected. Indeed, at low gamma energies, the ability to pass through the sample material in which it contains heavy elements with higher densities and be detected by a detector is difficult due to the many interactions with material atoms, which lead to the loss of energy before reaching the detector. However,

at higher gamma energies the FEPE is reduced by only 2-3%, owing to the latter having a larger chance of escaping from the sample and attaining the detector

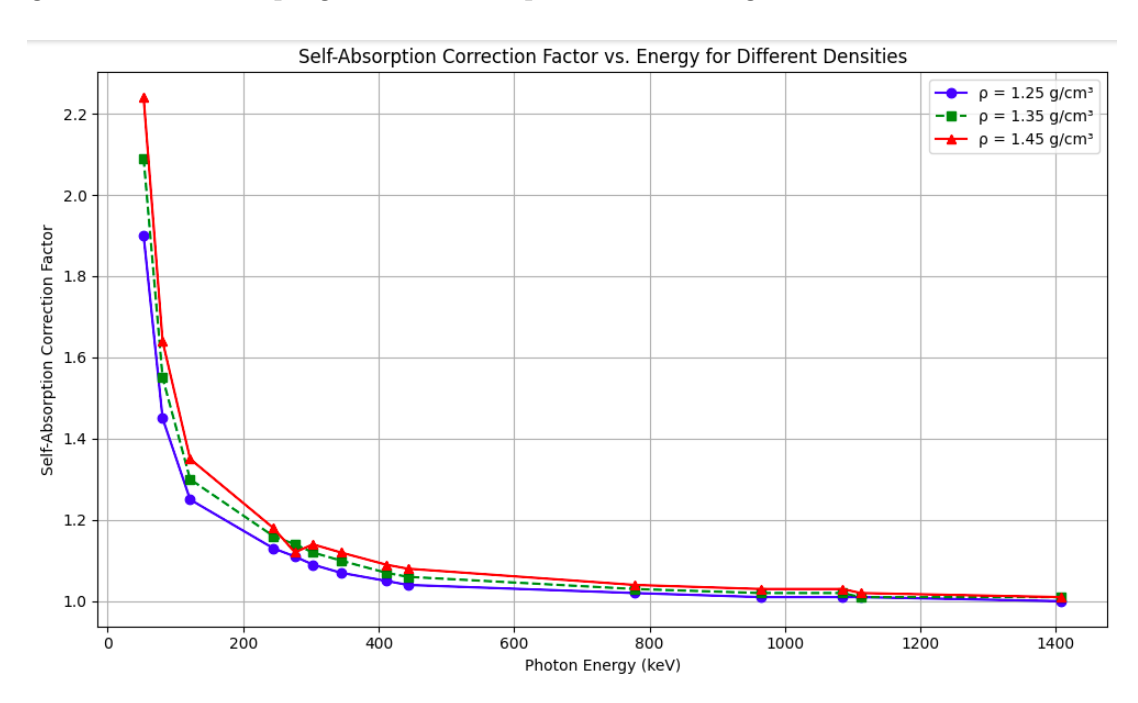


Figure 2.16: Variation of the self - absorption correction factor on the sample density (g/cm3)

2.4.11 Impact of Cross-Section Library Selection on Simulated Efficiency

Two cross-section libraries were used to carry out simulations with the MCNP5 code: ENDF/B-VI (Evaluated Nuclear Data File) and JENDL-5 (the first Japanese Evaluated Nuclear Data Library). These libraries were generated as ACE (A Compact ENDF) files using the NJOY16.65.j5 code. The ACE format is specifically designed for use in Monte Carlo simulations, providing a compact and efficient method for processing cross-section data. This format allows for accurate modeling of particle interactions based on evaluated nuclear data. A comparison of the two libraries was performed to assess whether changing the library would affect the simulated efficiency results. This study underscores the influence of cross-section data on detector response, highlighting how different libraries can impact efficiency predictions, especially at low energies where photon interactions with detector material are complex. The selection of an appropriate library based on the energy range of interest is essential for ensuring accurate simulations and reliable experimental results [75].

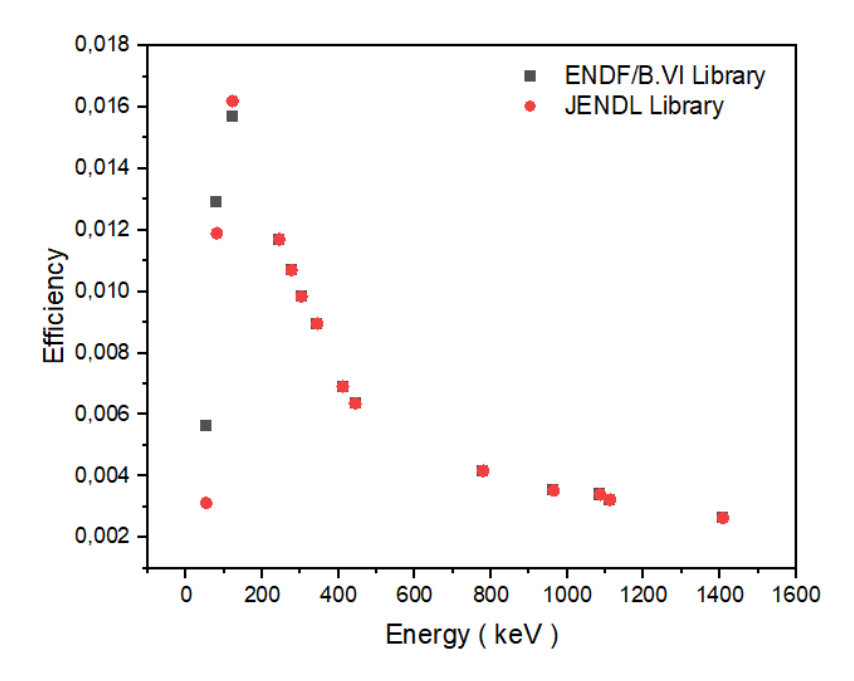


Figure 2.17: Efficiency calibration curves for the two libraries ENDF/B.VI and JENDL-5

The comparative analysis in Figure 2.17 illustrates the FEPE values derived from MCNP5 simulations using two distinct nuclear data libraries—ENDF/B-VI and JENDL-5—. Notable discrepancies were observed at lower energies (below 200 keV), where the ENDF/B-VI library generally provides higher efficiency values compared to the JENDL-5 library. This difference can be attributed to variations in how the two libraries evaluate the photoelectric cross-section in germanium, which is the dominant interaction mechanism at these energies. At higher energies, however, the efficiency values obtained from both libraries converge, with differences of less than 2%. This convergence suggests that ENDF/B-VI and JENDL-5 are similarly effective in modeling detector response in the higher energy range.

2.5 ANGLE Calculations

To conduct calculations using ANGLE software, several key parameters must be defined. The process begins by establishing a reference calibration curve derived from experimentally determined efficiency values. The detector's geometric properties are then configured within the "Detector" module, where the measurement geometry is defined as a Marinelli beaker with customizable dimensions, including radii and sample height. Sample matrices are characterized in the "Material" module, where their chemical composition and density are specified [87]. The efficiency transfer computation is executed in the "Transfer" module, where the reference calibration curve is applied, and the calculation is initiated

by selecting the "Calculations from Current Data" option. ANGLE employs the concept of the effective solid angle (Ω) to compute the Full Energy Peak Efficiency (FEPE) or absolute efficiency [75].

The solid angle Ω is given by:

$$\Omega = \int_{V_s, S_D} dd\Omega$$

where S_D is the surface of the detector exposed to the gamma photons and V_s is the volume of the source.

The absolute efficiency of the sample ϵ_{abs} is related to that of the reference standard $\epsilon_{abs,ref}$ by the expression [88]:

$$\epsilon_{\rm abs} = \epsilon_{\rm abs,ref} \frac{\Omega}{\Omega_{\rm ref}}$$

2.6 Simulation Results and Discussion

2.6.1 Validation of the optimized detector model

The results obtained for the source ¹⁵²Eu are presented in Figure 2.18. The figure demonstrate that the simulation using the MCNP5 code, based on the optimized detector model, shows excellent agreement with the experimental data. In contrast, the spectral simulation based on the detector dimensions provided by the manufacturer exhibits a significant discrepancy compared to the experimental spectra, particularly in the counts of the total absorption peaks and the shape of the Compton plateau. This comparison confirms that the detector model adjusted in this study is indeed optimized. Furthermore, the simulation using the MCNP5 code accurately accounts for all parameters involved in the calculation, including not only the physical interactions with the various materials constituting the detector but also electronic fluctuations such as electronic noise, variations in the electric field, charge collection, and the sampling function performed by the MCA (multi-channel analyzer) module.

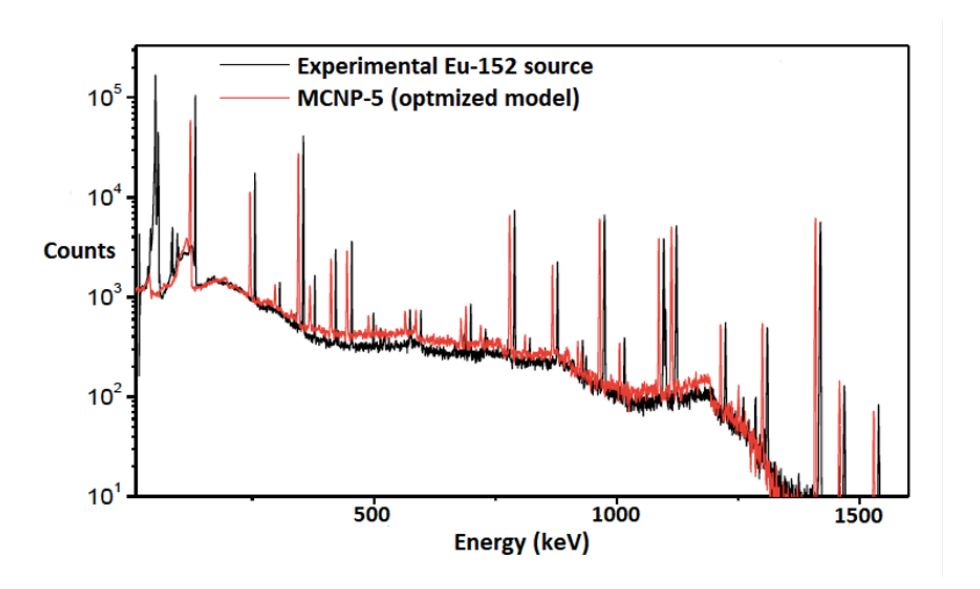


Figure 2.18: ¹⁵²Eu Spectrum: Experimental vs. MCNP Simulation (Optimized Model)

The validation of the optimized detector model was performed by comparing the FEPE curves obtained from experimental measurements, MCNP5 simulations and ANGLE software calculations. This multi-method approach ensures the robustness and accuracy of the model for gamma spectrometry applications.

2.6.2 Experimental vs. MCNP5 Simulated Efficiency

The experimental efficiency curve was derived from measurements using two Marinelli sources ¹³³Ba and ¹⁵²Eu, which provides a wide range of gamma-ray energies for validation. The MCNP5-simulated efficiency curve was generated using the optimized detector model, which accounts for the detector's geometric details, material properties, and electronic effects. The MCNP5-simulated efficiency curve exhibits excellent agreement with the experimental data across the entire energy range (from 53 keV to 1408 keV). This agreement validates the accuracy of the optimized detector model in reproducing the detector's response under real-world conditions.

2.6.2.1 Experimental Vs Simulation calculations

The comparative analysis presented in Figure 2.20. shows the FEPE obtained from experimental measurements, MCNP5 simulations, and ANGLE software calculations. At lower energies, particularly at 53 keV, notable discrepancies arise between the experimental and simulated efficiency values. The efficiency values derived from the ENDF/B-VI library closely match the experimental measurements, showing consistent agreement within a

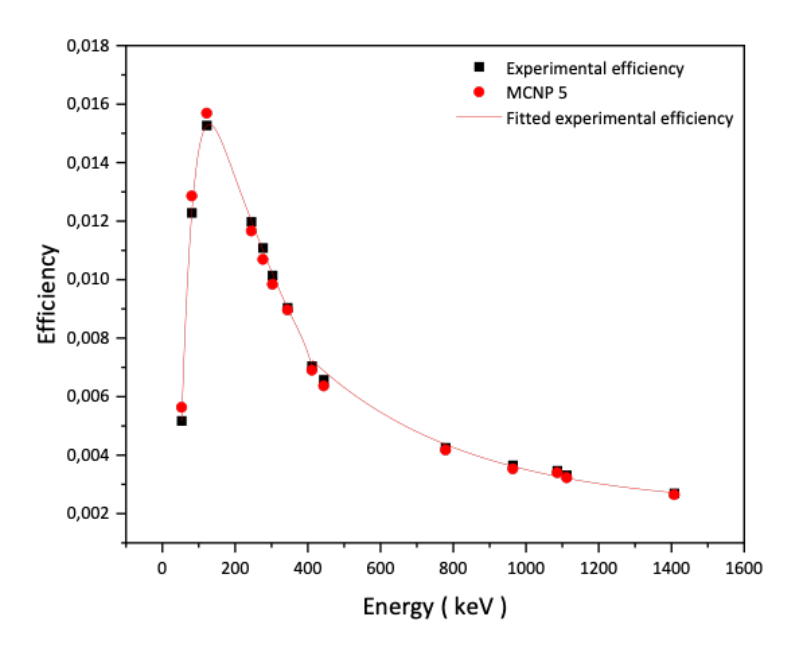


Figure 2.19: Comparison between experimental and MCNP-5 efficiencies

narrow margin of error (less than 3%). In contrast, the JENDL-5 library and the semi-empirical method (ANGLE) demonstrated larger deviations of approximately 50% and 70%, respectively.

These deviations suggest differences in how each method models low-energy photon interactions, likely due to variations in cross-section data or differing assumptions in the modeling approaches. The ANGLE software, which estimates efficiency based on effective solid angle adjustments, consistently predicts lower efficiencies at low energies. This underestimation is potentially due to differences in its treatment of photon attenuation and scattering within the matrix of the Marinelli beaker.

As the energy increases (above approximately 121 keV), the efficiency values from all methods converge closely with the experimental data, with error margins below 2%. This close agreement at higher energies indicates that, for applications involving mid-to-high energy gamma rays, both cross-section libraries and ANGLE provide reliable efficiency estimations.

However, at low energies, experimental calibration remains essential to ensure accuracy. These findings highlight the strengths and limitations of each method, offering valuable insight into their performance across different energy ranges. The effectiveness of each approach depends on the specific energy interval under investigation, enabling more informed decisions regarding the most suitable simulation method for a given application.

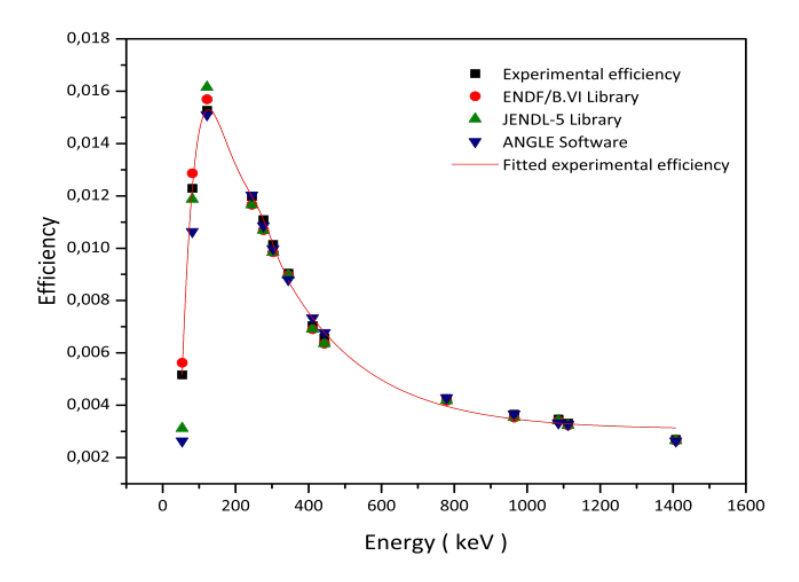


Figure 2.20: Efficiency calibration curves for both experimental and simulation calculation.

Chapter 3

Experimental Methodology

3.1 Introduction

This chapter describes the experimental procedures used to assess the contamination of honey samples by radioactivity, heavy metals, and antimicrobial residues. The study employs a combination of gamma spectrometry, atomic absorption spectroscopy (AAS), and the CHARM technique to quantify the presence of contaminants. The methodologies for sample collection, preparation, measurement, data analysis, and uncertainty evaluation are outlined to ensure the reliability and reproducibility of results. The experimental approach is designed to:

- Collect and prepare honey samples from different environmental settings (industrial zones, mountainous regions).
- Measure the activity concentrations of radionuclides using high-purity germanium (HPGe) detectors.
- Determine heavy metal concentrations using atomic absorption spectroscopy (AAS).
- Detect antimicrobial residues using the CHARM technique.
- Apply appropriate calibration, quality control, and statistical methods to validate the results.

3.2 Sample Collection and preparation

3.2.1 Sampling Strategy

A set of nine Honey samples (500 g each), were collected during the spring and summer of 2022 from various apiaries located in the northeastern region of Algeria. The colonies

of honeybees were kept from winter to summer in the same apiary. Table 1 shows the botanical origins of the honey samples studied. The sampling process was carefully designed to encompass a diverse range of environmental conditions, particularly focusing on locations with significant industrial activities that could contribute to contamination. A total of nine distinct areas were selected based on their proximity to industrial zones, mining operations, and other potential sources of environmental pollutants. The chosen sampling sites included:

- Tebessa: Samples were collected from three different locations within this region—one near a valley, another in the vicinity of a phosphate ore, and the third from a non-industrial area, providing a contrast to the other sampling locations, where industrial activities, traffic, and natural resources like quarries and mines may contribute to higher levels of environmental contamination.
- Setif: Sampling was conducted near a quarry and a iron ore site, both known for their potential emissions of heavy metals and radionuclides.
- Djelfa: Honey was collected from an area near a research center to evaluate potential contamination from scientific and agricultural activities.
- Guelma, Blida, and Biskra: These samples were obtained from industrial regions, where various manufacturing processes and traffic could contribute to environmental contamination.



Figure 3.1: Honey samples collection

The selection of these locations was guided by the objective of assessing the influence of industrial activities on honey contamination levels, particularly concerning radioactivity, heavy metals, and antimicrobial residues. The geographical distribution of the sampling sites is illustrated in Figure 3.2.

Table 3.1: Botanical origins of honey samples from North-eastern regions of Algeria

Sample ID	Type Of Honey	Plants	Collection Season/Year
H001	Multifloral	Wildflower, Lavender	Spring 2022
H002	Unifloral	Rosemary1	Spring 2022
H003	Multifloral	Prickly pear, Thyme	Spring 2022
H004	Multifloral	Orange Blossom, Citrus	Summer 2022
H005	Multifloral	Ziziphus spina Christi, Buckthorn plant	Summer 20222
H006	Unifloral	Ziziphus spina Christi, Rosemary	Summer 2022
H007	Multifloral	Wildflower, Eucalyptus	Spring 2022
H008	Multifloral	Artemisia	Summer 2022
H009	Multifloral	Rosemary, Artemisia	Summer 2022

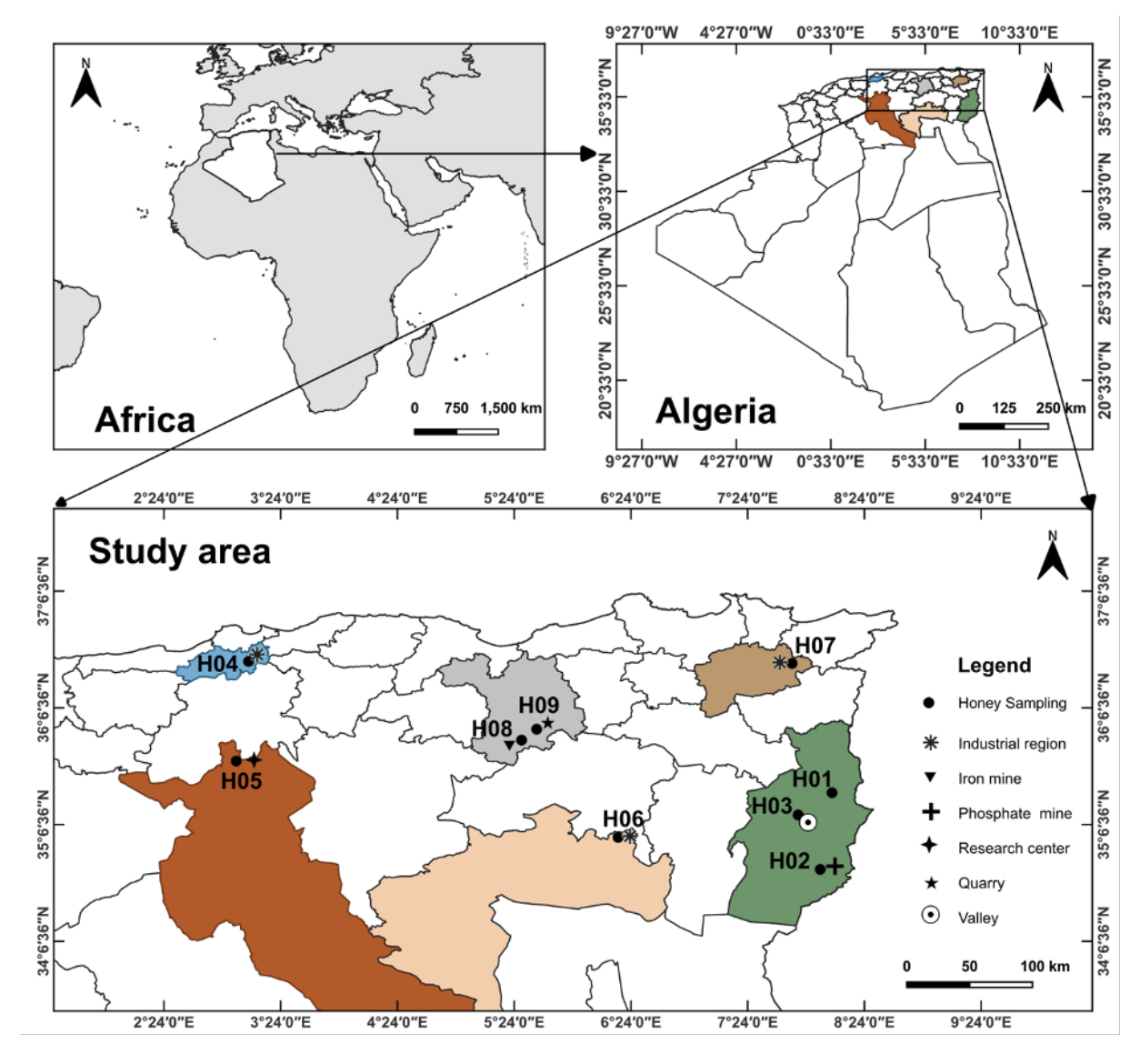


Figure 3.2: Map of sampling locations

3.3 Experimental setup

3.3.1 Radioactivity measurements

Preparing the sample for analysis

Measurements involving low levels of radioactivity, comparable to background levels, as in our study, require high detection efficiencies. This can be achieved either by using an expensive, large-volume germanium detector or by increasing the solid angle between the sample and the detector. We opted for the latter approach. For a maximum solid angle of around 4π , it is sufficient for the sample to almost completely encompass the detector. The Marinelli polyethylene beaker container ensures this 4π geometry. Before filling, the Marinelli beakers are cleaned with hydrochloric acid and rinsed several times with distilled water. Hermetically sealed samples must be stored for 30 days to allow 226 Rato reach secular equilibrium with its progeny. This duration is approximately seven times the radioactive half-life of 222 Rn

3.3.2 Gamma Spectrometry Analysis

• Acquisition chain

The measurements were performed by closed end coaxial, p-type HPGe detector. The characteristics of the p-type HPGe detector used in this analysis are described in detail in chapter II section 2. The detector is housed in a lead casing to minimize background radiation, (see Figure III-1). Each sample is then placed on the detector for 10000 s to ensure that the statistical uncertainty in the peak area will remain below 1%. The detector, immersed in a dewar, is cooled by liquid nitrogen to a temperature equal to 77 K (-196° C) to reduce thermal noise and improve its performance in detecting gamma rays. The background spectrum was acquired under the same experimental conditions by placing an empty Marinelli beaker in the measurement setup. This ensures that background radiation is measured in an environment identical to that of the actual samples, allowing for accurate background subtraction during data analysis. The collected spectrum was then analyzed using GammaVision software. Calculation of the activity concentrations of the various radioelements present in the samples was carried out both manually using a spreadsheet (Microsoft Excel), and with GammaVision software. After measurement and background subtraction, the activity concentrations were estimated.

• Energy Calibration

The first step in spectrum analysis is aligning the peaks of the calibration source, which emits gamma rays of well-known energies and intensities, with their corresponding channels. To ensure accurate calibration across the entire energy range of interest, we selected a maximum of 8192 channels with a conversion slope of 0.5 keV/channel. As detailed in Chapter II, the energy calibration was performed using a multi-gamma source of Eu-152 (table ??). The GammaVision software includes a built-in function that automatically generates the calibration curve.

• Efficiency Calibration

In gamma spectrometry, determining the detector efficiency is crucial for accurately calculating the activity of radioelements in a sample. This requires an energy-calibrated spectrum from standard radioactive sources over a sufficiently long period to ensure well-defined peaks with minimal uncertainty. To minimize errors in activity calculations, the standard sources should have a matrix density and geometry similar to those of the analyzed samples, reducing the need for self-absorption corrections. In our laboratory, we use two calibration sources: 152 Eu and 133 Ba. covering an energy range from 53 keV to 1408 keV, while 133 Ba offers additional calibration points at lower energies. Both sources consist of a resin with a density close to that of honey $(1.15 \ g/cm^3)$ and are contained in 450 cm³ Marinelli beakers. In this chapter, we opted to use the efficiency values calculated in chapter II.

• Calculation of minimum detectable MDA activity

the detection limit refers to the smallest amount of radioactivity that can be reliably measured above the background noise. The Minimum Detectable Activity (MDA) is a critical parameter, as it defines the lowest concentration of a radionuclide that can be detected with a given level of confidence. The MDA depends on several factors, including the counting time, the efficiency of the detector, the background radiation level, and the energy of the gamma ray being measured and (MDA's) are calculated using a coverage factor of 1.645, which corresponds to a 95% confidence level, using the formula [89]:

$$MDA = \frac{2.71 + 4.65\sqrt{B}}{P_{\gamma} \cdot \varepsilon \cdot T_c \cdot m}$$
(3.1)

where:

- B is the background count rate,
- P_{γ} is the photon emission probability,

- ε is the simulated efficiency of the detector,
- T_c is the counting time (in seconds),
- m is the sample mass (in kilograms),

The MDA for ²²⁶Ra, ²³²Th, ⁴⁰K and ¹³⁷Cs radionuclides in the present measurement system are calculated as 0.12, 0.21, 2.15 and 0.12 Bq kg-1, respectively. The activity concentrations of 9 samples for ¹³⁷Cs artificial radionuclide were either below the MDA or not detected.

• Qualitative and Quantitative Analysis

After acquisition, the obtained spectra (shown in figure 3.3 and 3.4) were analyzed for both qualitative and quantitative assessments of the honey samples. For qualitative analysis, GammaVision software, in combination with our custom-built library generated using the NUCLEIDES-NAVIGATOR III software (ORTEC), was used to identify the radionuclides present in the samples. The software automatically compared the measured spectra with the library, ensuring precise identification of the radionuclides based on their characteristic gamma-ray energies. For quantitative analysis, the activity concentrations of the different radioelements in the honey samples were calculated both manually using a spreadsheet (Microsoft Excel) and with GammaVision software. The software integrated the identified peaks and calculated the activity concentrations by measuring the areas under these peaks. Using calibration data, it then provided accurate estimates of the radionuclides activities in the samples.

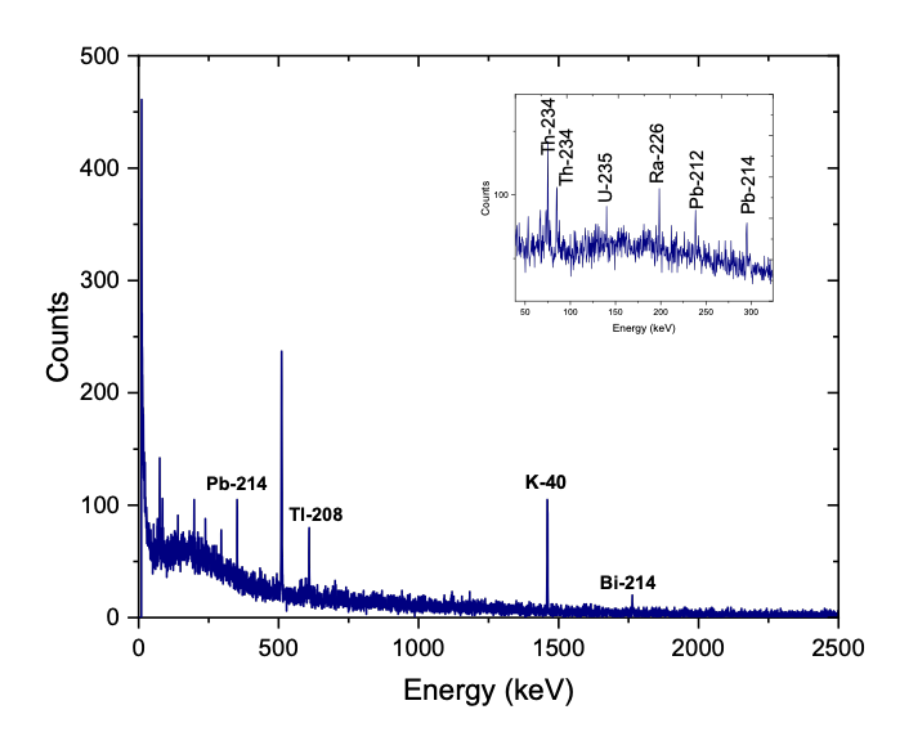


Figure 3.3: Spectrum of gamma radiation emitted by honey sample H008

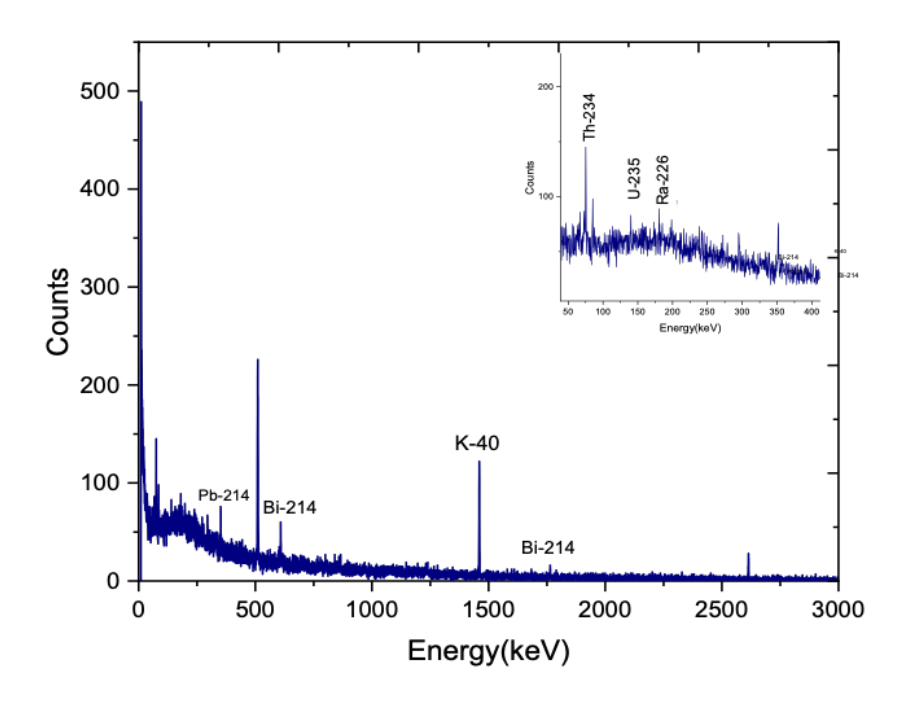


Figure 3.4: Spectrum of gamma radiations emitted by honey sample H001

The Concentrations measured using gamma ray energies emitted by ²¹⁴Pb (351 keV) and ²¹⁴Bi (609 and 1764 keV) were averaged to determine the activity concentration of ²²⁶Ra. The activity concentrations of ²³²Th were determined by averaging the concentrations measured from gamma ray energy emitted by ²¹²Pb (238 keV) and ²⁰⁸Tl (583 keV). Direct measurements of the activity concentration of ⁴⁰K and ¹³⁷Cs were determined from the 1460 keV and 661 keV gamma-ray energies, respectively. The activity concentration was calculated as follows [90]:

$$A\left(\mathrm{Bq/kg}\right) = \frac{N}{P_{\gamma} \cdot \varepsilon \cdot T_c \cdot m} \tag{3.2}$$

where:

• N is the net peak area (counts),

and its uncertainty was calculated as:

$$\Delta A = A \cdot \sqrt{\left(\frac{\Delta N}{N}\right)^2 + \left(\frac{\Delta \varepsilon}{\varepsilon}\right)^2 + \left(\frac{\Delta P_{\gamma}}{P_{\gamma}}\right)^2 + \left(\frac{\Delta m}{m}\right)^2 + \left(\frac{\Delta T_c}{T_c}\right)^2}$$
(3.3)

3.4 Heavy Metal Analysis

3.4.1 Instrumentation

The analysis of heavy metals was conducted using a PinAAcle 900H Atomic Absorption Spectrometer (AAS) manufactured by PerkinElmer. This high-performance instrument is equipped with both flame and graphite furnace systems, enabling the precise quantification of trace metals at low concentrations. The PinAAcle 900H offers exceptional sensitivity and accuracy, making it well-suited for the analysis of heavy metals in complex matrices. The operating conditions and emission wavelength lines used for each metal are detailed in Table III.1

Table 3.2: Operating parameters for elemental analysis using AAS.

Element	Al	$\mathbf{A}\mathbf{s}$	Cu	K	Zn
Fuel Flow (L/min)	2.5	2.5	2.5	2.5	2.5
Wavelength (nm)	309.27	193.70	324.75	766.49	213.86
Slit Width (nm)	0.7	0.7	0.7	0.7	0.7
Air Flow (L/min)	10	10	10	10	10

3.4.2 Sample Preparation

• The honey samples were prepared by digesting a 1g of each sample with 8 mL of 69% nitric acid (HNO_3) in Teflon vessels. • The sealed vessels were then placed in a Milestone microwave digestion system at 1000W and 200°C to break down the honey matrix and release the target metals into a liquid form. • the cooled digestion solution was then diluted to 50mL using high purity deionized water.



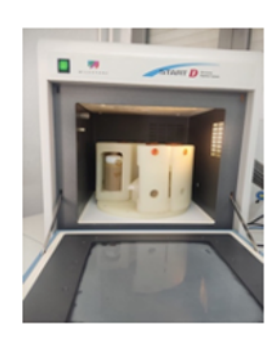






Figure 3.5: digestion process

3.4.3 Calibration

Calibration of process of AAS was performed using a series of standard solutions for each target metal: potassium (K), aluminum (Al), arsenic (As), copper (Cu), and zinc (Zn). The calibration process ensured accurate quantification of heavy metal concentrations in the samples by establishing a linear relationship between absorbance and concentration.

• Preparation of Calibration Standards

• High-purity certified standard solutions (1000 mg/L) for K, Zn, Cu, Al, and As were prepared from certified stock solutions. • A series of dilutions were made to cover the expected concentration range in the honey samples

• Instrument Calibration

• The AAS was calibrated using a blank solution (deionized water) followed by standard solutions at increasing concentrations as shown in the table III.2. • The absorbance values were recorded, and a calibration curve was generated by plotting absorbance against concentration.

Table 3.3: Calibration parameters for heavy metal analysis using AAS: concentration ranges and correlation coefficients (R^2) .

Metal	Concentration Range (mg/L)	Correlation Coefficient (R^2)
Potassium (K)	0.1 - 4	0.993
Aluminum (Al)	10-80	0.997
Arsenic (As)	10-80	0.989
Copper (Cu)	0.1 - 4	0.997
Zinc (Zn)	0.1 - 4	0.996

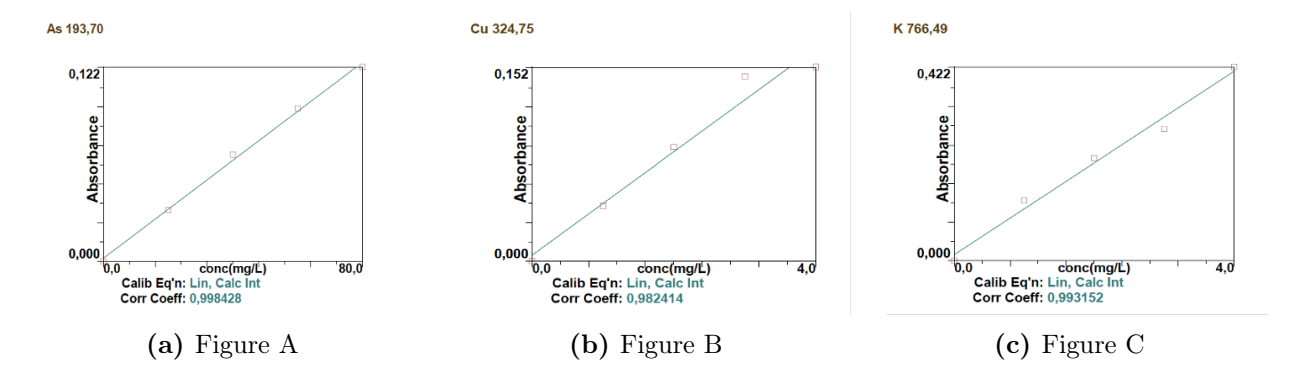


Figure 3.6: Calibration Curve for Quantification of Heavy Metals Using Atomic Absorption Spectroscopy (AAS)

3.5 Antibiotics residues

3.5.1 Charm II test

The Charm II technique is a competition test between an antibiotic labeled with tritium ([3H]-Tetracycline) or carbon 14 ([14C]-Penicillin G) and the substance to be analyzed to bind to a specific receptor [62]. In the case of a negative sample, all the sites of the receptor will be occupied by the labeled antibiotic and we obtain a high signal. In the presence of the substance sought, the sample is counted positive since there will be competition and the sites of the receptor will be occupied by the labeled antibiotic and the substance to be analyzed, hence a weak signal [58].



Figure 3.7: Charm II 7600 system equipment

3.5.2 Tetracycline Test for Honey

Antibiotics, including tetracycline drugs, are widely used in apiculture to treat bacterial brood diseases in beehives, such as American and European foulbrood. However, residues of these antibiotics, including tetracyclines, have been detected in honey samples worldwide. The CHARM II Tetracycline Test is a reliable method for detecting such residues. This test utilizes a binding reagent with specific receptor sites that selectively bind tetracycline drugs. During the assay, the binding reagent is added to a sample extract along with a known amount of [³H] labeled tetracycline (tracer). Tetracycline residues present in the sample compete with the tracer for binding to the receptor sites. The amount of tracer bound to the receptor sites is then measured and compared to a predetermined Control Point, which serves as the cutoff value to distinguish between negative and positive samples. A higher amount of bound tracer indicates a lower concentration of tetracycline in the sample, while a lower amount of bound tracer indicates a higher concentration of tetracycline.

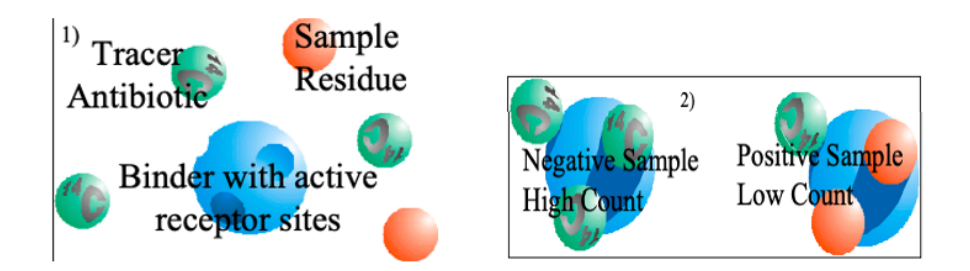


Figure 3.8: CHARM II test principle [91]

3.5.3 Sample Preparation

For the analysis of tetracycline residues in honey, 5.0 ± 0.1 g of honey was weighed into a labeled 50 mL centrifuge tube. If the honey contained sugar crystals, the sample was gently heated in warm water until it became homogeneous. Next, 20.0 mL of deionized or distilled water was added to the honey, and the mixture was thoroughly mixed until the honey was completely dissolved. The diluted sample was then inspected for insoluble debris, such as bee parts. If debris was present, the sample was centrifuged at 4000 rpm for 5 minutes, and the supernatant was used for further analysis. For dark honey samples (Pfund value > 83), a pretreatment step was performed by adding one Ion Exchange Resin tablet to 5.0 mL of the diluted honey extract. The mixture was vortexed for 10 seconds and centrifuged at 4000 rpm for 5 minutes. The resulting supernatant was transferred to a new tube and used as the 5.0 mL sample for the subsequent steps of the analysis.

3.5.4 Determination of the Control Point (CP)

The Control Point (CP) is a critical cutoff value used to distinguish between negative and positive samples for tetracycline residues in honey. It is calculated using data obtained from Negative Control samples. A new Control Point must be established for each new lot of tablet reagents to ensure accuracy and consistency. The procedure for determining the Control Point is as follows: 1. Run Negative Controls: Perform six replicate tests using Honey Negative Control samples in the assay. 2. Calculate the Negative Control Average: Determine the average value of the six replicates. If any of the six determinations deviate by more than 15% from the average, retest and replace that determination, then recalculate the average. 3. Calculate the Control Point: Subtract 25% from the recalculated average to establish the Control Point.

3.5.5 Interpretation of Results

The amount of tracer bound to the receptor sites is measured and compared to a predetermined Control Point (CP), which serves as the cutoff value for distinguishing between negative and positive samples. A sample is classified as negative (compliant) if the measured value is strictly higher than the Control Point. Conversely, a sample is classified as positive (non-compliant) if the measured value is less than or equal to the Control Point (Figure II.2). The interpretation is based on the principle that the amount of bound tracer is inversely proportional to the concentration of tetracycline residues in the sample. Specifically, a higher amount of bound tracer indicates a lower concentration of residues, while a lower amount of bound tracer indicates a higher concentration of

residues [92].

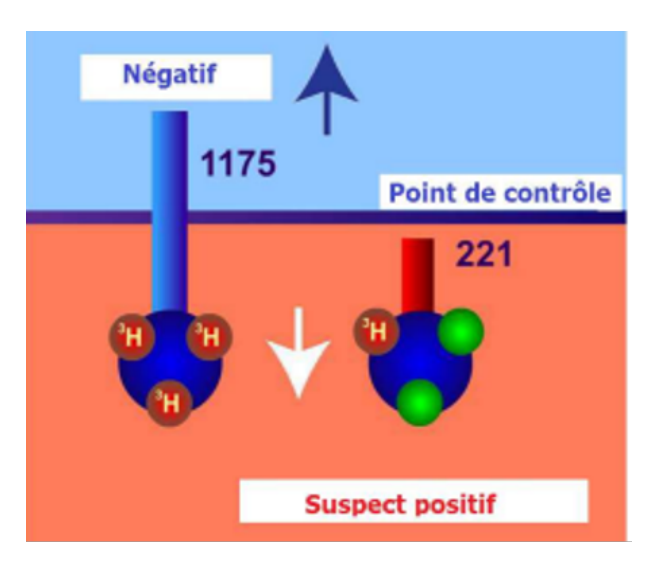


Figure 3.9: Example of interpretation of Charm II test results

Chapter 4

Results And Discussions

4.1 Introduction

Through the integration of simulation and experimental methodologies, this chapter aims to provide a comprehensive evaluation of the contamination levels in honey samples. Collects the results obtained from Monte Carlo simulations and experimental measurements. The first part focuses on the Monte Carlo simulation results, where the performance of the HPGe detector is evaluated through the FEPE calibration using the MCNP5 code and the ANGLE software. This chapter presents the experimental analysis of honey contamination. It includes measurements of radionuclide activity concentrations, heavy metal content, and antibiotic residues. Data are further analyzed to determine spatial distribution patterns, radiological and toxicological risk indexes, and multivariate correlations to better understand the origin and behavior of contaminants. These findings are discussed in light of international food safety standards and potential public health implications.

4.2 Experimental Analysis of Radioactive Contamination

4.2.1 Activity Concentrations

The concentration of radioactive isotopes in honey serves as an important bioindicator of environmental contamination. Honey is particularly valuable for this purpose due to its ability to accumulate trace elements and radionuclides from the environment. After acquisition, the obtained spectra were analyzed to perform both qualitative and quantitative assessments of the honey samples. The detected radionuclides were found to be naturally occurring, belonging to the radioactive decay chains of uranium-238 (²³⁸U) and thorium-

Table 4.1: Comparison of the radioactivity levels in honey samples with those from other regions worldwide

Activity Concentration (Bq/kg)							
Sample ID	226 Ra	²³² Th	$^{40}\mathrm{K}$				
H1	0.88 ± 0.12	0.59 ± 0.11	24 ±2				
H2	1.02 ± 0.11	0.71 ± 0.13	23 ± 2				
H3	1.17 ± 0.222	0.77 ± 0.12	47 ± 3				
H4	1.38 ± 0.21	0.80 ± 0.13	28 ± 2				
H5	1.67 ± 0.4	1.80 ± 0.26	62 ± 3				
H6	1.25 ± 0.14	1.38 ± 0.22	37 ± 2				
H7	1.07 ± 0.09	1.29 ± 0.19	34 ± 2				
H8	2.1 ± 0.39	1.53 ± 0.24	43 ± 3				
H9	$2.41 {\pm} 0.4$	1.04 ± 0.17	26 ± 2				
Mean	1,438	1.101	36				
SD	0.520	0.418	12.9				
World value [93]	33	45	420				

232 (²³²Th). Additionally, the primordial radionuclide potassium-40 (⁴⁰K) was identified. Anthropogenic radionuclides such as ¹³⁷Cs, originating from nuclear activities, were also measured due to their environmental and health significance. The activity concentrations of ²²⁶Ra were determined by averaging the measurements from gamma-ray energies emitted by its decay products, ²¹⁴Pb (351 keV) and ²¹⁴Bi (609 keV and 1764 keV). Similarly, the activity concentrations of ²³²Th were calculated by averaging the measurements from gamma-ray energies emitted by its decay products, ²¹²Pb(238 keV) and ²⁰⁸Tl(583 keV). For ⁴⁰K and ¹³⁷Cs, the activity concentrations were directly measured using their characteristic gamma-ray energies of 1460 keV and 661 keV, respectively. The activity concentrations, expressed in becquerels per kilogram (Bq/kg), were calculated using the relationship described in Chapter 3, with uncertainties reported at a 95% confidence level. The measured activity concentrations were found to be within the typical range observed in natural environments, suggesting no significant anthropogenic contamination in the sampled honey. These results align with findings from similar studies in uncontaminated regions, further supporting the use of honey as a reliable bioindicator for environmental monitoring. The activity concentrations of radionuclides in various honey samples labeled H001 to H009 which vary from one sample to another, summarized in 4.1.

4.2.2 Spatial Distribution

Quantum Geographic Information System (QGIS), a free GIS program [94] were employed to illustrate the spatial distribution of radioactive content in the honey samples using geospatial data analysis.

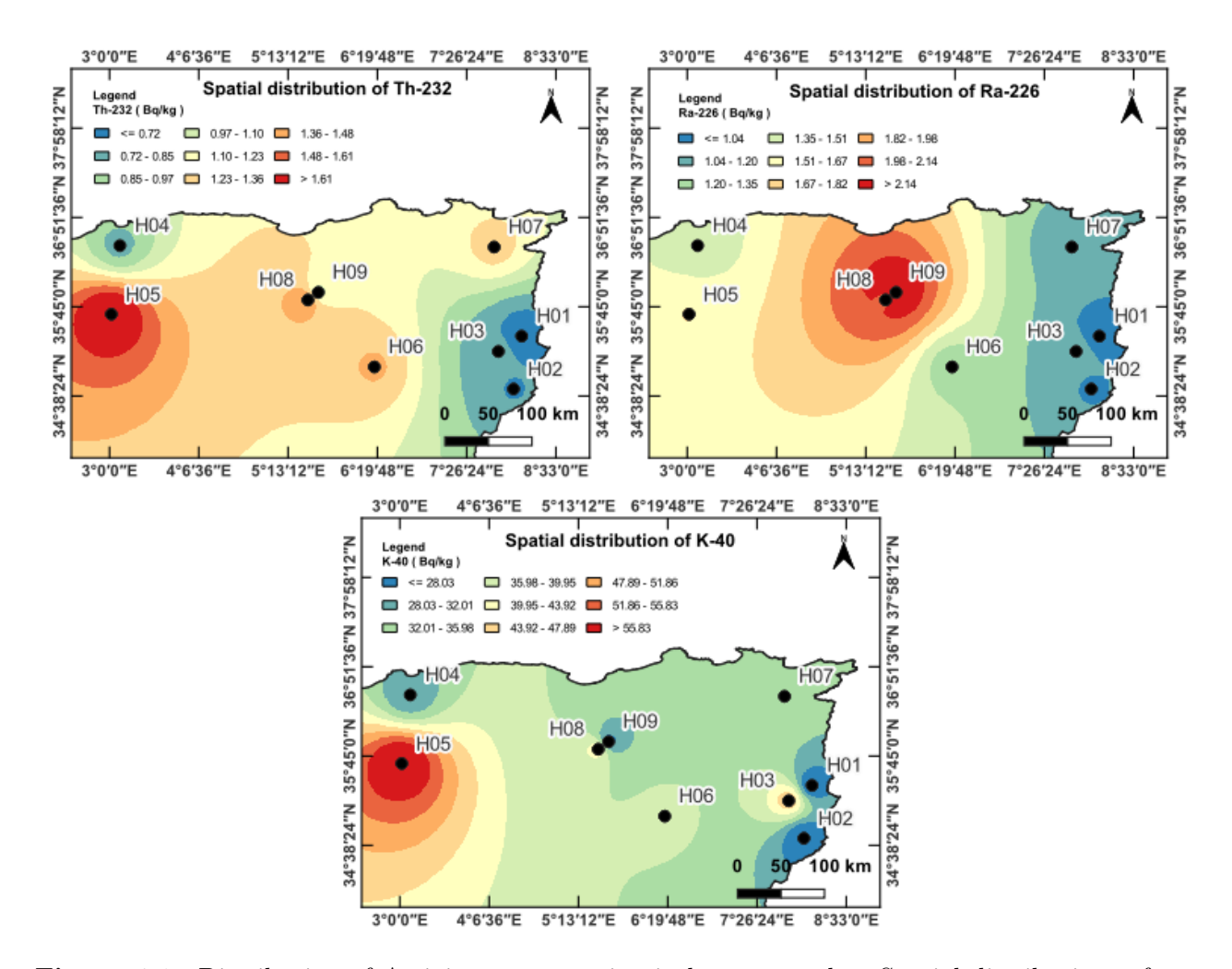


Figure 4.1: Distribution of Activity concentration in honey samples: Spatial distributions of 232 Th, 226 Ra and 40 K.

The geospatial distributions of radioaelements ²²⁶Ra, ²³²Th and ⁴⁰K were obtained by mean their activities using the inverse distance weighting (IDW) approach. The spatial distribution maps of the studied elements are presented in Figure 4.1. It reveals that ²³²Th and ⁴⁰K have the highest levels in the honey collected from the western part of the study area. The maximum concentrations of ²²⁶Ra are attained in the northeastern parts.

4.2.3 Radiological Risk Assessment

The radiological hazard indices are standard radiation hazard parameters used to assess the effects of radiation exposure on human and public health. By considering the radiation hazard associated with radionuclides (²²⁶Ra, ²³²Th, and ⁴⁰K), these indices are helpful in assessing the possible radiological influence of honey samples containing these radionuclides by a single parameter.

Daily Intake (D_{int})

The daily intake of radioactivity is considered by the accumulation of radioactivity in the human body through food consumption includes both the artificial radionuclide (¹³⁷Cs) and naturally occurring radionuclides such as ²²⁶Ra, ²³²Th and ⁴⁰K, is calculated using the following equation [95]:

$$D_{int} = \frac{A_i \times A_{ig}}{Nd} \tag{4.1}$$

Where, D_{int} is the daily intake of radionuclides (Bq/day) by individuals, A_i is the activity concentration of radionuclides (Bq/kg), A_{ig} is the per capita annual consumption of honey(kg/year) and N_d represents the number of days in a year. In Algeria, the average honey consumption in 2015 was 0.2 kg per person [96].

Annual Effective Dose (AED)

The annual effective dose is the annual radiation dosage that different human organs absorb or get as a result of consuming the naturally occurring radionuclides found in honey. It is calculated using equation [97]:

$$AED(\mu Sv/y) = \sum_{i}^{\infty} A_i \times A_{ig} \times CCF$$
 (4.2)

Where CCF is the ingestion dose conversion factor for related radionuclides which is are 2.8, 2.3 and $0.062\mu Sv/Bq$ for 226 Ra, 232 Th and 40 K respectively [98,99].

Excess Life Time Cancer Risk (ELCR)

The Excess Life Time Cancer Risk (ELCR) due to the ingestion of honey was assessed in order to estimate the possible carcinogenic consequences of consuming these veggies over an extended period of time used the equation [100]:

$$ELCR = AED \times RF \times L \tag{4.3}$$

Where, RF represents for the fatal cancer risk factor per sievert, which is $0.05 \ Sv^{-1}$ according

to the ICRP [101]. and Lis the lifetime duration (the average life expectancy in Algeria is around 77,9 years [102].

Internal hazard index (H_{in})

Internal hazard index of the gamma-ray specific activity concentrations of ²²⁶Ra, ²³²Th and ⁴⁰Kis calculated by using equation (3) given by:

$$H_{in} = \frac{A_{Ra}}{185} + \frac{A_{Th}}{259} + \frac{A_K}{4810} \tag{4.4}$$

Representative level index (RLI)

The representative level index (RLI)could be used to evaluate the degree of radiation hazard associated with terrestrial radionuclides [103], and it can be calculated using the following formula:

$$RLI = \frac{A_{Ra}}{150} + \frac{A_{Th}}{100} + \frac{A_K}{1500} \tag{4.5}$$

The growth of destructive body cells and hence subsequent development of cancer may occur if the value of RLI exceeds the standard value of unity [103].

Annual gonadal dose equivalent (AGDE)

The genetic significance of the annual dosage equivalent that the population's reproductive organs (gonads) receive is measured by the annual gonadal dose equivalent (AGDE) [].

The following formula was used to determine the AGDE caused by the specific activity of 226 Ra, 232 Th and 40 K.

$$AGDE = 3.09A_{Ra} + 4.18A_{Th} + 0.314A_{K} \tag{4.6}$$

The calculated values of the daily ingestion and radiological hazard indices of radionuclides ²²⁶Ra, ²³²Th and ⁴⁰K are presented in Table 4.2. The highest daily intake of ²²⁶Ra was found in sample H9 (1.32 mBq/kg), while for ²³²Th the intake ranges from 0.32 (mBq/kg) in sample H1 to 1 (mBq/kg) in sample H5. The daily intake of ⁴⁰K ranges from 12.6(mBq/kg) in H2 to 34.2(mBq/kg) in H5, with H5 showing the highest levels across all radionuclides.

The annual equivalent dose (AED) in honey samples was reported between 1,061 and 2,532 $\mu Sv/y$ with a mean value of 1,758 $\mu Sv/y$ which is under the worldwide accepted value of 290 $\mu Sv/y$ [104]. Correspondingly, the lifetime cancer risk values calculated for the three radionuclides in the honey samples were found to vary from 4,135 \times 10⁻⁶ to

Table 4.2: The caculated values of daily intake and radiological health risks parameters of 226 Ra, 232 Th and 40 K.

Sample ID	Daily intake (mBq/day)			Radiological hazard indices				
	²²⁶ Ra	²³² Th	⁴⁰ K	$\frac{AED}{(\mu Sv/y)}$	$ELCR \times 10^{-6}$	H_{in}	RLI	$\begin{array}{c} AGDE \\ (\mu Sv/y) \end{array}$
H1	0.36	0.32	14.2	1,0618	4,135	0,012	0,027	12,721
H2	0.56	0.39	12.6	1,183	4,607	0,013	0,029	13,341
Н3	0.64	0.42	25.6	1,5922	6,201	0,019	0,046	21,591
H4	0.43	0.76	15.3	1,488	5,795	0,016	0,035	16,4
H5	0.9	1.0	34.2	2,532	9,862	0,0288	0,070	32,152
H6	0.69	0.75	20.3	1,7936	6,986	0,0197	0,046	21,248
H7	0.59	0.71	18.9	1,6142	$6,\!287$	0,017	0,042	19,374
H8	1.15	0.84	23.4	2,413	9,398	0,026	0,057	26,386
H9	1.32	0.58	14.5	2,15	8,375	0,022	0,043	19,958
Mean	0.737	0.641	19.888	1,758	6,850	0,019	0.044	20.352
SD	0.323	0.228	6.950	0.514	2.004	0,005	0,013	6.145
World value [104]	-	-	-	290	10^{-3}	1	1	300

 $9,862 \times 10^{-6}$, which are significantly lower than the acceptable cancer risk threshold 10^{-3} for radiological risk [104,105], demonstrating that there is a comparatively low radiological health risk associated with the consumption of honey samples in this study is relatively low. The internal hazard index H_{in} and he representative level index (RLI), both vary from 0,012 to 0,0288 and from 0,027 to 0,070, respectively, hance, the radiation danger levels linked to consuming the examined honey samples are within safe limits, as indicated by the fact that all of these values are less than unity. Finally, as can be seen, the obtained value of AGDE for the studied samples ranges from 12,721 to 32,152 with an average of $20.352~\mu Sv/y$. Since the average value does not exceed the permissible recommended level by UNSCEAR [104] ($300\mu Sv/y$), the hazardous effects can be caused by the radiological exposure to gonads from consuming the analysed honey samples are negligible.

The 2000 report by UNSCEAR estimated that the annual global ingestion dose from natural sources generally varies from 0.2 to 0.8 mSv, with an average of approximately 0.31 mSv. This dose was reassessed in UNSCEAR's subsequent 2008 report, which found the ingestion dose generally ranged from 0.2 to 1.0 mSv, with an average annual ingestion dose of 0.29 mSv,which 0.17 mSv is due to 40 K. This dose results from the consumption of 550 kg of food per year, which corresponds to an activity of approximately 50 Bq/kg,and 0.12 mSv is due to long-lived radionuclides from the uranium and thorium series [106]. According to the WHO and the FAO in the CODEX ALIMENTARIUS COMMISION,the dose from ingestion of 40 K in food is not likely to be controlled because a healthy body

Table 4.3: Comparison of the radioactivity levels in honey samples with those from other regions worldwide

Activity Concentration (Bq/kg)							
Location	²²⁶ Ra	²³² Th	$^{40}\mathrm{K}$	$^{137}\mathrm{Cs}$	References		
Italy	=	-	61±12	< 0.16	[108]		
Poland	-	-	36 ± 21	1.3 ± 0.3	[109]		
Turkey	-	-	69 ± 4	18.2 ± 0.45	[110]		
Romania	4.16 ± 1.22	1.51 ± 0.74	24 ± 4	0.56 ± 0.34	[111]		
Iraq	27.18	33.18	1027.6		[112]		
Kosovo	$0.48 {\pm} 0.15$	1.28 ± 0.38	20.5 ± 0.5	1.03 ± 0.11	[113]		
Malaysia	3.96 ± 0.40	$1.46 {\pm} 0.23$	48 ± 4	_	[114]		
Republic of Serbia	$4.67{\pm}1.05$	1.32 ± 0.5	52 ± 3	< 0.5	[115]		
Slovakia	_	-	_	1.23 ± 0.04	[116]		
Greece	_	-	30 ± 6	0.5 ± 0.1	[117]		
Algeria	1.43 ± 0.23	1.10 ± 0.17	36±2	< DL	Present study		

needs potassium for its well-being and the potassium content (including ⁴⁰K) is kept constant by normal physiological regulatory processes [107].

4.2.4 Multivariate Statistical Analysis

Statistical analysis of this study was performed using origin pro software [118]. Pearson correlation analysis was performed to assess how strongly the variables under investigation are related. The principal component analysis (PCA) was employed to find the dependent variable principals and reduce the dimensionality of various datasets to present information with an emphasis on similarities and differences. In addition, hierarchical cluster analysis (HCA) was applied to classify the measured and calculated radiological parameters into groups based on their similarities.

The Pearson correlation analysis of honey samples

Table 4.4: Principal component	analysis of the	radionuclides	and radiologica	l health risk p	a-
rameters in honey samples					

	226 Ra	²³² Th	$^{40}\mathrm{K}$	AED	ELCR	Hin	RLI	AGDE
²²⁶ Ra	1							
$^{232}\mathrm{Th}$	0,469	1						
$^{40}\mathrm{K}$	0,207	0,733*	1					
AED	0,806**	0,868**	0,702*	1				
ELCR	0,806**	0,868**	0,702*	1	1			
Hin	0,736*	0,874**	0,79305*	0,99**	0,99**	1		
RLI	0,535	0,897**	0,917**	0,923**	0,923**	0,96527**	1	
AGDE	0,532	0,890**	0,921**	0,921**	0,921**	0,963**	0,999**	1

^{*}Correlation is significant at the 0.05 level (2-tailed test)

^{**}Correlation is significant at the 0.01 level (2-tailed test)

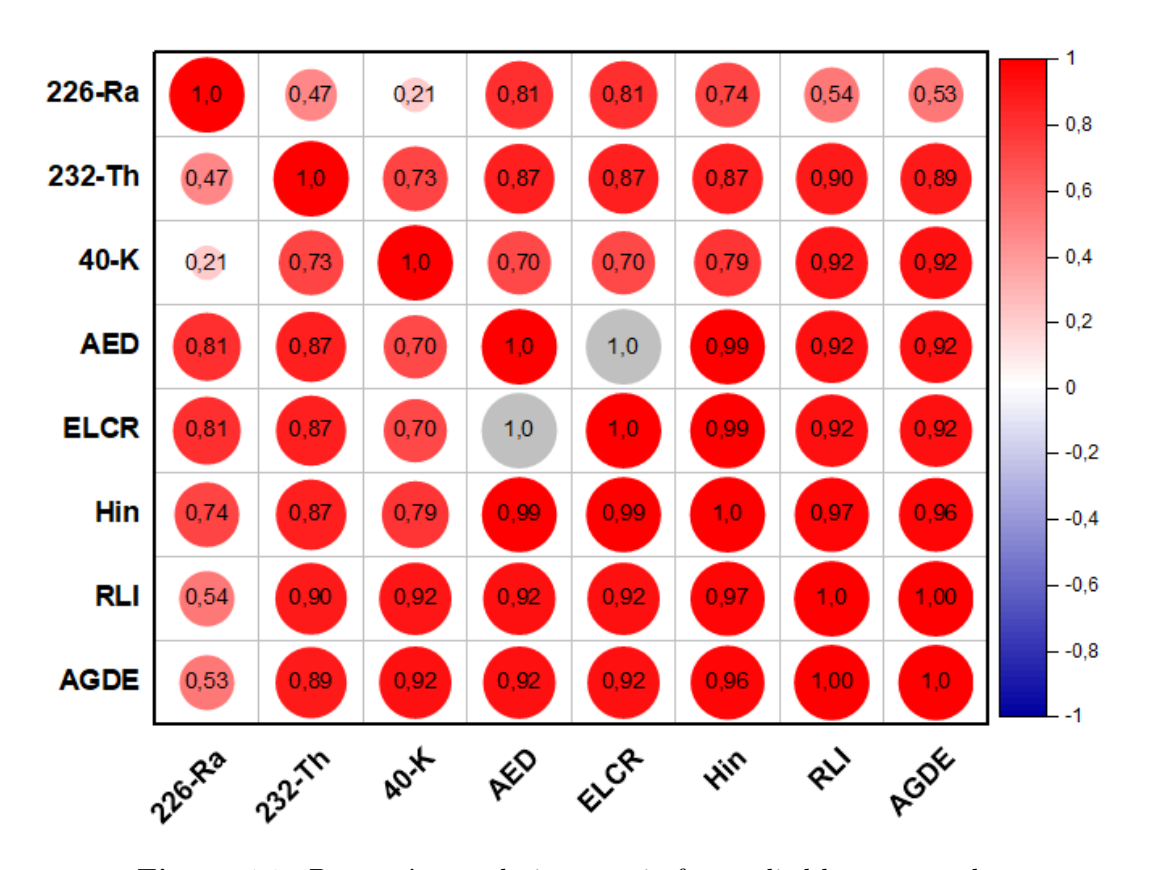


Figure 4.2: Pearson's correlation matrix for studied honey sapmles.

Table 4.4 and Figure 4.2 display the pearson's correlation coefficients between the concentrations of natural radionuclides (226 Ra, 232 Th, and 40 K) and various radiological health risk parameters.

A moderate degree of positive correlation (R = 0.46967) was noted between ^{226}Ra and ^{232}Th , indicating that these isotopes may to some extent co-occur in the honey samples

because they are present in natural decay chains. In contrast to the other radionuclides, 226 Ra demonstrated a weak correlation with 40 K (R=0.20757), supporting the distinction made between series and non-series radionuclides. On the other hand, 232 Th had a stronger positive correlation with 40 K (R=0.73342), suggesting that both radionuclides are likely controlled by similar geochemical or environmental conditions in the study region.

The radiological risk parameters (AED, ELCR, Hin, RLI, AGDE) exhibited consistently high correlations with all three radionuclides, reflecting their mathematical dependence on activity concentrations. 226 Ra, showed strong correlations with AED and ELCR (both R = 0.80672), while its correlation with Hin, RLI, and AGDE ranged from 0.53231 to 0.7362. In contrast, 232 Th demonstrated very strong correlations with all risk parameters, including RLI (R = 0.89785) and AGDE (R = 0.89078), emphasizing its dominant contribution to the overall radiological risk.

All the radiological hazard parameters showed very strong correlations with all three of the radionuclides as expected from their direct dependence upon radionuclide activity concentrations. 226 Ra correlated most strongly with AED and ELCR (both R = 0.80672), while all correlations with Hin, RLI, and AGDE were in the 0.53231 to 0.7362 range.

Principal Component Analysis (PCA)

The principal components analysis (PCA) is a multivariate statistical technique, Kaiser guidelines state that the primary component and descriptor of the variance must have an eigenvalue greater than 1.0 [119]. Table 4.5 presents the principal components loadings, eigenvalues, as well as their respective explained variance, while the rotated factor loadings are illustrated in Figure 4.3.

Only one component with eigenvalue exceeding 1 explain around 85% of the total variance and shows strong positive loadings with all variables, including $^{226}\mathrm{Ra},~^{232}\mathrm{Th},$ $^{40}\mathrm{K},$ AED, ELCR, Hin, RLI, and AGDE. This indicates that PC1 is heavily impacted by overall radiological risk markers and may be understood as a comprehensive radiological risk component. PC2 accounts for an additional 12.15% of the variance and is mostly impacted by $^{226}\mathrm{Ra}$'s high positive loading and $^{40}\mathrm{K}$'s negative loading which suggests possible differentiation between radionuclide sources or distribution behaviors. Thus, while PC1 rflects quantitatively the total radiological impact from all parameters , PC2 seems to factor out the effect of certain radionuclides.

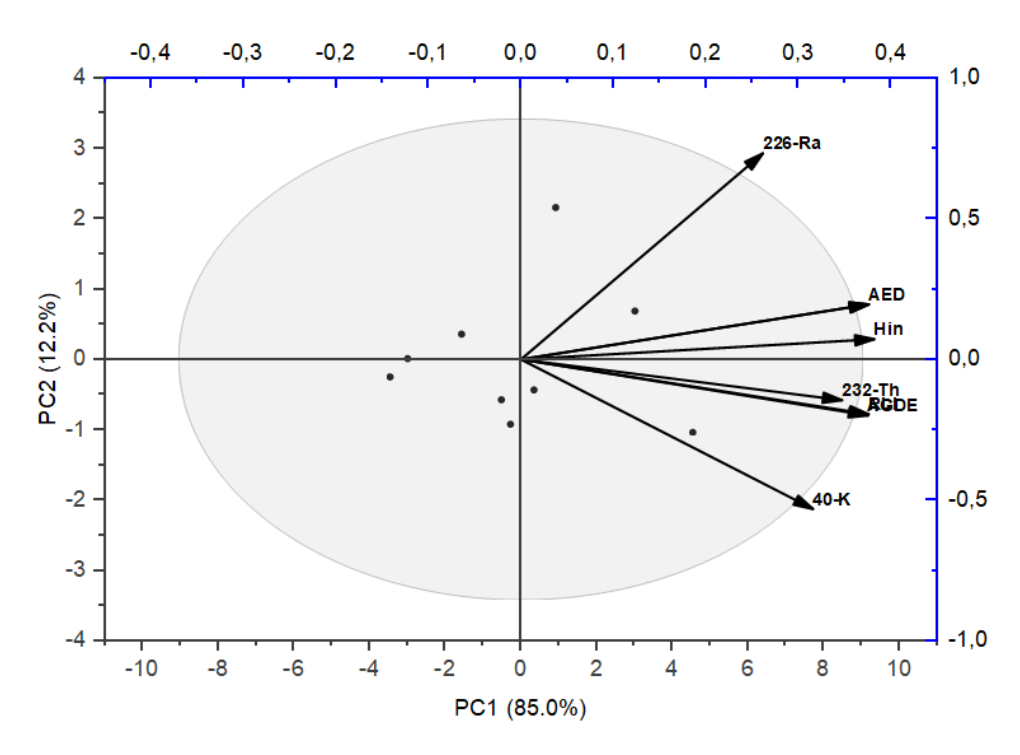


Figure 4.3: Principal component plot

Table 4.5: Principal component analysis of the radionuclides and radiological health risk parameters in honey samples

Variables	PC 1	PC 2
²²⁶ Ra	0,26169	0,73266
232 Th	0,34716	-0,14521
$^{40}\mathrm{K}$	0,31575	-0,53158
AED	$0,\!37621$	$0,\!19567$
ELCR	$0,\!37621$	$0,\!19567$
Hin	0,38213	0,07189
RLI	$0,\!37597$	-0,19492
AGDE	$0,\!37532$	-0,19952
Eigenvalue	6,8001	0,97214
Variance (%)	85,00126	$12,\!15174$
Cumulative (%)	85,00126	97,153

Hierarchical Cluster Analysis

Hierarchical Cluster Analysis (CA) is a multivariate technique designed to categorize system objects into clusters based on their similarities, aiming to achieve an optimal grouping where observations within each cluster are similar, while the clusters themselves are distinct from one another [120]. The CA data (hierarchical clustering) for the activities of the studied radionuclides and the radiological parameters is shown in Figure 4.4. All

the clusters are formed based on existing similarities. Two main clusters were identified from all of the parameters. The first cluster consists of only 226 Ra while the second consists of 232 Th and 40 K and all the other radiological variables. From cluster 1 and cluster 2 the total level of the radioactivity mainly depends on 232 Th and 40 K concentrations. The cluster analysis showed a strong association with both the PCA and Pearson correlation.

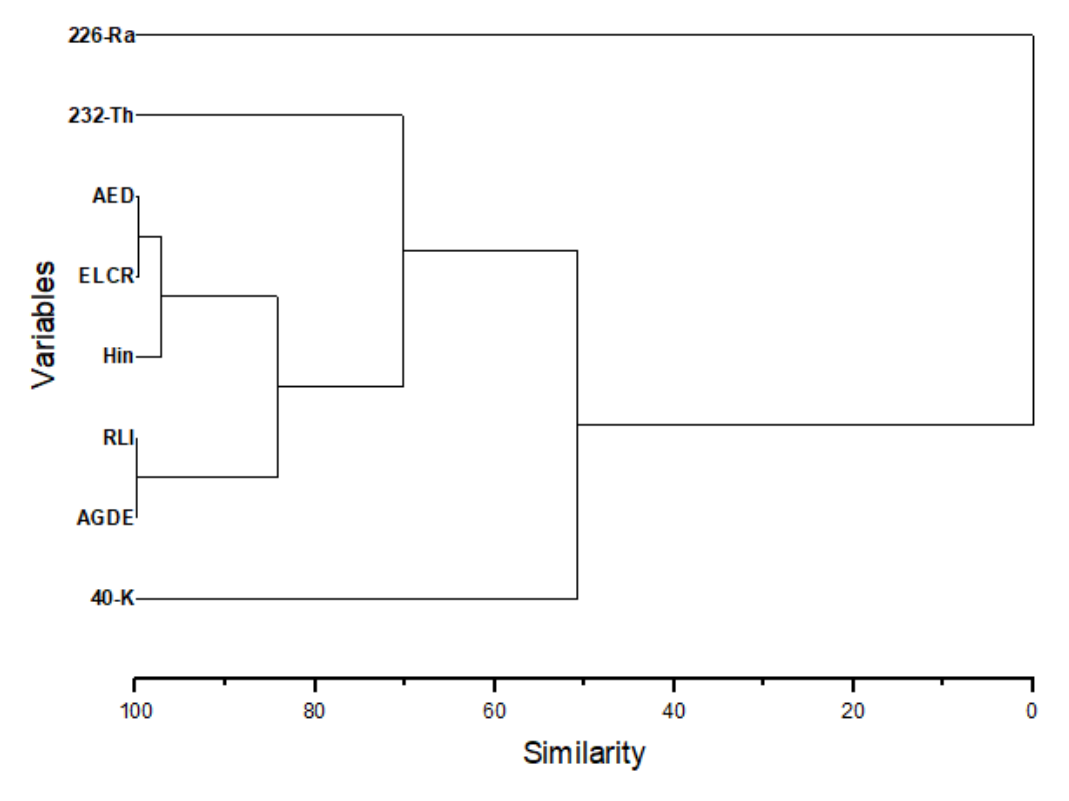


Figure 4.4: Clustering dendrogram of the honey samples' radiological parameters and radionuclides.

4.3 Experimental Analysis of Heavy Metals Contamination

4.3.1 Heavy Metals concentrations

Trace elements such as aluminum (Al), potassium (K), and zinc (Zn), as well as Heavy metals like copper (Cu) and arsenic (As) were analyzed in honey samples to assess their levels and potential health risks. While K, Cu, and Zn are essential nutrients required for biological processes, Al. is non-essential and can be toxic at high levels, where As is highly toxic even at low concentrations. These elements can enter honey through various pathways, including soil, water, and atmospheric deposition, making honey a valuable

bioindicator of environmental pollution. The concentrations of heavy metals and trace elements in the honey samples are summarazed in table ??

Table 4.6: Concentrations	(mg/L)) of heavy	metals in	honey.
-----------------------------------	--------	------------	-----------	--------

	Heavy metals concentration					
Sample ID	K	$\mathbf{Z}\mathbf{n}$	Cu	Al	As	
H1	725 ± 70	0.157 ± 0.017	$1.206\pm0,20$	6.89 ± 1.9	ND	
H2	732 ± 79	1.897 ± 0.31	0.569 ± 0.023	8.45 ± 2.78	ND	
H3	723 ± 57	0.147 ± 0.0091	2.132 ± 0.25	9.50 ± 3.34	0.009 ± 0.0001	
H4	684 ± 24	0.119 ± 0.016	2.018 ± 0.26	4.57 ± 1.4	0.022 ± 0.0013	
H5	713 ± 23	0.101 ± 0.012	2.885 ± 0.42	ND	0.006 ± 0.001	
Н6	749 ± 79	0.219 ± 0.019	2.127 ± 0.27	9.79 ± 3.9	0.012 ± 0.0012	
H7	751 ± 88	1.012 ± 0.20	3.339 ± 0.47	ND	0.005 ± 0.0006	
Н8	706 ± 47	0.108 ± 0.0019	1.563 ± 0.29	11.03 ± 4.4	0.001 ± 0.0004	
H9	719 ± 52	0.88 ± 0.018	2.694 ± 0.38	4.739 ± 1.3	0.003 ± 0.0005	
Mean	722,444	0,551	2.059	7.852	0,00828	
SD	20.821	0,626	0,860	2,527	0,007	
WHO safe limits (μ gg1)		5	3		$10500~\mu~\mathrm{g/kg}$	

4.3.2 Spatial Distribution

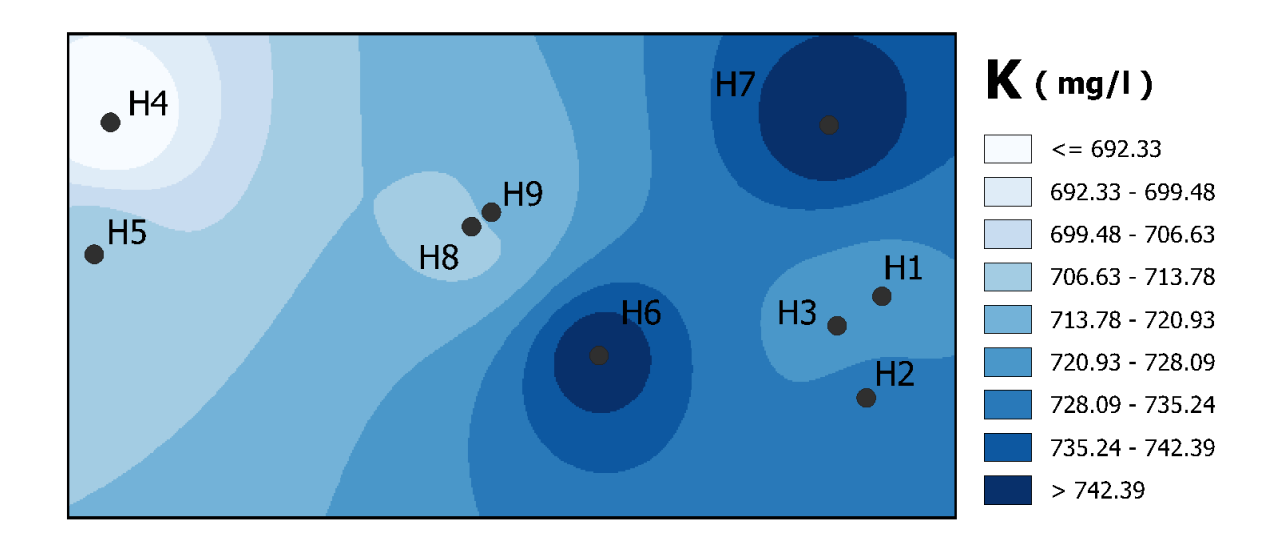


Figure 4.5: K distribution .

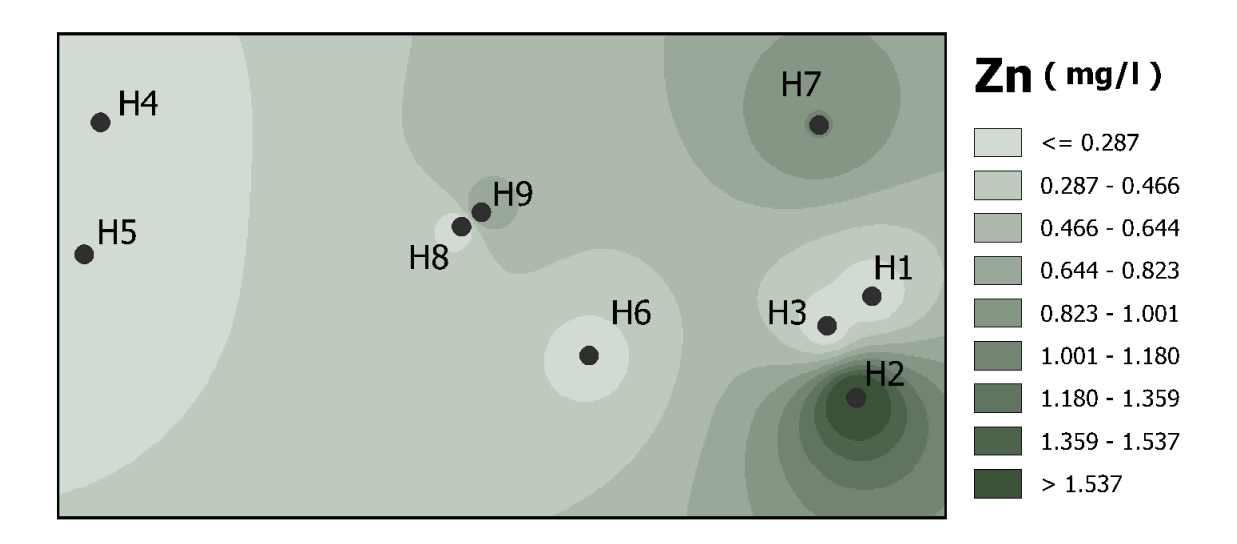


Figure 4.6: Zn distribution.

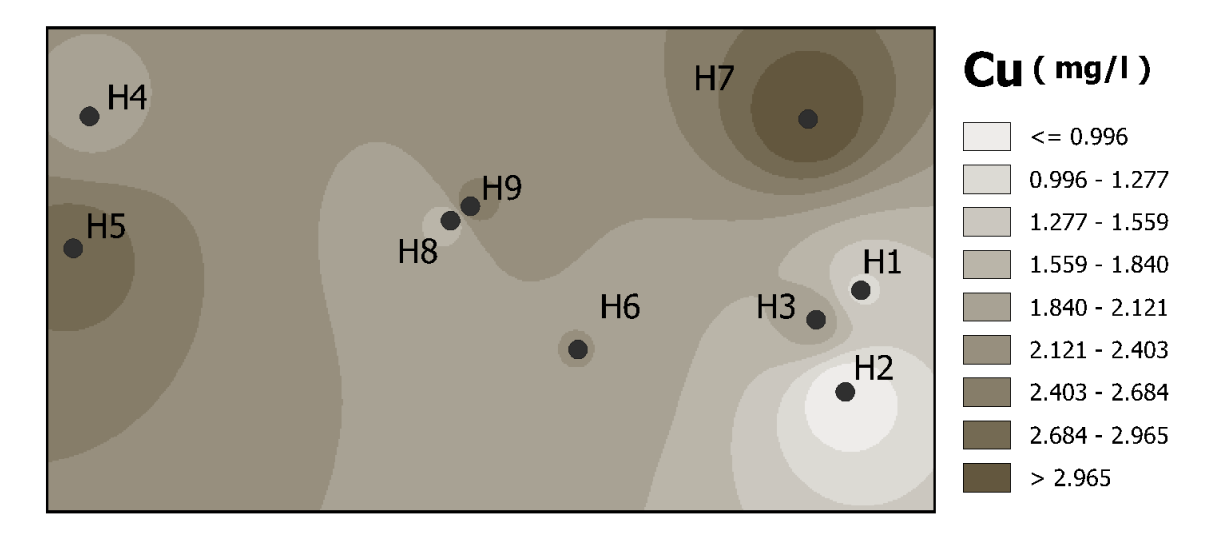


Figure 4.7: Cu distribution .

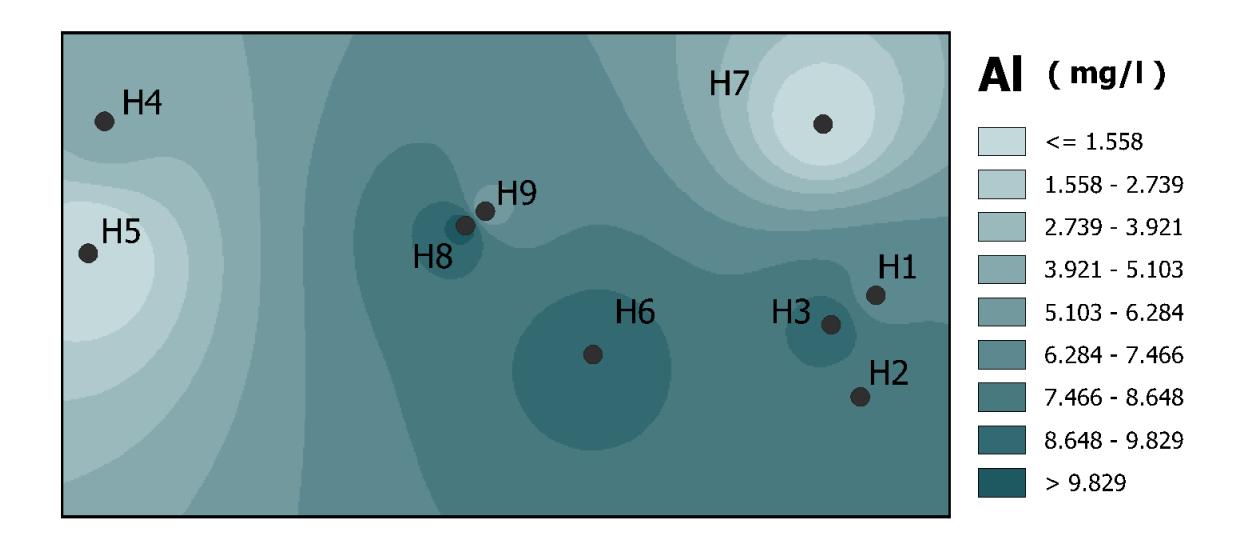


Figure 4.8: Al distribution .

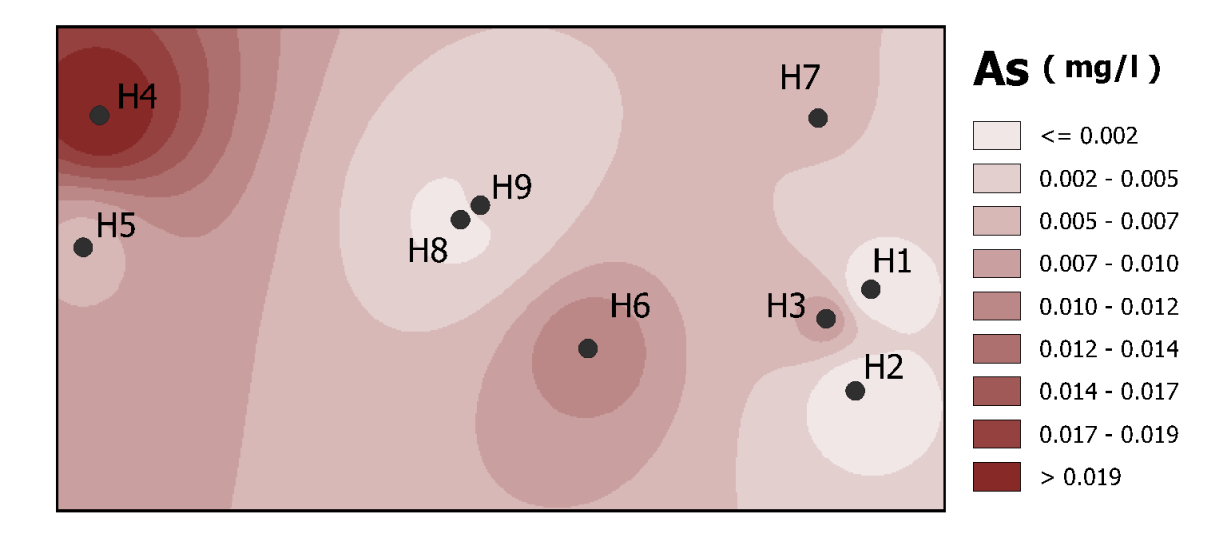


Figure 4.9: As distribution.

The spatial distribution of heavy metals concentrations (K, Zn, Cu, Al, and As) (presented in figures 4.5-4.9) in honey samples reveals distinct patterns linked to environmental and botanical factors. Potassium an essential element in plants (684–751 mg/L), was consistently the most abundant element, with relatively uniform distribution reflecting its natural presence in nectar. Higher concentrations of trace metals were observed in samples from industrial zones such as Blida (H007), Biskra (H008), and Guelma (H006), suggesting a clear influence of anthropogenic pollution. Unifloral rosemary honey (H002) showed elevated Zn and moderate Cu, while multifloral samples from Ziziphus and buckthorn plants (H005, H006) exhibited significant Cu content, highlighting the role of botanical

origin. Aluminum levels were highest in summer-collected samples from contaminated areas—especially in H008 (11.03 mg/L) and H006 (9.79 mg/L)—possibly due to increased dry-season deposition. Arsenic was not detected in honeys from relatively clean zones (H001, H002) but was present in trace amounts in samples from mining and industrial areas, with the highest values found in H004 and H003, near phosphate and iron ore sites. Overall, the spatial distribution pattern confirm that environmental exposure and floral sources both contribute to the variability in heavy metal content, with summer samples and those from polluted regions generally exhibiting higher concentrations.

4.3.3 Health Risk Assessments

To evaluate the potential health risks associated with heavy metal exposure through honey consumption, risk assessment indices such as the Daily Intake of Metals (DIM), Target Hazard Quotient (THQ), and Hazard Index (HI) were calculated. These indices help determine whether the detected metal concentrations pose a significant non-carcinogenic or carcinogenic risk to consumers. The assessment considers average honey consumption rates and established reference doses for each metal to provide a comprehensive understanding of potential health implications.

Daily Intake of Metals (DIM)

To determine the dose of human exposure, the average daily intake of was calculated by the following equation:

$$DIM(mg/kg/day) = \frac{C_{heavymetal} \times C_{honeyintake}}{B_{averageweight}}.$$
 (4.7)

where C_{metal} is the heavy metal concentration in honey (mg / L), $C_{honeyintake}$ is the average daily consumption of honey and it was estimated to be (50 g/day for both adults and infants [121]) and $B_{averageweight}$ is the average body weight, it was considered to be 70 kg for adults and 15 kg for children [122].

Target Hazard Quotient (THQ)

The Target Hazard Quotient (THQ) is a widely used parameter in health risk assessment to evaluate the non-carcinogenic risk of exposure to heavy metals. It compares the estimated exposure level of a heavy metal to its reference dose (RfD), which is the maximum daily exposure unlikely to cause adverse health effects over a lifetime. When the THQ is less than 1, the exposed population is considered to be at no serious risk. However, if it is greater than 1, it indicates that exposure may pose health hazards. The THQ is calculated using the following formula [123]:

$$THQ = \frac{DIM}{R_f D}. (4.8)$$

where, RfD refers to the oral reference dose proposed by the U.S. Environmental Protection Agency (US EPA) of each heavy metal. Oral RFDs for heavy metals were presented in Table 4.7.

Table 4.7: Reference oral dose (RfD) for metals

Metals	RfD (mg/kg/day)	Source
Zn	0.3	
Cu	0.04	
As	0.0003	[124]
Al	1.0	
K	NS	
	NICENTAL CONTRACTOR	

NS: Not Specified.

Hazard Index (HI)

The HI is also used to assess the cumulative risk of multiple metals present in a food product, calculated by summing the THQ values for each metal. The hazard index is key factor for evaluating the overall potential risks associated with exposure to many contaminants, it is the sum of HRIs of each heavy metals and is calculated as follows:

$$HI = THQ_{Cu} + THQ_{Al} + THQ_{Zn} + THQ_{As}$$

$$\tag{4.9}$$

When the HI is greater than 1, it indicates the concumed item that contains pollutants may have a significant negative impact on one's health.

Table 4.8: Daily Intake of Metals from honey consumption by adults and children

		Daily	Intake (mg	/kg/day)		
Sample ID		K	Zn	Cu	Al	As
H1	Adults	0,3836	8,30688E-5	6,38095E-4	0,00365	
	Infants	1,78994	3,87616E-4	0,00298	0,01701	_
H2	Adults	0,3873	0,001	3,01058E-4	0,00447	_
	Infants	1,80723	0,00468	0,0014	0,02086	_
НЗ	Adults	0,38254	7,77778E-5	0,00113	0,00503	4,7619E-6
	Infants	1,78501	3,62927E-4	0,00526	0,02345	2,222E-5
H4	Adults	0,3619	6,2963E-5	0,00107	0,00242	1,16402E-5
	Infants	1,68872	2,93798E-4	0,00498	0,01128	5,43156E-5
Н5	Adults	0,37725	5,34392E-5	0,00153	_	3,1746E-6
	Infants	1,76032	2,49358E-4	0,00712	_	1,48133E-5
Н6	Adults	0,3963	1,15873E-4	0,00113	0,00518	6,34921E-6
	Infant	1,8492	5,40687E-4	0,00525	0,02417	2,96267E-5
H7	Adults	0,39735	5,3545E-4	0,00177	_	2,6455E-6
	Infant	1,85414	0,0025	0,00824	_	1,23444E-5
Н8	Adults	0,37354	5,71429E-5	8,26984E-4	0,00584	5,29101E-7
	Infants	1,74304	2,6664E-4	0,00386	0,02723	2,46889E-6
H9	Adults	0,38042	4,65608E-4	0,00143	0,00251	1,5873E-6
	Infants	1,77513	0,00217	0,00665	0,0117	7,40667E-6

The data in Table 4.8 demonstrates that honey consumption contributes minimal amounts of metals to daily dietary intake for both adults and children. K shows the highest levels (0.36–0.40 mg/kg/day for adults; 1.69–1.85 mg/kg/day for infants) because it is naturally abundant in plant-derived foods such as honey, but these values remain well below the recommended daily intake. The 4.7 times higher exposure seen in infants simply reflects their smaller body weights rather than greater consumption, as toxicological assessments are weight-normalized. Trace metals like Zn, Cu, and Al appear at very low concentrations (10^{-5} to 10^{-3} mg/kg/day), with the highest aluminum level in infants (0.02417 mg/kg/day in H6) representing less than 1% of the safe weekly limit. Detectable As in some samples (up to 2.96×10^{-5} mg/kg/day) falls far below WHO safety thresholds (Table 4.7). While occasional outliers like elevated zinc in sample H2 suggest possible local environmental factors, the overall pattern confirms honey's safety. The entries for certain

metals indicate levels below detection limits, providing additional reassurance. The study ultimately confirms that typical honey consumption poses negligible metal-related health risks across all age groups.

Table 4.9: Target hazard quotient and harzard index of metals from honey consumption by adults and children

Target Hazard Quotient								
Sample ID		K	$\mathbf{Z}\mathbf{n}$	Cu	Al	$\mathbf{A}\mathbf{s}$	Hazard Index	
H1	Adults	_	2,76896E-4	0,01595	0,00365	_	0,019874779	
	Infants	_	0,00129	0,07444	0,01701	_	0,092739696	
H2	Adults	_	0,00335	0,00753	0,00447	_	0,015343033	
	Infants	_	0,01561	0,03512	0,02086	_	0,071593663	
НЗ	Adults	_	2,59259E-4	0,0282	0,00503	0,01587	0,049359787	
	Infants	-	0,00121	0,13159	0,02345	0,07407	0,230322644	
H4	Adults	_	2,09877E-4	0,02669	0,00242	0,0388	0,068121692	
	Infants	_	9,79326E-4	0,12456	0,01128	0,18105	0,317869444	
H5	Adults	_	1,78131E-4	0,03816	_	0,01058	0,048921516	
	Infants	_	8,31193E-4	0,17807	_	0,04938	0,228277581	
Н6	Adults	_	3,86243E-4	0,02813	0,00518	0,02116	0,054865078	
	Infants	_	0,0018	0,13128	0,02417	0,09876	0,256011433	
H7	Adults	_	0,00178	0,04417	_	0,00882	0,05476984	
	Infants	-	0,00833	0,20609	_	0,04115	0,255567033	
Н8	Adults	_	1,90476E-4	0,02067	0,00584	0,00176	0,028464726	
	Infants	_	8,888E-4	0,09647	0,02723	0,00823	0,132822107	
Н9	Adults	_	0,00155	0,03563	0,00251	0,00529	0,044985361	
	Infants	_	0,00724	0,16628	0,0117	0,02469	0,209910694	
Average	Adults		,	,	,	,	0,04274509	
O	Infants						0,199457144	

Table 4.9 presents the THQ for individual heavy metals (Zn, Cu, Al, and As) detected in honey samples (H1–H9), as well as the aggregated Hazard Index (HI), representing the cumulative non-carcinogenic health risk due to simultaneous exposure to these elements. The values are calculated separately for adults and infants, considering their respective consumption rates and body weights.

Across all samples, the THQ values remained below the safety threshold of 1, indi-

cating that the exposure to individual metals through honey ingestion does not pose a significant non-carcinogenic risk for either adults or children. However, a clear trend of elevated THQ values is observed in infants, with values approximately 3–5 times higher than those for adults. This is attributed to infants' lower body mass and relatively higher consumption ratio, making them more susceptible to bioaccumulated toxicants.

Copper (Cu) consistently exhibited the highest THQ values among all metals across most samples, particularly in samples H3, H4, H6, and H7, with infant THQ values reaching up to 0.206 (H7). This is of concern, given Cu's potential to induce oxidative stress and hepatic toxicity at elevated levels.

Arsenic (As) though often present in lower concentrations, demonstrated significant THQ contributions in samples H4, H6, and H9, with the highest value being 0.181 in infants (H4). This reflects a potential concern for chronic exposure, especially considering the high toxicity of inorganic arsenic compounds.

Aluminum (Al) a neurotoxic element, showed moderate THQ values in infants, particularly in H2 (0.02086) and H6 (0.02417), though well below the critical threshold.

Zinc (**Zn**) an essential trace element, generally displayed low THQ values across all samples and age categories, indicating low toxicity risk from honey ingestion.

When evaluating the Hazard Index (HI), the sum of all individual THQs for each sample, a clearer picture of cumulative risk emerges. The HI remained well below 1 in all adult cases, with the highest being 0.068 (H4). However, for infants, the HI values were significantly higher, peaking at 0.3179 (H4) and exceeding 0.25 in several samples (H6, H7, H9). These results suggest that while adult exposure to these contaminants via honey remains within safe limits, infants may face an elevated cumulative risk, particularly in samples from industrial zones where environmental contamination is likely.

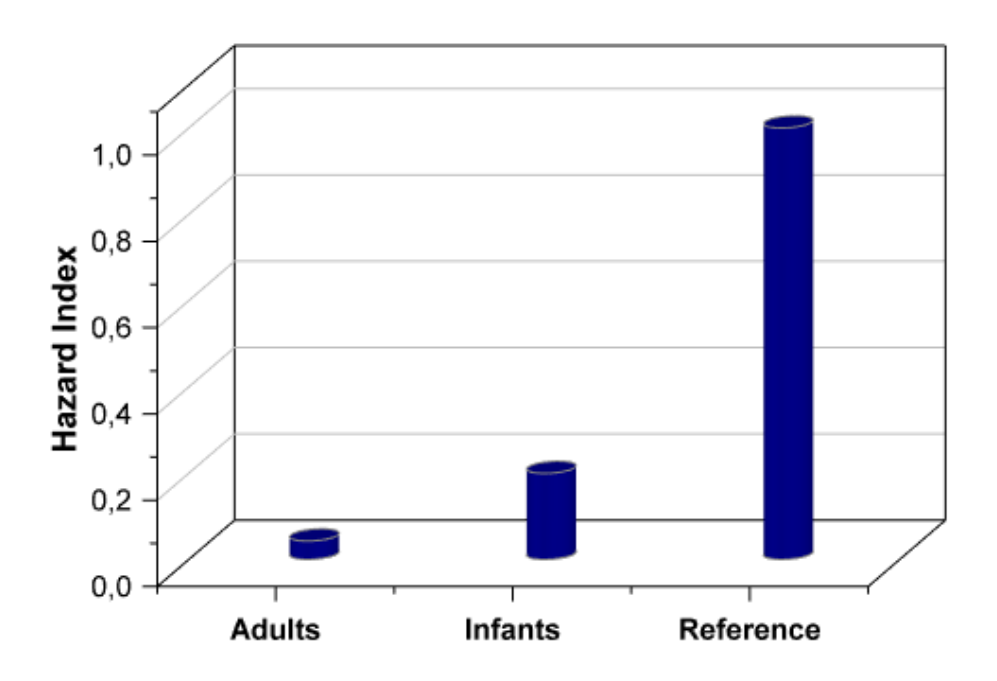


Figure 4.10: Hazard index

4.3.4 Multivariate statistical analysis

Pearson Correlation Analysis

Pearson correlation analysis can be used to evaluate the correlation between HM concentrations and successfully identify different sources by looking at the linear relationship between two different HMs. The degrees of linear correlation are described by the correlation coefficient value (r), with |r| > 0.3, it shows that there is a relationship between the two HMs, while |r| > 0.7 There is a significant correlations [125]. Figure ?? displays the Pearson correlation coefficients for each of these rates along with their significance levels (p < 0.05). In this study, the correlations are considered moderate (0.5 < r < 0.7), and weak (r < 0.5), respectively. The findings demonstrated that the high positive correlation between Zn and Cu suggests that these metals have a possible common source or similar behavior in the honey matrix. There was a nearly moderate positive correlation between Al and K, suggesting that they might originate from a variety of sources [126]. Weak correlations between Zn and K, K and Cu signific that these HMs may not be homologous [127]. As (same with Al except with K) has negative correlation with all metals which indicating that these metals may originate from different sources or undergo distinct biogeochemical processes.

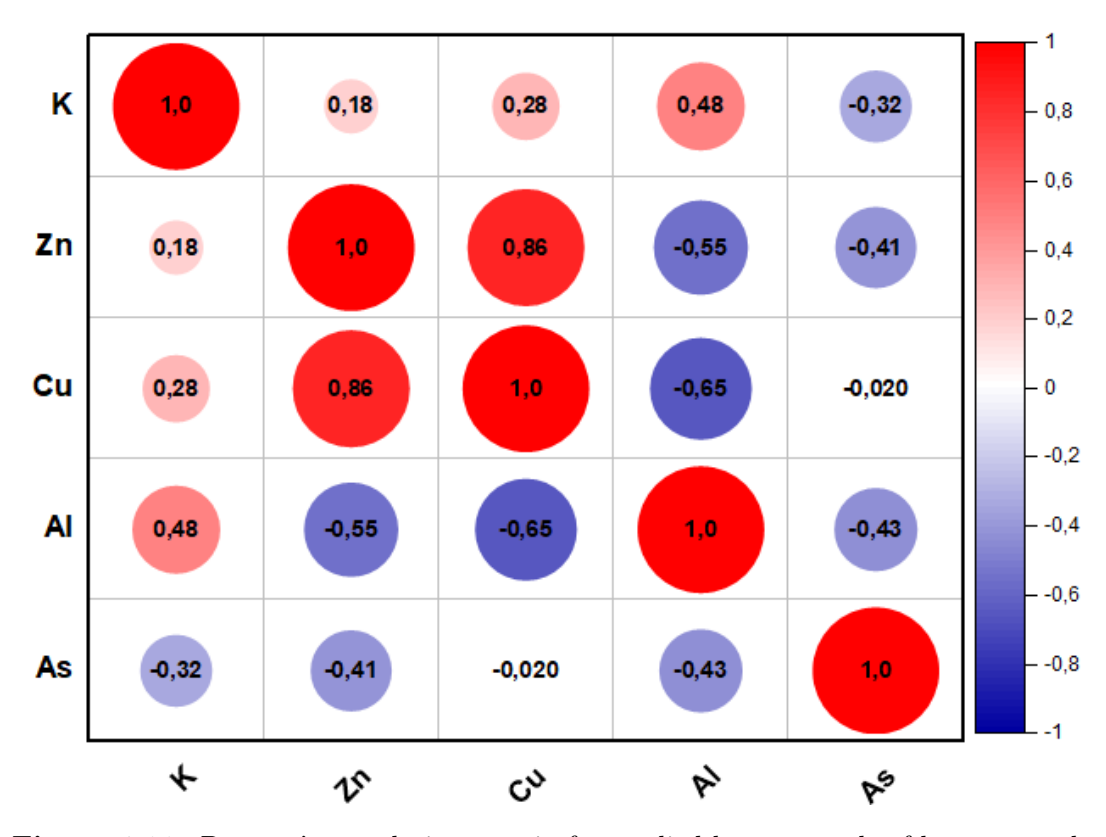


Figure 4.11: Pearson's correlation matrix for studied heavy metals of honey sapmles.

Principal Component Analysis (PCA)

The PCA has been used to identify pollutant sources and can effectively reduce the number of variables and there by facilitate analysis of the relationships among the observed variables [128]. Kaiser guidelines state that the primary component and descriptor of the variance must have an eigenvalue greater than 1.0 [119]. Thus, taking into account eigenvalues greater than one, two principal components were extracted, accounting for a cumulative variance of 83.73%. (Table 4.10). The first component (PC1) with a contribution of 47.68% made significant positive contributions to the loadings of Zn (0.60104) and Cu (0.61721), and one high negative contribution for Al (-0.50469). This shows that PC1 is under the control of anthropogenic sources, that is, metal processing and industrial emissions. Copper and zinc are widely used in galvanization, metal alloying, and electronics production, while aluminium negative loading may indicate a geogenic dilution or an alternative natural background source. Hence, PC1 may reflect mixed inputs from industrial processes and natural geological backgrounds. The second emponent (PC2) accounted for 36.05% of the variance and had significant positive loadings for K (0.60149) and Al (0.46336), and a significant negative loading for As (-0.60607). This component would indicate natural sources and agricultural amendments. Potassium and aluminum are usually from soil minerals and rock weathering, while arsenic, as it is both geogenic and anthropogenic, has a reverse pattern—likely due to leaching or differential mobility in soil systems. Thus, PC2 could be related to lithogenic inputs as well as application of phosphate fertilizers and pesticides mobilizing arsenic.

Table 4.10:	Principal	component	analysis of	of trace	metals	in honev	samples

Metals	PC 1	PC 2
K	0,03917	0,60149
Zn	0,60104	0,22029
Cu	0,61721	0,0875
Al	-0,50469	0,46336
As	-0,03941	-0,60607
Eigenvalue	2,384	1,802
Variance (%)	47,683	36,046
Cumulative (%)	47,683	83,729

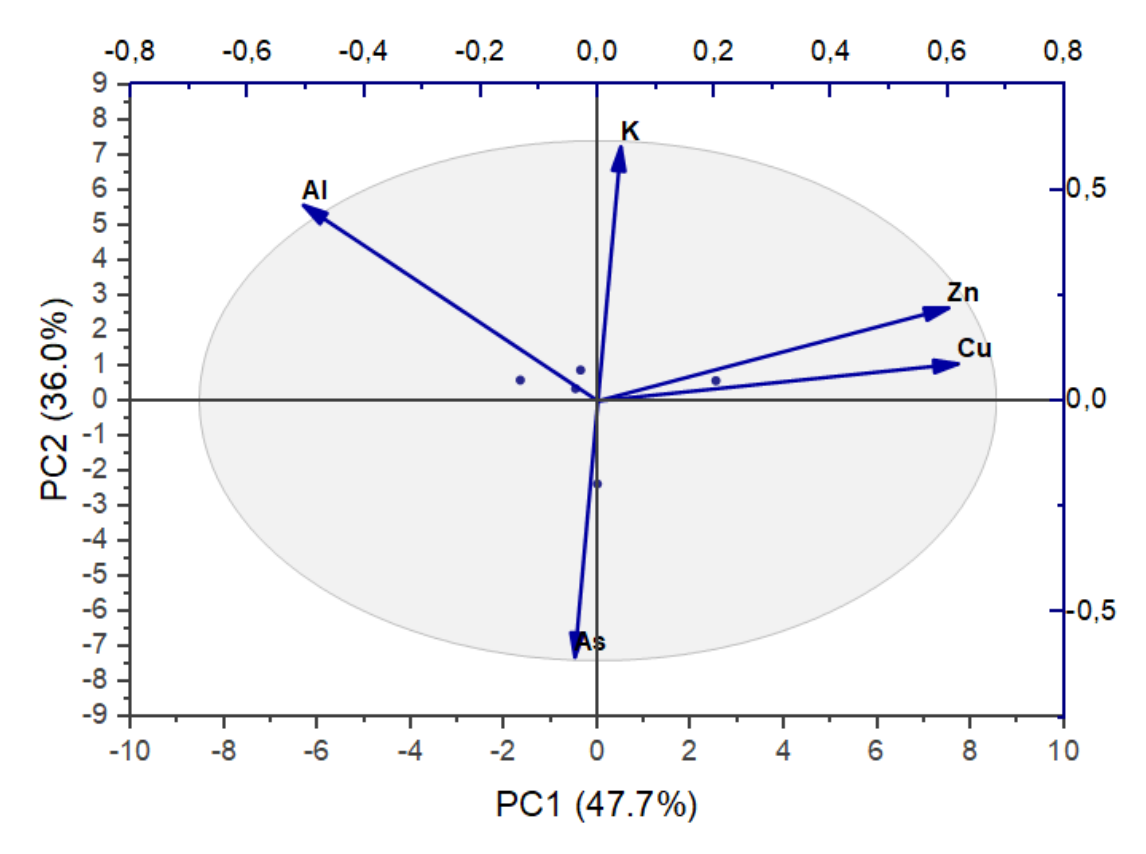


Figure 4.12: PCA analysis loading 2-D plot (PC 1 vs PC 2) for heavy metals in honey

Hierarchical Cluster Analysis

Hierarchical cluster analysis was conducted to analyze which sampling locations had similar metals concentration to evaluate honey samples having comparable properties. According

to the hierarchical dendrogram showed in Figure 4.13, K and Al grouped together in the first cluster, which indicated a highly similar occurrence or concentration profile of these two elements among the honey samples. Zn grouped with them later, which indicated a moderate degree of similarity among these three elements. Cu grouped at the lower similarity level, which indicated a more differential nature or source. As diverged as an outlier, joining the others only at the lowest similarity level, which means that it has a disparate distribution or potential source of contamination in the honey. Cluster pattern may be a sign of differences in floral origin, environmental contact, or human-modified inputs contributing to honey composition. These results showed good agreement with those of the pearson's correlation and principal component analysis.

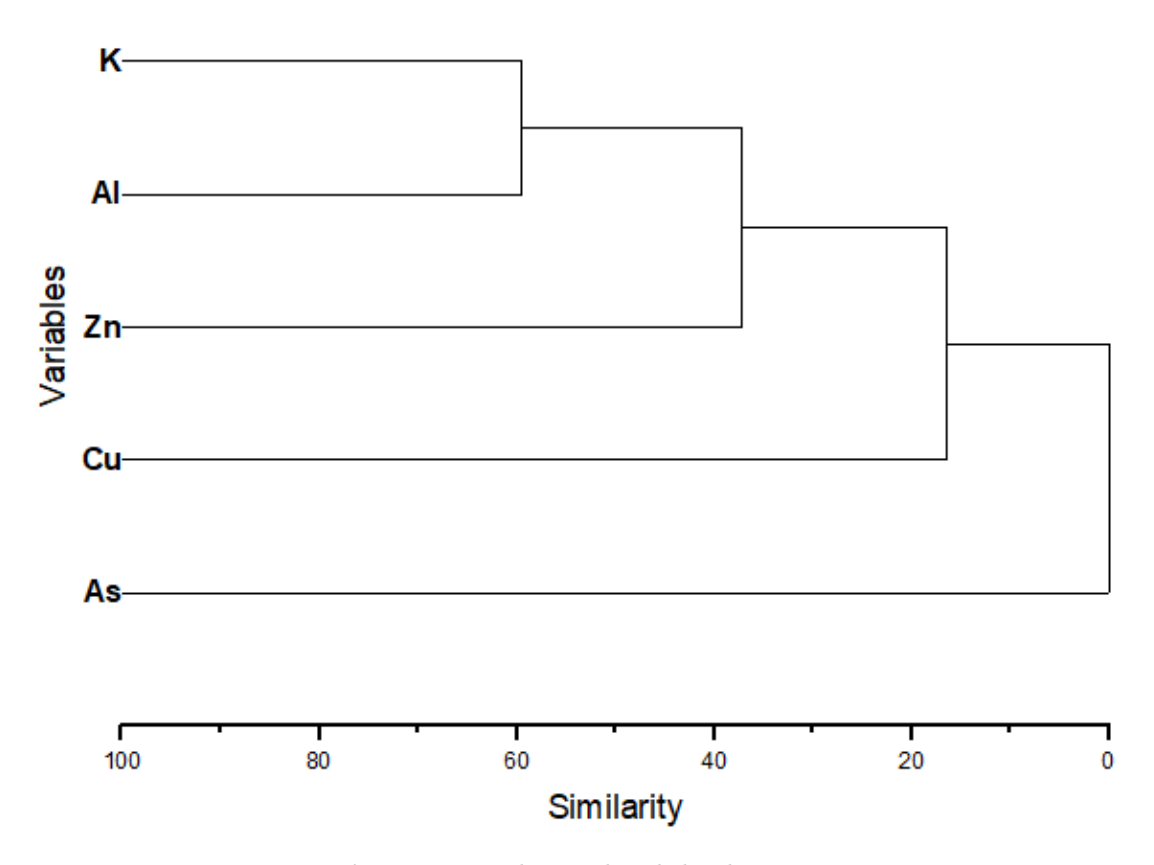


Figure 4.13: hierarchical dendrogram

4.4 Experimental Analysis of Antibiotics Residues Contamination

4.4.1 Antibiotics residues concentrations

Antimicrobial residues in honey are a significant concern due to their potential health risks and impact on food safety. The analysis of antibiotic residues in honey samples was conducted using two kits: TETH-012B for tetracyclines (chlortetracycline, oxytetracycline, and tetracycline) and ATBLH-007C for chloramphenicol. For tetracyclines, the detection limits were set at 10 ppb for chlortetracycline, 20 ppb for oxytetracycline, and 15 ppb for tetracycline. The control point for the assay was 1332 cpm, with negative and positive controls recording 1583 cpm and 864 cpm, respectively. All honey samples showed cpm values ranging from 1399 to 2231, which were higher than the negative control but lower than the positive control, indicating no detectable tetracycline residues above the specified limits. Consequently, all samples were classified as "Negative" for tetracycline residues.

For chloramphenicol analysis, the detection limit was set at 0.3 ppb. The control point for this assay was 1196 cpm, with negative and positive controls recording 1795 cpm and 1083 cpm, respectively. The cpm values for all honey samples ranged from 1232 to 1343, which were below the negative control but above the positive control, confirming the absence of chloramphenicol residues above the detection limit. As a result, all samples were also classified as "Negative" for chloramphenicol residues.

	Table 4.11:	Tetracyclines	Residue	Detection	Results	and	Sample	Analysis
--	-------------	---------------	---------	-----------	---------	-----	--------	----------

Sample ID	Kit	Detection Limit (ppb)	Control pointe (cpm)	Negative Control (cpm)	Positive Control (cpm)	Sample value value	Decision
H1		Chlortetracycline				2098	
H2		10				2022	
H3		Oxytetracycline				1399	
H4		20				1975	
H5	TETH012B	Teracycline	1332	1583	864	2096	Negative
H6		15				1829	
H7						2231	
H8						2036	
H9						2056	

Table 4.12: Chloramphenicol Residue Detection Results and Sample Analysis

Sample ID	Kit	Detection Limit (ppb)	Control pointe (cpm)	Negative Control (cpm)	Positive Control (cpm)	Sample value value	Decision
H1						1291	
H2						1211	
H3						1327	
H4						1328	
H5	ATBLH007C	0.3	1196	1795	1083	1343	Negative
H6						1338	
H7						1232	
H8						1277	
Н9						1283	

The results presnet in tables 4.11 and 4.12 indicate that none of the analyzed honey samples contained detectable levels of tetracycline or chloramphenicol residues, as all cpm values fell within the acceptable ranges defined by the respective negative and positive controls. For tetracyclines, the cpm values of the samples were consistently higher than the negative control and lower than the positive control, confirming compliance with regulatory limits. Similarly, for chloramphenicol, the cpm values of the samples were below the negative control but above the positive control, further validating the absence of residues. These findings are consistent with honey produced under regulated conditions, where the use of antibiotics is strictly controlled.

The absence of tetracycline and chloramphenicol residues in these samples highlights their compliance with international safety standards, ensuring consumer protection against potential antibiotic exposure. Chloramphenicol, in particular, is a banned substance in food production due to its severe health risks, and its absence in the tested samples underscores the quality and safety of the honey. These results align with previous studies that have reported low or undetectable levels of these antibiotics in honey from regions with stringent

General Conclusion

This thesis began by developing a Monte Carlo model of an HPGe detector using MCNP5 Code to simulate its efficiency for gamma spectrometry applications. The initial model was constructed based on the manufacturer's specifications; however, significant discrepancies were observed, particularly in the low-energy range(80%). These discrepancies highlighted the limitations of using nominal dimensions alone when simulating detector performance. To resolve this, the model was refined by adjusting the germanium crystal's dead layer thickness, which had a critical impact on the detector's low energy response. After optimization, the simulated full energy peak efficiencies showed excellent agreement with experimental values, with deviations reduced to less than 5% for low energies and less than 2% for higher energies.

Following validation with point sources, the model was extended to simulate the detector response for Marinelli beaker geometry, which is commonly used in environmental sample measurements such as honey. This geometry introduces additional complexities due to the sample's volume and its distribution around the detector, as well as the occurrence of True Coincidence Summing (TCS) effects that can significantly distort the measured efficiency, especially for radionuclides with cascade emissions. To account for these effects and ensure the reliability of the results, the Marinelli Efficiency Transfer software (MEFTTRAN) was applied for TCS correction. Despite these challenges, the refined Monte Carlo model maintained its accuracy and proved to be effective for complex geometries and real sample measurements.

In addition, two photon cross-section libraries—ENDF/B-VI and JENDL-5 were tested and compared to identify which dataset provided the best agreement with experimental results. This comparison was crucial, as the selected cross-section data have a direct impact on the simulated response of the HPGe detector. Moreover, understanding how each library performs in different energy ranges helped to choose the most suitable library for the specific energy interval relevant to this study. ANGLE software was employed in

estimates detection efficiency based on the effective solid angle, offering a semi-empirical method that complements the MCNP5 results and supports their validation.

Following its validation and optimization, the Monte Carlo model was applied to evaluate the radioactivity levels in honey samples of various botanical and geographical origins. These measurements focused on key naturally occurring radionuclides: 226 Ra, 232 Th, and 40 K. Special consideration was given to self-absorption effects within the honey matrix due to its high density (typically ranging 1.25 to 1.45 g/cm^3) and complex composition (sugars, water, organic acids, and trace minerals). These properties pose unique challenges for gamma spectrometry, such as photon attenuation and self-absorption, which significantly reduce low-energy gamma photon detection efficiency. By accurately modeling the matrix composition and density, the simulation accounted for these effects, ensuring reliable results.

The validated model allowed for the precise quantification of activity concentrations in the samples, which were subsequently used to calculate critical radiological hazard indices (AED, ELCR, Hin, RLI, and AGDE). The results confirmed that all measured values remained well within internationally accepted safety limits, as defined by UNSCEAR, WHO, and FAO, highlighting the radiological safety and high quality of Algerian honey. Beyond radioactivity measurements, this research also assessed the presence of other contaminants in honey, namely heavy metals and antibiotic residues (tetracycline and chloramphenicol residues), using Atomic Absorption Spectroscopy (AAS) and the CHARM II technique, respectively. These methods were selected to complement the radiological analysis and provide a broader evaluation of honey safety.

The spatial distribution of heavy metals (K, Zn, Cu, Al, As) in honey revealed clear correlations with both environmental pollution and botanical origin. Higher concentrations were observed in samples from industrial zones and during the summer season. Potassium (K) was the most abundant element, while trace metals like Cu, Al, and As showed elevated levels in honey collected near industrial or mining areas, reflecting the combined influence of anthropogenic activities and seasonal factors.

To interpret these complex datasets, multivariate statistical analyses—Principal Component Analysis (PCA) and Hierarchical Cluster Analysis (HCA)—were employed. These methods successfully identified contamination patterns, revealed significant correlations, and enabled differentiation between samples from industrial versus non-industrial zones.

Finally, CHARM II analysis confirmed the absence of tetracycline and chloramphenicol residues in all tested samples, demonstrating compliance with international food safety standards and underscoring the honey's microbiological quality. Together, these results validate the effectiveness of combining simulation-based approaches with multicontaminant experimental analysis for comprehensive food safety assessment.

Looking forward, future research could investigate the specific sources and pathways of honey contamination—such as pollutants from soil, irrigation water, and atmospheric deposition—providing insights into environmental exposure routes. Additionally, advances in simulation tools and high-resolution spectrometry could further enhance the precision and efficiency of contaminant detection. The integration of machine learning, such as deep learning algorithms for spectral deconvolution and contamination pattern prediction, holds great promise for accelerating analysis and improving decision-making in food safety monitoring.

Bibliography

- [1] M. F. Aydın, Ö. Söğüt, and A. Kara, "Radiological health risks assessment of vegetable and fruit samples taken from the provincial borders of adıyaman in the southeastern anatolia region, in turkey," *Journal of Radiation Research and Applied Sciences*, vol. 15, no. 4, p. 100491, 2022.
- [2] H. Younis, M. A. Ahmad, U. Azeem, M. R. Shaik, A. Al-Warthan, B. Shaik, A. Jagnandan, S. Jagnandan, and M. Ajaz, "Comprehensive analysis of contaminants in powdered milk samples using an hpge for γ radiation," *ACS omega*, vol. 9, no. 19, pp. 21089–21096, 2024.
- [3] S. Pervin, M. M. Kabir, M. J. Dewan, M. U. Khandaker, and S. Yeasmin, "Evaluation of radioactivity concentration in farm fresh milk and concomitant dose to consumer," *Heliyon*, vol. 10, no. 9, 2024.
- [4] S. Samarghandian, T. Farkhondeh, and F. Samini, "Honey and health: A review of recent clinical research," *Pharmacognosy research*, vol. 9, no. 2, p. 121, 2017.
- [5] A. Ajibola, "Novel insights into the health importance of natural honey," *The Malaysian journal of medical sciences: MJMS*, vol. 22, no. 5, p. 7, 2015.
- [6] F. Livens, "Measurement of radionuclides in food and the environment. a guidebook: Technical reports series no. sti/doc/010/295 trs 295. iaea, vienna, austria, 1989. isbn 92 0 125189 0," Journal of Environmental Radioactivity, vol. 11, no. 2, pp. 201–202, 1990.
- [7] U. Rizwan, A. Chester, T. Domingo, K. Starosta, J. Williams, and P. Voss, "A method for establishing absolute full-energy peak efficiency and its confidence interval for hpge detectors," Nuclear Instruments and Methods in Physics Research Section A: Accelerators, Spectrometers, Detectors and Associated Equipment, vol. 802, pp. 102–112, 2015.

- [8] S. Jonsson, J. Kastlander, T. Vidmar, and H. Ramebäck, "Experimental validation of corrections factors for γ – γ and γ –x coincidence summing of 133 ba, 152 eu, and 125 sb in volume sources," *Journal of Radioanalytical and Nuclear Chemistry*, vol. 323, pp. 465–472, 2020.
- [9] A. A. Thabet, A. D. Dlabac, S. I. Jovanovic, M. S. Badawi, N. N. Mihaljevic, A. M. El-Khatib, M. M. Gouda, and M. I. Abbas, "Experimental verification of gamma-efficiency calculations for scintillation detectors in angle 4 software," *Nuclear Technology and Radiation Protection*, vol. 30, no. 1, pp. 35–46, 2015.
- [10] J. K. Nikolic, M. Rajacic, D. Todorovic, and T. Vidmar, "The first experimental test of the mefftran software on hpge detector calibration for environmental samples," *Journal of Environmental Radioactivity*, vol. 165, pp. 191–196, 2016.
- [11] S. Bartha, I. Taut, G. Goji, I. A. Vlad, and F. Dinulică, "Heavy metal content in polyfloralhoney and potential health risk. a case study of copșa mică, romania," *International Journal of Environmental Research and Public Health*, vol. 17, no. 5, p. 1507, 2020.
- [12] V. Šerevičienė, A. Zigmontienė, and D. Paliulis, "Heavy metals in honey collected from contaminated locations: a case of lithuania," *Sustainability*, vol. 14, no. 15, p. 9196, 2022.
- [13] B. Mitrović, D. Todorović, J. Ajtić, and B. Vranješ, "A review: Natural and artificial radionuclides and radiation hazard parameters in the soil of mountain regions in serbia," *Journal of Agricultural Sciences (Belgrade)*, vol. 65, no. 1, pp. 1–18, 2020.
- [14] N.-E. C. Ereh and M. Zhang, "Environmental radiation measurement and assessment of natural radioactivity in soil, water and vegetation," *Journal of Applied Mathematics and Physics*, vol. 6, no. 11, pp. 2330–2337, 2018.
- [15] A. Dołhańczuk-Śródka, "Estimation of external gamma radiation dose in the area of bory stobrawskie forests (pl)," *Environmental monitoring and assessment*, vol. 184, pp. 5773–5779, 2012.
- [16] T. H. Park, D. R. Kang, S. H. Park, D. K. Yoon, and C. M. Lee, "Indoor radon concentration in korea residential environments," *Environmental Science and Pollution Research*, vol. 25, pp. 12678–12685, 2018.
- [17] P. Airey, T. Hinton, and J. Twining, "The scientific basis," in *Radioactivity in the Environment*, vol. 18, pp. 1–57, Elsevier, 2012.

- [18] E. B. De Souza, B. Park, G. Adhikari, P. Adhikari, N. Carlin, J. Choi, S. Choi, M. Djamal, A. Ezeribe, C. Ha, et al., "Study of cosmogenic radionuclides in the cosine-100 nai (tl) detectors," Astroparticle Physics, vol. 115, p. 102390, 2020.
- [19] V. Saenko, V. Ivanov, A. Tsyb, T. Bogdanova, M. Tronko, Y. Demidchik, and S. Yamashita, "The chernobyl accident and its consequences," *Clinical Oncology*, vol. 23, no. 4, pp. 234–243, 2011.
- [20] P. Danesi, J. Moreno, M. Makarewicz, and D. Louvat, "Residual radionuclide concentrations and estimated radiation doses at the former french nuclear weapons test sites in algeria," Applied Radiation and Isotopes, vol. 66, no. 11, pp. 1671–1674, 2008.
- [21] V. Chandra, K. Arpita, P. Yadav, V. Raghuvanshi, A. Yadav, and S. Prajapati, "Environmental biotechnology for medical waste management: A review of current practices and future directions," *Annals of Biomedical Sciences*, vol. 6, no. 2, pp. 1–9, 2023.
- [22] G. Gilmore and D. Joss, *Practical gamma-ray spectrometry*. John Wiley & Sons, 2024.
- [23] B. Girolamo and M. Nessi, "Silicon trackers," 2014.
- [24] L. S. Darken and C. E. Cox, "High-purity germanium detectors," *Semiconductors* and *Semimetals*, vol. 43, pp. 23–83, 1995.
- [25] K. Bergaoui, N. Reguigui, C. Gary, C. Brown, J. Cremer, J. Vainionpaa, and M. Piestrup, "Development of a new deuterium-deuterium (d-d) neutron generator for prompt gamma-ray neutron activation analysis," *Applied Radiation and Isotopes*, vol. 94, pp. 319–327, 2014.
- [26] G. F. Knoll, Radiation detection and measurement. John Wiley & Sons, 2010.
- [27] M. Amman, "Optimization of amorphous germanium electrical contacts and surface coatings on high purity germanium radiation detectors," arXiv preprint arXiv:1809.03046, 2018.
- [28] Q. Looker, Fabrication process development for high-purity germanium radiation detectors with amorphous semiconductor contacts. University of California, Berkeley, 2014.

- [29] P. Wallbrink, D. Walling, and Q. He, "Radionuclide measurement using hpge gamma spectrometry," in *Handbook for the assessment of soil erosion and sedimentation using environmental radionuclides*, pp. 67–96, Springer, 2002.
- [30] S. R. Cherry, J. A. Sorenson, and M. E. Phelps, "Radiation detectors," *Physics in Nuclear Medicine*. 4th ed. Elsevier, pp. 87–106, 2012.
- [31] J. G. Webster and H. Eren, Measurement, instrumentation, and sensors handbook: spatial, mechanical, thermal, and radiation measurement. CRC press, 2017.
- [32] F. B. Brown, R. Barrett, T. Booth, J. Bull, L. Cox, R. Forster, T. Goorley, R. Mosteller, S. Post, R. Prael, et al., "Mcnp version 5," Trans. Am. Nucl. Soc, vol. 87, no. 273, pp. 02–3935, 2002.
- [33] A. Maurotto, S. Rizzo, and E. Tomarchio, "Mcnp5 modelling of hpge detectors for efficiency evaluation in γ-ray spectrometry," Radiation Effects and Defects in Solids, vol. 164, no. 5-6, pp. 302–306, 2009.
- [34] R. A. Forster, L. J. Cox, R. F. Barrett, T. E. Booth, J. F. Briesmeister, F. B. Brown, J. S. Bull, G. C. Geisler, J. T. Goorley, R. D. Mosteller, et al., "McnpTM version 5," Nuclear Instruments and Methods in Physics Research Section B: Beam Interactions with Materials and Atoms, vol. 213, pp. 82–86, 2004.
- [35] C. Werner, "Mcnp users manual-code version 6.2 (report, la-ur-17-29981)," New Mexico: Los Alamos National Laboratory, 2017.
- [36] T. Goorley, M. James, T. Booth, F. Brown, J. Bull, L. J. Cox, J. Durkee, J. Elson, M. Fensin, R. Forster, et al., "Initial mcnp6 release overview," Nuclear technology, vol. 180, no. 3, pp. 298–315, 2012.
- [37] D. B. Pelowitz, J. Goorley, and M. Fensin, "Mcnp6 user's manual version 1.0: Lacp-13-00634 rev. 0," Los Alamos National Laboratory, Los Alamos, vol. 104, 2013.
- [38] J. S. Hendricks, G. W. McKinney, L. S. Waters, T. L. Roberts, H. W. Egdorf, J. P. Finch, H. R. Trellue, E. J. Pitcher, D. R. Mayo, M. T. Swinhoe, et al., "Mcnpx extensions version 2.5. 0," Los Alamos National Laboratory, vol. 15, 2005.
- [39] I. M. Nabil, K. El-Kourghly, and A. F. El Sayed, "A semi-empirical method for efficiency calibration of an hpge detector against different sample densities," *Applied Radiation and Isotopes*, vol. 200, p. 110946, 2023.

- [40] G. Stanić, J. Nikolov, I. Tucaković, D. Mrđa, N. Todorović, Ž. Grahek, I. Coha, and A. Vraničar, "Angle vs. labsocs for hpge efficiency calibration," *Nuclear Instruments and Methods in Physics Research Section A: Accelerators, Spectrometers, Detectors and Associated Equipment*, vol. 920, pp. 81–87, 2019.
- [41] O. Sima and D. Arnold, "Accurate computation of coincidence summing corrections in low level gamma-ray spectrometry," *Applied Radiation and Isotopes*, vol. 53, no. 1-2, pp. 51–56, 2000.
- [42] R. Abi Njoh, K. Kocadal, F. Alkas, M. A. Kurt, D. Battal, and S. Saygi, "Heavy metal pollution of agricultural soils and vegetables of abandoned mining district in northern cyprus," *Fresenius Environ Bull*, vol. 30, pp. 1415–1423, 2021.
- [43] A. Alengebawy, S. T. Abdelkhalek, S. R. Qureshi, and M.-Q. Wang, "Heavy metals and pesticides toxicity in agricultural soil and plants: Ecological risks and human health implications," *Toxics*, vol. 9, no. 3, p. 42, 2021.
- [44] H. Tutun, H. A. Kahraman, Y. Aluc, T. Avci, and H. Ekici, "Investigation of some metals in honey samples from west mediterranean region of turkey," in *Veterinary Research Forum*, vol. 10, p. 181, 2019.
- [45] G. Pandey and S. Madhuri, "Heavy metals causing toxicity in animals and fishes," Research Journal of Animal, Veterinary and Fishery Sciences, vol. 2, no. 2, pp. 17–23, 2014.
- [46] E. Huskisson, S. Maggini, and M. Ruf, "The role of vitamins and minerals in energy metabolism and well-being," *Journal of international medical research*, vol. 35, no. 3, pp. 277–289, 2007.
- [47] I. A. Odongo, S. A. Opiyo, P. W. Njoroge, and E. T. Osewe, "Heavy metal pollution in water, detection and remediations strategies," 2025.
- [48] A. F. Lagalante, "Atomic absorption spectroscopy: A tutorial review," *Applied Spectroscopy Reviews*, vol. 34, no. 3, pp. 173–189, 2004.
- [49] S. Singhal and A. Singh, "Atomic absorption spectrophotometric method for the estimation of micronutrients in soil and their effect on plant growth," ES Food & Agroforestry, vol. 18, p. 1188, 2024.
- [50] S. J. Hill and A. S. Fisher, "Atomic absorption, methods and instrumentation," in *Encyclopedia of Spectroscopy and Spectrometry, Second Edition*, pp. 46–53, 2010.

- [51] I. Bankaji, R. Kouki, N. Dridi, R. Ferreira, S. Hidouri, B. Duarte, N. Sleimi, and I. Caçador, "Comparison of digestion methods using atomic absorption spectrometry for the determination of metal levels in plants," *Separations*, vol. 10, no. 1, p. 40, 2023.
- [52] M. A. Farrukh, Atomic absorption spectroscopy. BoD-Books on Demand, 2012.
- [53] R. Sturgeon, "Atomic absorption spectrometry vapor generation," 2005.
- [54] C. Chakrabarti, "Atomic spectroscopy, historical perspective," 1999.
- [55] K. O. Omeje, B. O. Ezema, F. Okonkwo, N. C. Onyishi, J. Ozioko, W. A. Rasaq, G. Sardo, and C. O. R. Okpala, "Quantification of heavy metals and pesticide residues in widely consumed nigerian food crops using atomic absorption spectroscopy (aas) and gas chromatography (gc)," Toxins, vol. 13, no. 12, p. 870, 2021.
- [56] S. L. Ferreira, M. A. Bezerra, A. S. Santos, W. N. dos Santos, C. G. Novaes, O. M. de Oliveira, M. L. Oliveira, and R. L. Garcia, "Atomic absorption spectrometry—a multi element technique," *TrAC Trends in Analytical Chemistry*, vol. 100, pp. 1–6, 2018.
- [57] G. Butler, "The legal relations of the european union with the republic of san marino," European Foreign Affairs Review, vol. 29, no. 3, 2024.
- [58] W. Reybroeck, E. Daeseleire, H. F. De Brabander, and L. Herman, "Antimicrobials in beekeeping," *Veterinary microbiology*, vol. 158, no. 1-2, pp. 1–11, 2012.
- [59] H. Rodrigues, M. Leite, B. Oliveira, and A. Freitas, "Antibiotics in honey: A comprehensive review on occurrence and analytical methodologies," *Open Research Europe*, vol. 4, p. 125, 2024.
- [60] L. R. Guidi, P. A. Tette, C. Fernandes, L. H. Silva, and M. B. A. Gloria, "Advances on the chromatographic determination of amphenicals in food," *Talanta*, vol. 162, pp. 324–338, 2017.
- [61] I. G. David, M. Buleandra, D. E. Popa, M. C. Cheregi, and E. E. Iorgulescu, "Past and present of electrochemical sensors and methods for amphenical antibiotic analysis," *Micromachines*, vol. 13, no. 5, p. 677, 2022.
- [62] A. K. Mukota, M. F. K. Gondam, J. J. T. Tsafack, J. Sasanya, W. Reybroeck, M. Ntale, S. A. Nyanzi, and E. Tebandeke, "Primary validation of charm ii tests

- for the detection of antimicrobial residues in a range of aquaculture fish," *BMC* chemistry, vol. 14, pp. 1–15, 2020.
- [63] S. Kwon, G. Owens, Y. Ok, D. Lee, W.-T. Jeon, J. Kim, and K.-R. Kim, "Applicability of the charm ii system for monitoring antibiotic residues in manure-based composts," Waste Management, vol. 31, no. 1, pp. 39–44, 2011.
- [64] J. M. Pacyna, E. G. Pacyna, and W. Aas, "Changes of emissions and atmospheric deposition of mercury, lead, and cadmium," *Atmospheric environment*, vol. 43, no. 1, pp. 117–127, 2009.
- [65] Z. Long, H. Zhu, H. Bing, X. Tian, Z. Wang, X. Wang, and Y. Wu, "Contamination, sources and health risk of heavy metals in soil and dust from different functional areas in an industrial city of panzhihua city, southwest china," *Journal of Hazardous Materials*, vol. 420, p. 126638, 2021.
- [66] , , , , , , and , "Activity concentrations and radiological hazard assessments of 226ra, 232th, 40k, and 137cs in soil samples obtained from the dongnam institute of radiological & medical science, korea," *Nuclear Engineering and Technology*, vol. 55, no. 7, pp. 2388–2394, 2023.
- [67] C. M. G. Lima, F. M. Dalla Nora, S. K. T. Seraglio, J. M. da Silva, H. J. Marzoque, R. F. Santana, S. Verruck, and V. M. Scussel, "Antibiotic residues in honey: A public health issue," *Research, Society and Development*, vol. 9, no. 11, pp. e1739119604 e1739119604, 2020.
- [68] C. A. Mullin, M. Frazier, J. L. Frazier, S. Ashcraft, R. Simonds, D. Van Engelsdorp, and J. S. Pettis, "High levels of miticides and agrochemicals in north american apiaries: implications for honey bee health," *PloS one*, vol. 5, no. 3, p. e9754, 2010.
- [69] A. Nowak and I. Nowak, "Review of harmful chemical pollutants of environmental origin in honey and bee products," Critical Reviews in Food Science and Nutrition, vol. 63, no. 21, pp. 5094–5116, 2023.
- [70] S. Bogdanov, "Contaminants of bee products," *Apidologie*, vol. 37, no. 1, pp. 1–18, 2006.
- [71] E. Chham, F. P. García, T. El Bardouni, M. A. Ferro-García, M. Azahra, K. Benaalilou, M. Krikiz, H. Elyaakoubi, J. El Bakkali, and M. Kaddour, "Monte carlo analysis of the influence of germanium dead layer thickness on the hpge gamma

- detector experimental efficiency measured by use of extended sources," Applied Radiation and Isotopes, vol. 95, pp. 30–35, 2015.
- [72] S. Gallardo, A. Querol, J. Ortiz, J. Ródenas, G. Verdú, and J. Villanueva, "Uncertainty analysis in environmental radioactivity measurements using the monte carlo code mcnp5," *Radiation Physics and Chemistry*, vol. 116, pp. 214–218, 2015.
- [73] M.-C. Lépy, C. Thiam, M. Anagnostakis, R. Galea, D. Gurau, S. Hurtado, K. Karfopoulos, J. Liang, H. Liu, A. Luca, et al., "A benchmark for monte carlo simulation in gamma-ray spectrometry," Applied Radiation and Isotopes, vol. 154, p. 108850, 2019.
- [74] S. Penabeï, D. Bongue, A. Mistura, P. Maleka, K. Demdah, and G. Kwato, "Simulation of p-type hpge detector full-energy peak efficiency using geant4 monte carlo toolkit," *International Journal of Environmental Science and Technology*, vol. 21, no. 4, pp. 4509–4518, 2024.
- [75] G. Mellak, W. Boukhenfouf, F. Z. Dehimi, A. Messai, and N. E. Hebboul, "Investigating cross-section effects on hpge detector response through computational and empirical approaches," *Applied Radiation and Isotopes*, vol. 216, p. 111596, 2025.
- [76] M. Zadehrafi, A. Luca, and M. Ioan, "Determination of si (li) detector efficiency by experimental and monte carlo simulation methods," *Physica Scripta*, vol. 96, no. 5, p. 055302, 2021.
- [77] H. D. Chuong, N. T. T. Linh, V. H. Nguyen, L. H. Minh, C. T. Tai, T. T. Thanh, et al., "A simple approach for developing model of si (li) detector in monte carlo simulation," Radiation Physics and Chemistry, vol. 166, p. 108459, 2020.
- [78] O. Iwamoto, N. Iwamoto, S. Kunieda, F. Minato, S. Nakayama, Y. Abe, K. Tsubakihara, S. Okumura, C. Ishizuka, T. Yoshida, et al., "Japanese evaluated nuclear data library version 5: Jendl-5," Journal of Nuclear Science and Technology, vol. 60, no. 1, pp. 1–60, 2023.
- [79] S. M. Zamzamian, S. A. Hosseini, and M. Samadfam, "Optimization of the marinelli beaker dimensions using genetic algorithm," *Journal of Environmental Radioactiv*ity, vol. 172, pp. 81–88, 2017.
- [80] P. P. Aguiar-Amado, V. A. Amado, and J. C. Aguiar, "Full-energy peak determination from total efficiency and peak-to-total ratio calculations," *Nuclear Instruments*

- and Methods in Physics Research Section A: Accelerators, Spectrometers, Detectors and Associated Equipment, vol. 990, p. 164980, 2021.
- [81] J. Wu, L. Shen, G. Zhang, Z. Zhou, and Q. Zhu, "Efficiency evaluation with data uncertainty," *Annals of Operations Research*, vol. 339, no. 3, pp. 1379–1403, 2024.
- [82] D. A. Aloraini, M. Elsafi, A. H. Almuqrin, and M. Sayyed, "Coincidence summing factor calculation for volumetric γ-ray sources using geant4 simulation," Science and Technology of Nuclear Installations, vol. 2022, no. 1, p. 5718920, 2022.
- [83] T. M. Semkow, G. Mehmood, P. P. Parekh, and M. Virgil, "Coincidence summing in gamma-ray spectroscopy," Nuclear Instruments and Methods in Physics Research Section A: Accelerators, Spectrometers, Detectors and Associated Equipment, vol. 290, no. 2-3, pp. 437–444, 1990.
- [84] C. Agarwal, S. Chaudhury, A. Goswami, and M. Gathibandhe, "True coincidence summing corrections in point and extended sources," *Journal of Radioanalytical and Nuclear Chemistry*, vol. 289, no. 3, pp. 773–780, 2011.
- [85] G. P. Verma, Abhigyan, R. Prakash, S. Sahoo, A. Patra, S. Jha, and M. Kulkarni, "Gross alpha activity measurements: Investigating the crucial role of self-absorption correction factors," *MAPAN*, vol. 39, no. 1, pp. 69–75, 2024.
- [86] I. Alafogiannis, F. Tugnoli, I. Mitsios, and M. Anagnostakis, "Development of a computer code for the calculation of self-absorption correction factors in γ-spectrometry applications," HNPS Advances in Nuclear Physics, vol. 28, pp. 98–103, 2021.
- [87] S. Bell, S. Judge, and P. Regan, "An investigation of hpge gamma efficiency calibration software (angle v. 3) for applications in nuclear decommissioning," *Applied Radiation and Isotopes*, vol. 70, no. 12, pp. 2737–2741, 2012.
- [88] M. Miller and M. Voutchkov, "Modeling the impact of uncertainty in detector specification on efficiency values of a hpge detector using angle software," Nuclear Technology and Radiation Protection, vol. 28, no. 2, pp. 169–181, 2013.
- [89] L. A. Currie, "Limits for qualitative detection and quantitative determination. application to radiochemistry," *Analytical chemistry*, vol. 40, no. 3, pp. 586–593, 1968.
- [90] S. Pervin, M. J. Dewan, A. M. Apon, M. M. Siraz, and S. Yeasmin, "Measurement of natural radioactivity and its health hazards associated with the use of different branded cement samples collected from different manufactures in dhaka city using

- gamma spectrometry," Journal of Bangladesh Academy of Sciences, vol. 45, no. 1, pp. 95–104, 2021.
- [91] R. Salter, "Charm ii system-comprehensive residue analysis system for honey," *Apiacta*, vol. 38, pp. 198–206, 2003.
- [92] M. Beltrán, T. Romero, R. L. Althaus, and M. Molina, "Evaluation of the charm maximum residue limit β-lactam and tetracycline test for the detection of antibiotics in ewe and goat milk," Journal of dairy science, vol. 96, no. 5, pp. 2737–2745, 2013.
- [93] U. Nations, "Sources and effects of ionizing radiation," UNSCEAR Report, 1993.
- [94] J. Gray, "Quantum gis: the open-source geographic information system," *Linux Journal*, vol. 2008, p. 8, 01 2008.
- [95] K. Asaduzzaman, M. Khandaker, Y. Amin, and R. Mahat, "Uptake and distribution of natural radioactivity in rice from soil in north and west part of peninsular malaysia for the estimation of ingestion dose to man," *Annals of Nuclear Energy*, vol. 76, pp. 85–93, 2015.
- [96] L. Haderbache and A. Mohammedi, "Etude sur le comportement de consommation du miel en algérie : attentes et préférences," Revue Agriculture fsnv, vol. 09, pp. 19– 24, 04 2015.
- [97] M. A. Meli, D. Desideri, P. Battisti, I. Giardina, D. Gorietti, and C. Roselli, "Assessment of radioactivity in commercially available honey in italy," Food Control, vol. 110, p. 107001, 2020.
- [98] L. Tettey-Larbi, E. O. Darko, C. Schandorf, and A. A. Appiah, "Natural radioactivity levels of some medicinal plants commonly used in ghana," *SpringerPlus*, vol. 2, pp. 1–9, 2013.
- [99] U. N. S. C. on the Effects of Atomic Radiation, B. Annex, et al., "Exposures from natural radiation sources," Cosmic rays, vol. 9, no. 11, 2000.
- [100] L. Semerjian, H. Alrajaby, N. Naaz, R. Kasfah, E. Z. Dalah, E. Waheed, A. Nabulssi, and W. A. Metwally, "Age-dependent effective ingestion dose estimations and lifetime risk assessment for selected radionuclides (40k and 3h) in bottled waters marketed in united arab emirates," Chemosphere, vol. 249, p. 126114, 2020.

- [101] J. Valentin, "International commission on radiological protection. the 2007 recommendations of the international commission on radiological protection," Annals of the ICRP, ICRP Publication, vol. 103, pp. 2–4, 2007.
- [102] F. Flici and M. Chinoune, "Analysis of recent changes in chronic disease-free life expectancy in algeria," *Eastern Mediterranean Health Journal*, vol. 28, no. 12, pp. 872–878, 2022.
- [103] N. F. Salih, "Measurement the natural radioactivity concentration levels of radionuclides in selected vegetables collected from kirkuk, iraq using hpge detector," *International Journal of Environmental Analytical Chemistry*, vol. 103, no. 6, pp. 1323–1342, 2023.
- [104] UNSCEAR, "Sources and effects of ionizing radiation /," p. 89 p. :, 2000. Includes bibliographical references.
- [105] A. Patra, S. Mohapatra, S. Sahoo, P. Lenka, J. Dubey, R. Tripathi, and V. Puranik, "Age-dependent dose and health risk due to intake of uranium in drinking water from jaduguda, india," *Radiation protection dosimetry*, vol. 155, no. 2, pp. 210–216, 2013.
- [106] M. Charles, "Effects of ionizing radiation: United nations scientific committee on the effects of atomic radiation: Unscear 2006 report, volume 1—report to the general assembly, with scientific annexes a and b," 2010.
- [107] J. T. K. Ndondo, "Review of the food and agriculture organisation (fao) strategic priorities on food safety 2023," in *Food Safety-New Insights*, IntechOpen, 2023.
- [108] F. Caridi, V. Venuti, G. Paladini, V. Crupi, G. Belmusto, and D. Majolino, "The radioactivity distribution and radiation hazard in honey samples from italian large retailers," in *Journal of Physics: Conference Series*, vol. 2162, p. 012002, IOP Publishing, 2022.
- [109] M. H. Borawska, J. Kapała, A. Puścion-Jakubik, J. Horembała, and R. Markiewicz-Żukowska, "Radioactivity of honeys from poland after the fukushima accident," Bulletin of environmental contamination and toxicology, vol. 91, pp. 489–492, 2013.
- [110] E. Altekin, S. Dizman, and R. Keser, "Radioactivity and heavy metal concentrations in various honey samples," *Journal of Environmental Protection and Ecology*, vol. 16, no. 2, pp. 716–722, 2015.

- [111] G. Bulubasa, D. Costinel, A. F. Miu, and M. R. Ene, "Activity concentrations of 238u, 232th, 226ra 137cs and 40k radionuclides in honey samples from romania. lifetime cancer risk estimated," *Journal of Environmental Radioactivity*, vol. 234, p. 106626, 2021.
- [112] H. M. Abdullah, K. S. Jassim, and I. H. Kadhim, "The natural radioactivity distribution and radiation hazard in honey bees samples.," 2019.
- [113] S. Dizman, G. Hodolli, S. Kadiri, H. Aliu, and S. Makolli, "Radioactivity in kosovo honey samples," *Polish Journal of Environmental Studies*, vol. 29, no. 2, pp. 1119–1127, 2020.
- [114] M. U. Khandaker, N. S. Zayadi, S. F. A. Sani, D. A. Bradley, H. Osman, Y. Alzamil, M. Almeshari, M. Sayyed, and A. Sulieman, "Norm in cultivated honey in malaysia and concomitant effective dose to consumers," *Radiation Protection Dosimetry*, vol. 199, no. 18, pp. 2174–2178, 2023.
- [115] Ž. Mihaljev, S. Jakšić, M. Živkov-Baloš, and N. Popov, "Radioactive residue in honey," 2021.
- [116] K. Beňová, P. Dvořák, and M. Špalková, "Radiocaesium in honey from košice and prešov regions in eastern slovakia," *Folia Veterinaria*, vol. 63, no. 4, pp. 27–32, 2019.
- [117] D. C. Xarchoulakos and M. Lasithiotakis, "Radioactivity evaluation and radiation dosimetry assessment in greek honey," *Food Chemistry*, vol. 394, p. 133556, 2022.
- [118] E. Seifert, "Originpro 9.1: Scientific data analysis and graphing software software review," 2014.
- [119] H. F. Kaiser, "The application of electronic computers to factor analysis," *Educational and Psychological Measurement*, vol. 20, no. 1, pp. 141–151, 1960.
- [120] A. Chandrasekaran, R. Ravisankar, G. Senthilkumar, K. Thillaivelavan, B. Dhinakaran, P. Vijayagopal, S. Bramha, and B. Venkatraman, "Spatial distribution and lifetime cancer risk due to gamma radioactivity in yelagiri hills, tamilnadu, india," Egyptian Journal of Basic and Applied Sciences, vol. 1, no. 1, pp. 38–48, 2014.
- [121] A. Zergui, S. Boudalia, and M. L. Joseph, "Heavy metals in honey and poultry eggs as indicators of environmental pollution and potential risks to human health," *Journal of Food Composition and Analysis*, vol. 119, p. 105255, 2023.

- [122] A. ZERGUI, A. I. CHEBLI, M. A. KERDOUN, F. HAMITRI-GUERFI, R. MAY-OUF, H. TOUER, B. CHEFIRAT, and S. BOUDALIA, "Metallic contaminants in foodstuff consumed in algeria and associated health risks: A systematic review," *Journal of Trace Elements and Minerals*, vol. 12, p. 100235, 2025.
- [123] A. Ogunlaja, O. O. Ogunlaja, D. M. Okewole, and O. A. Morenikeji, "Risk assessment and source identification of heavy metal contamination by multivariate and hazard index analyses of a pipeline vandalised area in lagos state, nigeria," *Science of The Total Environment*, vol. 651, pp. 2943–2952, 2019.
- [124] USEPA, "Us (environmental protection agency) regional screening level (rsl) subchronic toxicity supporting table november," Regional Screening Level (RSL) Subchronic Toxicity Supporting Table November, 2020.
- [125] J. C. Egbueri, B. U. Ukah, O. E. Ubido, and C. O. Unigwe, "A chemometric approach to source apportionment, ecological and health risk assessment of heavy metals in industrial soils from southwestern nigeria," *International Journal of Environmental Analytical Chemistry*, vol. 102, no. 14, pp. 3399–3417, 2022.
- [126] M. Zhang, X. Wang, C. Liu, J. Lu, Y. Qin, Y. Mo, P. Xiao, and Y. Liu, "Quantitative source identification and apportionment of heavy metals under two different land use types: Comparison of two receptor models apcs-mlr and pmf," *Environmental Science and Pollution Research*, vol. 27, pp. 42996–43010, 2020.
- [127] H. Chen, D. Wu, Q. Wang, L. Fang, Y. Wang, C. Zhan, J. Zhang, S. Zhang, J. Cao, S. Qi, and S. Liu, "The predominant sources of heavy metals in different types of fugitive dust determined by principal component analysis (pca) and positive matrix factorization (pmf) modeling in southeast hubei: A typical mining and metallurgy area in central china," *International Journal of Environmental Research and Public Health*, vol. 19, no. 20, 2022.
- [128] F. Ilhan, H. Bayir, and A. Aygün, "Pca and lda assessment of the heavy metal contamination in honey bees, bee pollen and honey produced in urban areas of türkiye," *Bee Studies- Apiculture Research Institute*, 2023.

Appendix A

Title of the Appendix